UC Santa Barbara
UC Santa Barbara Electronic Theses and Dissertations

Title
Probing forces generated and architectures mediated by Tau on microtubules

Permalink
https://escholarship.org/uc/item/0ck355df

Author
Chung, Peter Jinwoo

Publication Date
2016

Peer reviewed|Thesis/dissertation

UNIVERSITY OF CALIFORNIA

Santa Barbara

Probing forces generated and architectures mediated by Tau on microtubules

A dissertation submitted in partial satisfaction of the

requirements for the degree Doctor of Philosophy

in Physics

by

Peter Jinwoo Chung

Committee in charge:

Professor Cyrus Safinya, Chair

Professor Phil Pincus

Professor Everett Lipman

Professor Stuart Feinstein

Professor Leslie Wilson

March 2016

The dissertation of Peter Jinwoo Chung is approved.

_____

Stuart Feinstein

_____

Les Wilson

_____

Everett Lipman

_____

Phil Pincus

_____

Cyrus Safinya, Committee Chair

March 2016

Probing forces generated and architectures mediated by Tau on microtubules

To other students I had the opportunity to work with through mentorship programs, thank you for giving me the opportunity to not just teach but learn something more about myself, without which I surely would not have grown as much as I have; Avni Bhatt, Ekene Akabike, George Villatoro, Thomas Oyuela-Trachter, Cat Keiner, Andy Lihani, Amy Chen, Robert Palfini, Garrett Chan, Simone Dupuy, Christopher Polstrini, and Julia Korolenko.

To my friends at UCSB, thank you for the love and support you have given me over the years, both in good and more trying times. Elizabeth Sciaky, I cherish you for being a source of both stability and joy over the years. Jared Frey, your relentless positivity is something I aspire to, both inside and outside of work. Annika Jensen, please do not buy that Tiny Home, partially because I still contend it is a ridiculous idea but mostly because you will always have a place to visit and stay wherever I am. Ramsey Majzoub, thank you for being a confidante and sounding board I could rely on and trust.

To my mother, thank you for the patience and understanding. You are the reason why I am here and able to do this today.

VITA OF PETER JINWOO CHUNG
February 2016

EDUCATION

Bachelor of Arts in Physics, University of California, Berkeley, December 2007
Bachelor of Science in Materials Science and Engineering, University of
California, Berkeley, December 2007
Master of Arts in Physics, University of California, Santa Barbara, June 2011
Doctor of Philosophy in Physics, University of California, Santa Barbara,
February 2016 (expected)

PROFESSIONAL EMPLOYMENT

2007-2008: Laboratory technician, Lawrence Berkeley National Laboratory
2008-2009: Graduate teaching assistant, UCSB
2009-2010: Graduate teaching associate, UCSB
2008-2015: Graduate research assistant, Safinya Laboratory, University of
California Santa Barbara

PUBLICATIONS

"Tau intrinsic disorder mediates distinct minima in the energy landscape of
active microtubule bundles," P.J. Chung, C. Song, E. Akabike, A. Bhatt, T.
Oyuela-Trachter, G.A. Villatoro, H.P. Miller, Y. Li, M.C. Choi, L. Wilson, S.C.
Feinstein, and C.R. Safinya, in preparation.

"Tau mediates microtubule bundling architectures mimicking fascicles of
microtubules in the axonal initial segment," P.J. Chung, C. Song, J. Deek, H.P.
Miller, Y. Li, L. Wilson, S.C. Feinstein, and C.R. Safinya, under review.

"Paclitaxel suppresses Tau-mediated microtubule bundling," M.C. Choi, P.J.
Chung, C. Song, H.P. Miller, E. Kiris, Y. Li, L. Wilson, S.C. Feinstein, and C.R.
Safinya, under review.

"Neurofilament networks: salt-responsive hydrogels with sidearm-dependent
phase behavior," J. Deek, P.J. Chung, and C.R. Safinya, *BBA – General
Subjects*, Accepted 1/2016

"Direct force measurements reveal protein Tau confers short-range attractions
and isoform-dependent steric stabilization to microtubules," P.J. Chung*, M.C.

Choi*, H.P. Miller, H.E. Feinstein, U. Raviv, Y. Li, L. Wilson, S.C. Feinstein, and C.R. Safinya, *Proceedings of the National Academy of Sciences*, Accepted 10/2015. (*Authors contributed equally)

"The effect of multivalent cations and Tau on paclitaxel-stabilized microtubule assembly, disassembly, and structure," C.R. Safinya, P.J. Chung, C. Song, Y. Li, K.K. Ewert, M.C. Choi, *Advances in Colloid and Interface Science*, Under Review

"Neurofilament sidearms modulate parallel and crossed-filament orientations inducing nematic to isotropic and re-entrant birefringent hydrogels ," J. Deek, P.J. Chung, J. Kayser, A.R. Bausch, and C.R. Safinya, *Nature Communications* **4**, 2224 (2013).

"Smectic-A and smectic-C phases and phase transitions in 8S5 liquid-crystal aerosol gels," B. Freelon, M. Ramazanoglu, P.J. Chung, R.N. Page, Y.-T. Lo, P. Valdivia, C.W. Garland, and R.J. Birgeneau, *Physical Review E* **84**, 031705 (2011).

HONORS AND AWARDS

MRL Outstanding Mentor Award, 2014
DOW/MRL Travel Fellowship 2013, 2014, 2015
UC Berkeley Regents' and Chancellor's Scholar 2003-2007

SYNERGESTIC ACTIVITIES

Research Internships in Science and Engineering Internship Program, UCSB
    Supermentor, 2012-2014
    Mentor to George Villatoro (2014-2015), Avni Bhatt (2012-2014), Andy Lihani (2013-2014)
California Alliance for Minority Participation, UCSB
    Mentor to Ekene Abike (2013-2014), Cat Keiner (2013), Thomas Oyuela-Trachter (2013-2014)
Summer Institute in Mathematics and Science, UCSB
    Mentor to Amy Chen, Robert Palfini, Garrett Chan, Simone Dupuy, 2013
Interns in Nanosystems Science, Engineering, and Technology, UCSB
    Mentor to Julia Korolenko, 2010-2012
Apprentice Researchers Program, UCSB
    Mentor to Christopher Polistrini, 2010

PROFESSIONAL ASSOCIATIONS

Biophysical Society

.

ABSTRACT

Probing forces generated and architectures mediated by Tau on microtubules

by

Peter Jinwoo Chung

Tau, a developmentally regulated protein localized to the axon of mature neurons, stabilizes axonal microtubules but has been implicated in many neurodegenerative diseases ("tauopathies") including Alzheimer's, Pick's, and, more recently, chronic traumatic encephalopathy. Despite its importance in both development and disease, difficulty in understanding Tau is due, in part, to its intrinsically disordered nature; Tau does not assume a secondary structure in solution. However, lack of structure does not imply lack of function, as Tau binds to microtubules, thereby regulating microtubule assembly/stability and affecting inter-microtubule interactions, although the latter remains controversial. Herein, through microscopy and synchrotron small-angle X-ray scattering of cell free Tau/microtubule reconstitutions under various conditions, we report on the nature of the Tau structure and Tau-mediated interactions between microtubules.

By examining the force-response of Tau-coated paclitaxel-stabilized microtubules by osmotic depletants, we observed that longer isoforms of Tau at high (and physiologically relevant) coverage on microtubules more effectively

sterically stabilize microtubules against microtubule bundling. This steric stabilization occurs by the amino-terminal tail of Tau assuming the conformational (and repulsive) properties of a polyelectrolyte brush. Furthermore, the coverage at which this transition into a polyelectrolyte brush occurs gives the first direct measurement of the size of the longer isoforms of Tau (~20-23 nm) on microtubule surfaces.

To understand the molecular mechanism of Tau-mediated inter-microtubule interactions in dissipative, out-of-equilibrium conditions, we co-polymerized Tau with microtubules in the absence of stabilizing agents (i.e. paclitaxel) and found that Tau mediates microtubule bundles with resultant architectures mimicking fascicles of microtubules found in the axonal initial segment. These bundles confirmed an attractive component to the Tau-mediated microtubule interaction through an aggregate of sub-$k_\mathrm{B}T$ interactions along the microtubule length heretofore unreported in intrinsically disordered systems. The interaction dependence on microtubule length reconciles previous (unsuccessful) attempts at reconstituting Tau-mediated bundles, as stabilizing agents often promoted more, but shorter, microtubules.

These novel biophysical characterizations of Tau on the microtubule surface give insight to the physiological function of Tau inside the neuronal axon and represent possible properties to investigate the role of mutations and post-translational modifications of Tau that lead to neurodegenerative disease.

TABLE OF CONTENTS

1. Introduction

Tau, a protein primarily localized to the axon of mature neurons, is known to stabilize the neuronal cytoskeleton and is critical for the development of neuronal polarity. However, Tau dysfunction has been implicated in many neurodegenerative diseases ("tauopathies") including Alzheimer's[1], Pick's[2], and, more recently, chronic traumatic encephalopathy[3]. Furthermore, genetic analyses have unequivocally demonstrated that specific mutations in Tau result in neuronal death and dementia in many of the aforementioned diseases[4–6]. Despite its importance in neuronal development and neuropathology, understanding of Tau function (and dysfunction) remains limited, partly due to its natively unfolded state in solution (i.e. intrinsically disordered). However, what is known to occur, from both *in vivo* and *in vitro* data, is that Tau associates with and modifies the assembly behavior of microtubules.

1.1 The Microtubule: Assembly and Function

Microtubules are a critical component of the eukaryotic cytoskeleton that are involved in a variety of cell functions, including maintaining cell structure, intracellular trafficking, and cell division[7]. Microtubules are made up straight protofilaments (PFs), polarized head-to-tail assemblies of globular αβ-tubulin heterodimers, which dynamically assemble into hollow protein nanotubes (13-15 PFs, diameter ~ 25-30 nm) that are stabilized by lateral PF-PF interactions (Fig.

1.1). However, microtubules can switch between growing/shrinking phases in a process known as dynamic instability[8], wherein tubulin polymerization into microtubules is interrupted by rapid microtubule depolymerization ("catastrophe"). Catastrophe occurs when GTP bound to the polymerizing end of microtubules (the microtubule GTP cap) is hydrolyzed into GDP, causing protofilaments to peel off as highly-bent GDP-tubulin oligomers and depolymerizing until a new microtubule GTP cap is formed, restarting the entire process[9]. Furthermore, the depolymerization of microtubules is often enhanced in cold environs (4°C) and with the addition of calcium ions[10].
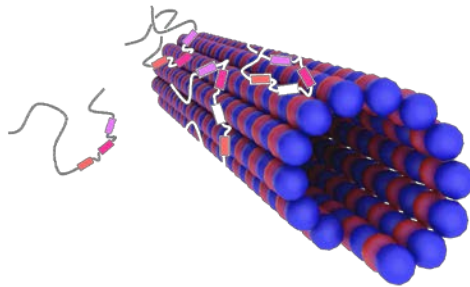
Figure 1.1| A microtubule, made up of linear, polarized arrays of dimerized αβ-tubulin (i.e. protofilaments) which self-assemble to form hollow nanotubes. Microtubules are often functionalized with the addition of microtoubule-associated proteins such as Tau (depicted as gray strings).

Despite the complex nature of microtubule assembly, microtubules can assume a variety of roles that either emphasizes its dynamic nature or its presence as a rigid support. In eukaryotic cell division, microtubules form from centromeres at opposing ends of the cell, searching (polymerizing) until a chromosome is found, and restarting (depolymerizing) if it is not[11]. In

intracellular trafficking, kinesin and dynein travel with their subcellular cargoes on microtubule networks, with both motor proteins uniquely evolved to travel towards opposing polarized ends of the microtubule. Although they are already superstructures of tubulin, microtubules can be a subunit of even larger cellular architectures, as seen in microtubule doublets that form the backbone of flagella, lash-like cellular appendages that rotate in one direction to provide cellular locomotion.

Commensurate with the variety of roles microtubules play are the diversity of proteins that associate with microtubules. Specific microtubule-associated proteins (MAPs) are found in distinct cell types (and sometimes, even subcellular compartments) and help functionally differentiate microtubules by altering polymerization dynamics, modifying inter-microtubule interactions, or guiding microtubules towards specific cellular locations. Even in associating with microtubules do MAPs differ; some MAPs bind to the growing tip of microtubules (the EB-family of MAPs), others bind on the microtubule inner lumen, but most associate with the outer surface of microtubules.

1.2 The Microtubule-Associated Protein, Tau

One MAP in particular, Tau, is found to be abundant in neurons of the central nervous system and is often found almost exclusively in the healthy neuronal axons[12], the long, dynamic process that extends from the neuronal cell body. Tau has been long known to minimize dynamic instability in

microtubules[13,14], but its importance in neuropathology was not realized until it was discovered Tau was a constitutive component of neurofibrillary tangles[15,16], one of the pathological hallmarks of Alzheimer's disease. Subsequent research would identify Tau as part of other pathological aggregations and extend neurofibrillary tangles to other pathologies, leading to the umbrella term "tauopathies," or neurodegenerative diseases related to Tau.

While both tauopathies and the regulation of Tau during neuronal development spurred extensive research into the function and structure of the protein, efforts were hampered by the intrinsically disordered nature of Tau. Unlike most proteins which form secondary structures, Tau lacks an ordered structure in solution and is better described as a random coil[17,18]. Thus, Tau is instead described through its primary sequence from N- to C- terminus: the N-terminal tail (NTT) consists of a projection domain (PD, with low affinity for microtubules and projecting off its surface[19,20]) and a proline-rich region (PRR, with weak affinity for microtubules), then the microtubule-binding region (MTBR; a series of 3-4 18 amino acid long imperfect repeats separated from one another by 13-14 amino acid long inter-repeats), and finally a C-terminal tail (CTT, with low affinity for microtubules[21–24]. The human central nervous system expresses 6 wild type (WT) isoforms (Fig. 1b) through alternative splicing; the MTBR either has 4 or 3 imperfect repeats (4R- or 3R- Tau isoforms), depending on expression/non-expression of exon 10. The PD length depends on expression

of exons 2 and/or 3 with +/+, +/-, and -/- resulting in long (-L), medium (-M), and

short (-S) length PDs, respectively (Fig. 1.2).
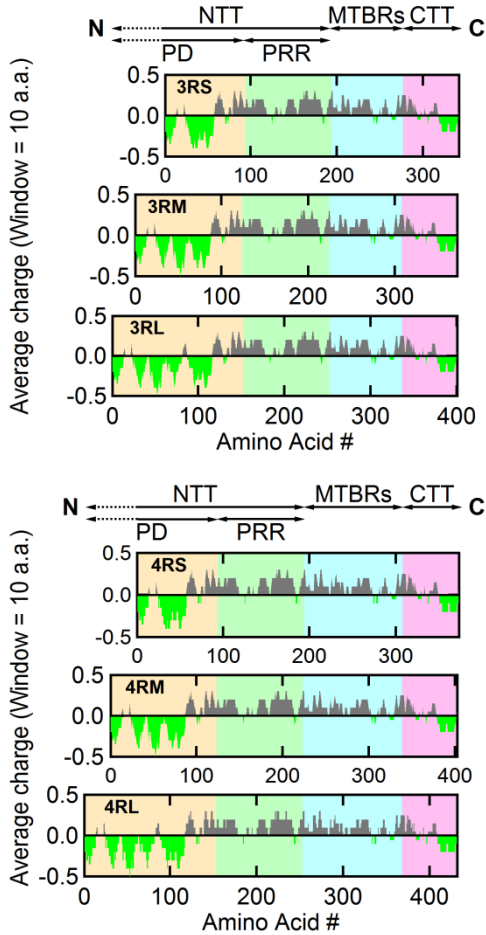
Figure 1.2| Charge (averaged over 10 residues) versus amino acid residue number for six isoforms of human Tau. The charge distribution diagram of each isoform shows the cationic (grey) nature of Tau with the exception the amino- and carboxyl- terminal tails which include anionic (bright green) regions, which lead to dipole-like characteristics.. The N-terminal (NT) is made up of the projection domain (PD, yellow background, first 92, 121, and 150 AAs for -S, -M and -L isoforms) and proline-rich region (PRR, green background, next 94 AAs), followed by MT-binding region (MTBR, blue background), and ending at the carboxyl-terminus (C) with the C-terminal (CT, pink background). Tau isoforms have either 3 or 4 microtubule-binding repeats (3R-, 4R-) as a result of excluding (or including) exon 10 (33 amino acids), which contains second microtubule-binding repeat and the interrepeat region between first and second repeat. Additionally, the exclusion of exons 2 and 3 (both 29 amino acids), exclusion of

exon 2, or no exclusions in the PD result in the short (-S), medium (-M), or long (-L) isoforms, respectively.[1]

The expression of the six different Tau isoforms is developmentally regulated. The fetal brain expresses only the shortest isoform (3RS) while the adult brain (with Tau concentration increasing along the length of the axon away from the cell body) expresses an approximately 1:1 ratio of 4R- and 3R-Tau[25]. In the adult brain, the composition of the different isoforms is not known as a function of position along the axon, but averaged over the entire length of the axon, the -S, -M, and -L N-terminal isoform ratio is 4:5:1, respectively[26].

1.3 Interactions between Microtubules and Tau

The most well-characterized function of Tau, upon binding to microtubules, is the suppression of microtubule dynamic instability by decreasing the rate of catastrophe with increasing Tau[27,28] (Fig. 1.3).

---

[1] This figure and caption has been adapted with permission from Chung *et al*, Proceedings of the National Academy of Sciences 2015, **112**. Copyright 2015 National Academy of Sciences, USA
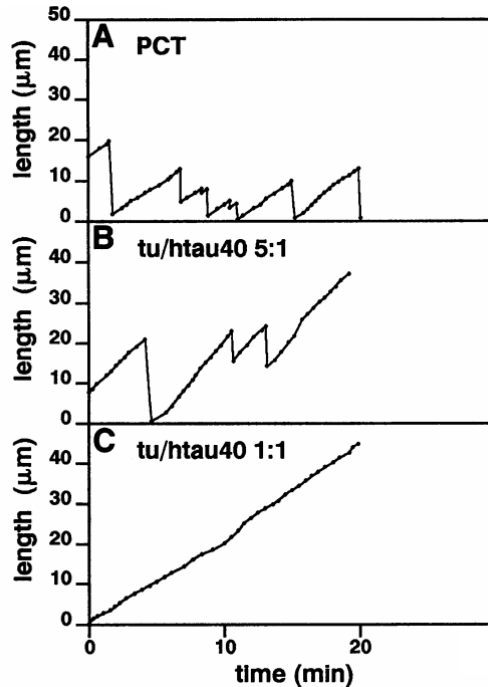
Figure 1.3| **A,** Plotting the length (as measured from the plus-ends) of microtubules (derived from tubulin purified over a phosphocellulose column, or PCT) as a function of time show microtubule dynamic instability. **B,** With the addition of Tau (tu/htau40 5:1, or Tau to tubulin-dimer molar ratio $\Phi_{4RS}=1/5$), microtubule dynamic instability is slightly suppressed. **C,** At higher concentration of Tau (tu/htau40 1:1, or $\Phi_{4RS}=1/1$), microtubule dynamic instability is almost entirely suppressed. Adapted from Trinczek *et al*[28].

It was later discovered that Tau was primarily able to suppress microtubule dynamic instability through the microtubule-binding region (MTBR) binding to microtubules, with assistance from regions flanking the MTBR (the C-terminal tail and proline-rich regions)[14,24]. This stabilizing activity was found to be the result from highly conserved residues that bind dynamically to the interface between protofilaments in microtubules[29], thereby promoting microtubule assembly and stabilization.

7

While the caryboxyl-terminal half of Tau has been relatively well characterized, the amino-terminal half (and more specifically, the projection domain) has not, despite four of the six Tau isoforms resulting from changes in the Tau projection domain. Seminal studies[20,30] of non-neuronal cells overexpressing transfected Tau cDNA had concluded that the Tau projection domain determines inter-microtubule distances in observed widely-spaced hexagonally-ordered microtubule arrays in neurite-like processes (Fig, 1.4). However, the studies could not discern whether the bundles were a repulsive lattice under confinement or the result of axially-symmetric microtubule attractions induced by Tau. Cell free experiments offered conflicting results. While the absence of bundles in cell free reconstitutions of microtubules with WT Tau led to the conclusion that Tau mediated a purely-repulsive force between microtubules[14,31], surface force apparatus measurements of Tau-coated mica surfaces exhibited an attractive potential[32].
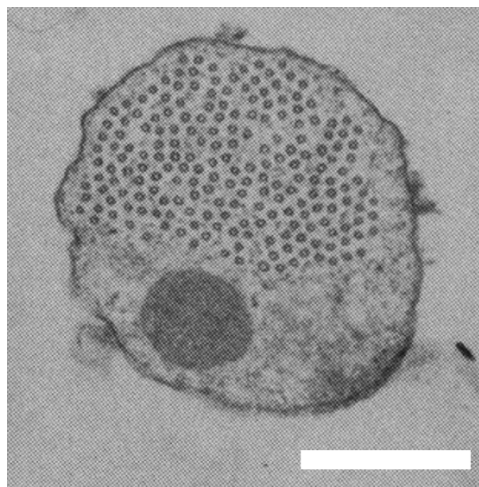
Figure 1.4 | Overexpression of Tau cDNA transfected in non-neuronal cells result in neurite-like processes from which hexagonally-ordered microtubule arrays are clearly evident. As the spacing seemed to be dependent of that of the Tau

projection domain, Tau was thought to mediate widely-spaced microtubule bundles although recapitulation of such bundles in cell-free reconstitutions have been difficult. Scale bar, 500 nm, and adapted from Chen *et. al*[20].

Furthermore, prior to the discovery of Tau, groundbreaking electron micrscopy studies of the fine structure of axons in mature rat hippocampal neurons revealed that the axon-initial segment contained widely-spaced string-like microtubule bundles ("fascicles of microtubules", Fig. 1.5)[33,34]. However, the connection between fascicles and Tau remain an open question, although the evidence of higher-order microtubule structures in non-neuronal cells would perhaps indicate Tau may be responsible for such structures in the axon of the neuron.
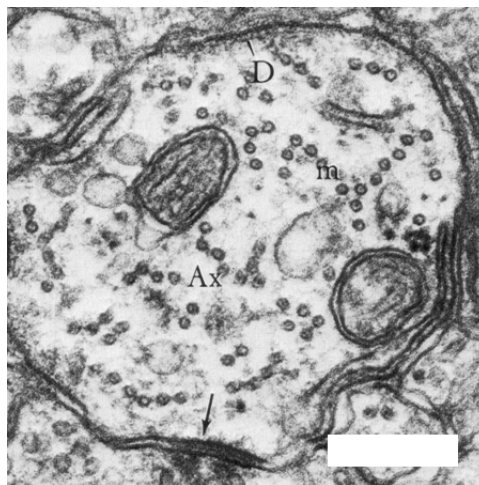
Figure 1.5| Electron microscopy of the fine structure of the axon initial segment reveals linear bundles of microtubules ("fascicles of microtubules") with wide spacings between microtubules. This is one of the few observed instances of any kind of higher-order structure of microtubules in axons. Scale bar, 250 nm, and adapted from Peters *et. al*[34].

1.4 References

1.   Grundke-Iqbal, I. *et al.* Abnormal phosphorylation of the microtubule-associated protein tau (tau) in Alzheimer cytoskeletal pathology. *Proc. Natl. Acad. Sci. U. S. A.* **83,** 4913–4917 (1986).

2.   Love, S., Saitoh, T., Quijada, S., Cole, G. M. & Terry, R. D. Alz-50, ubiquitin and tau immunoreactivity of neurofibrillary tangles, Pick bodies and Lewy bodies. *J. Neuropathol. Exp. Neurol.* **47,** 393–405 (1988).

3.   McKee, A. C. *et al.* Chronic traumatic encephalopathy in athletes: progressive tauopathy after repetitive head injury. *J. Neuropathol. Exp. Neurol.* **68,** 709–735 (2009).

4.   Clark, L. N. *et al.* Pathogenic implications of mutations in the tau gene in pallido-ponto-nigral degeneration and related neurodegenerative disorders linked to chromosome 17. *Proc. Natl. Acad. Sci. U. S. A.* **95,** 13103–13107 (1998).

5.   Spillantini, M. G. *et al.* Mutation in the tau gene in familial multiple system tauopathy with presenile dementia. *Proc. Natl. Acad. Sci. U. S. A.* **95,** 7737–7741 (1998).

6.   Hutton, M. *et al.* Association of missense and 5'-splice-site mutations in tau with the inherited dementia FTDP-17. *Nature* **393,** 702–705 (1998).

7.   Desai, A. & Mitchison, T. J. Microtubule polymerization dynamics. *Annu. Rev. Cell Dev. Biol.* **13,** 83–117 (1997).

8.   Mitchison, T. & Kirschner, M. Dynamic instability of microtubule growth. *Nature* **312,** 237–42 (1984).

9.   Löwe, J., Li, H., Downing, K. H. & Nogales, E. Refined structure of alpha beta-tubulin at 3.5 A resolution. *J. Mol. Biol.* **313,** 1045–1057 (2001).

10. Weisenberg, R. C. Microtubule formation in vitro in solutions containing low calcium concentrations. *Science* **177,** 1104–5 (1972).

11. Biology, C. *Cell Biology*. (Saunders/Elsevier, 2008).

12. Binder, L. I., Frankfurter, A. & Rebhun, L. I. The distribution of tau in the mammalian central nervous system. *J. Cell Biol.* **101,** 1371–1378 (1985).

13. Cleveland, D. W., Hwo, S. Y. & Kirschner, M. W. Purification of tau, a microtubule-associated protein that induces assembly of microtubules from purified tubulin. *J. Mol. Biol.* **116,** 207–225 (1977).

14. Gustke, N., Trinczek, B., Biernat, J., Mandelkow, E. M. & Mandelkow, E. Domains of tau protein and interactions with microtubules. *Biochemistry* **33,** 9511–9522 (1994).

15. Wood, J. G., Mirra, S. S., Pollock, N. J. & Binder, L. I. Neurofibrillary tangles of Alzheimer disease share antigenic determinants with the axonal microtubule-associated protein tau (tau). *Proc. Natl. Acad. Sci. U. S. A.* **83,** 4040–4043 (1986).

16. Goedert, M., Spillantini, M. G., Jakes, R., Rutherford, D. & Crowther, R. a. Multiple isoforms of human microtubule-associated protein tau: sequences and localization in neurofibrillary tangles of Alzheimer's disease. *Neuron* **3,** 519–526 (1989).

17. Mylonas, E. *et al.* Domain conformation of tau protein studied by solution small-angle X-ray scattering. *Biochemistry* **47,** 10345–10353 (2008).

18. Schweers, O., Schönbrunn-Hanebeck, E., Marx, A. & Mandelkow, E. Structural studies of tau protein and Alzheimer paired helical filaments show no evidence for beta-structure. *J. Biol. Chem.* **269,** 24290–24297 (1994).

19. Kanai, Y., Chen, J. & Hirokawa, N. Microtubule bundling by tau proteins in vivo: analysis of functional domains. *EMBO J.* **11,** 3953–3961 (1992).

20. Chen, J., Kanai, Y., Cowan, N. J. & Hirokawa, N. Projection domains of MAP2 and tau determine spacings between microtubules in dendrites and axons. *Nature* **360,** 674–677 (1992).

21. Lee, G., Cowan, N. & Kirschner, M. The primary structure and heterogeneity of tau protein from mouse brain. *Science (80-.).* **239,** 285–288 (1988).

22. Butner, K. A. & Kirschner, M. W. Tau protein binds to microtubules through a flexible array of distributed weak sites. *J. Cell Biol.* **115,** 717–730 (1991).

23. Lee, G., Neve, R. L. & Kosik, K. S. The microtubule binding domain of tau protein. *Neuron* **2,** 1615–1624 (1989).

24. Goode, B. L. & Feinstein, S. C. Identification of a novel microtubule binding and assembly domain in the developmentally regulated inter-repeat region of tau. *J. Cell Biol.* **124,** 769–781 (1994).

25. Kosik, K. S., Orecchio, L. D., Bakalis, S. & Neve, R. L. Developmentally regulated expression of specific tau sequences. *Neuron* **2,** 1389–1397 (1989).

26. Hong, M. *et al.* Mutation-specific functional impairments in distinct tau isoforms of hereditary FTDP-17. *Science* **282,** 1914–1917 (1998).

27. Drechsel, D. N., Hyman, A. A., Cobb, M. H. & Kirschner, M. W. Modulation of the dynamic instability of tubulin assembly by the microtubule-associated protein tau. *Mol. Biol. Cell* **3,** 1141–1154 (1992).

28. Trinczek, B., Biernat, J., Baumann, K., Mandelkow, E. M. & Mandelkow, E. Domains of tau protein, differential phosphorylation, and dynamic instability of microtubules. *Mol. Biol. Cell* **6,** 1887–1902 (1995).

29. Kadavath, H. *et al.* Folding of the Tau Protein on Microtubules. *Angew. Chemie Int. Ed.* n/a–n/a (2015). doi:10.1002/anie.201501714

30. Baas, P. W., Pienkowski, T. P. & Kosik, K. S. Processes induced by tau expression in Sf9 cells have an axon-like microtubule organization. *J. Cell Biol.* **115,** 1333–1344 (1991).

31. Brandt, R. & Lee, G. Orientation, assembly, and stability of microtubule bundles induced by a fragment of tau protein. *Cell Motil. Cytoskeleton* **28,** 143–154 (1994).

32. Rosenberg, K. J., Ross, J. L., Feinstein, H. E., Feinstein, S. C. & Israelachvili, J. Complementary dimerization of microtubule-associated tau protein: Implications for microtubule bundling and tau-mediated pathogenesis. *Proc. Natl. Acad. Sci. U. S. A.* **105,** 7445–50 (2008).

33. Palay, S. L., Sotelo, C., Peters, A. & Orkand, P. M. The axon hillock and the initial segment. *J. Cell Biol.* **38,** 193–201 (1968).

34. Peters, A., Palay, S. L. & Webster, H. deF. *The Fine Structure of the Nervous System: Neurons and Their Supporting Cells.* (Oxford University Press, 1991).

2. Methods and Techniques

While I will be summarizing the many experimental techniques used to replicate and examine the environmental conditions in which microtubules and Tau are found, I will first focus on the physical underpinnings of methods particular to our studies: the osmotic stress technique (recapitulating the macromolecular crowding within cells) and small-angle X-ray scattering (angstrom-resolution measurements of structures in solution).

2.1 Osmotic Stress through Depletion Forces

In order to fully capture the properties of biological assemblies, replication of the local environs (i.e. state variables) of the cytoplasm in which the system exists is necessary. For example, human physiological temperature ($\sim 37°$ C) can be easily obtained through the use of a sample oven and cytoplasmic salinity/pH mimicked through the use of the appropriate buffer with added monovalent/divalent salts. However, there is one effect that has been difficult to reproduce: macromolecular crowding. Biological macromolecules, unlike the dilute conditions in which biochemical/biophysical experiments are often run, exist and function in crowded environments. Macromolecular crowding can increase reaction rates, initiate protein aggregation, and even induce structures that would have not otherwise been observed in solution, even when accounting for increase in reaction rates vis-à-vis concentration[1,2].

A fundamental force underlying many crowded environment physics is the depletion force, which is an attractive force between large colloidal particles (our biological macromolecule of interest) as a result of being suspended in a dilute solution of smaller solutes, or depletants[3]. This force arises as a result of depletants being preferentially excluded near the vicinity of colloidal particles, an absence of which creates an effective osmotic pressure (or stress) between colloidal particles[4]. Counter intuitively, this effectively entropic force promotes demixing of different colloids in solutions, the magnitude and range of which is dependent on the geometry, nature, and size of both the colloidal particles and depletants (as I will be later demonstrating with the calculation of depletion forces on cylinders by ideal polymers). Through this concept, Parsegian and associates developed[5] the osmotic stress technique to measure the force response between particles and membranes in solution through the use of inert depletants.

One can easily extend the concept of depletion attraction to that of the crowded macromolecular environment. Cells are often packed, with the macromolecular concentration of solutes of *e. coli* measured[6] to be ~0.3 to 0.4 g/mL. Indeed, depletion forces artificially induced in cell free conditions can recapitulate structures found *in vivo*. The sickle cell hemoglobin fiber naturally "zippers" both *in vivo* and *in vitro* (the latter in the presence of depletants), with the energy required to bundle the fibers from *in vitro* experiments[8] to be -7.2 $k_B T/\mu$m.

2.1.1 Depletion Forces on Cylinders by Ideal Polymers[1]

Depletion forces can arise when large colloidal and cylindrical particles (such as microtubules [MTs]) are suspended in a dilute solution of inert polymers (osmotic depletants) such as poly(ethylene oxide), MW=20 kDa (20k PEO). The depletants are preferentially excluded from the vicinity of the colloidal particles due to its inability to get closer than its effective radius, a (Figure 2.1). In the low-concentration limit (dilute regime), the monomers apply an ideal gas-like osmotic pressure $\Pi_{osm}=ck_{\mathrm{B}}T$ (where c is the number density of 20k PEO) owing to a reduction of excluded volume when excluded volumes overlap[9].
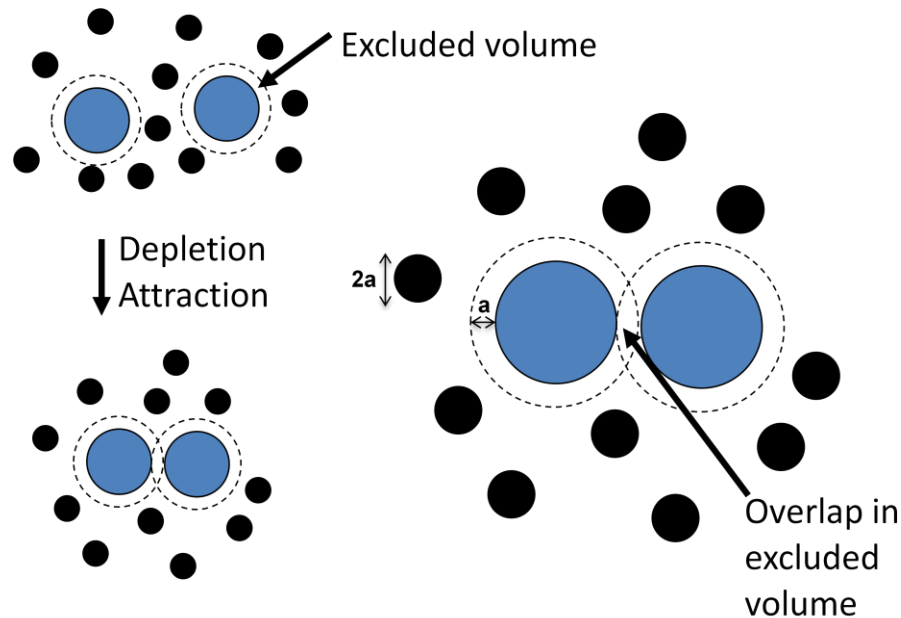
Figure 2.1| An axial view of parallel cylinders bundled by depletion attraction. The 20k PEO (black circles) is barred from the excluded volume (dashed line) around the microtubules (blue circles). The overlap of these two excluded volumes results in an excess volume available for the 20k PEO, leading to an

entropically induced attraction between microtubules (equivalently, the removal of 20k PEO depletants results in an excess PEO density around the MTs, pushing them together).

The depletion energy per unit length (at the dilute limit) takes the form[4]:

$$V_{depletion} = -ck_B TA(H, R, a) \qquad\qquad\qquad \text{(Eq. 2.1)}$$

where $A(H)$ is the overlap of the excluded area (cross section of overlap of the excluded volume) as a function of the distance H between the surface of two circular cylinders of radius R (for MTs[10], R=12.5nm), surrounded by monomers of radius a (for 20k PEO, the effective depletant radius for a polymer of radius of gyration, R_G = 6.9 nm, $a = \frac{2R_G}{\sqrt{\pi}}$ = 7.8 nm)[11,12]. By constructing two circles of radius R' and center-to-center distance d (Figure 1.2), the known formula[9] for circular segments is used to calculate the excluded area with the appropriate translation, $R' \rightarrow R + a$ and $d \rightarrow H + 2R$
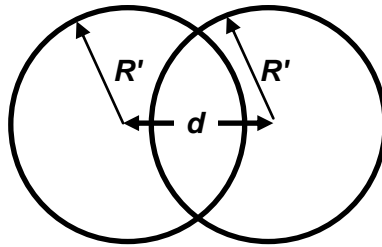
Figure 2.2| The overlap of two circles as a function of center-to-center distance. The lens shaped region is a sum of two circular segments.

$$A(d, R') = 2R'^2 \cos^{-1}\left(\frac{d}{2R'}\right) - \frac{d}{2}\sqrt{4R'^2 - d^2}$$

$$A(H, R, a) = 2(a+R)^2 \cos^{-1}\left(\frac{H+2R}{2(a+R)}\right) - \frac{(H+2R)}{2}\sqrt{(2a-H)(2a+H+4R)}$$

$$A(H, R, a) = (a+R)^2\left[2\cos^{-1}\left(\frac{H+2R}{2(a+R)}\right) - \frac{(d+2R)\sqrt{(2a-H)(2a+H+4R)}}{2(a+R)^2}\right] \qquad \text{(Eq. 2.2)}$$

$$A(H, R, a) = \begin{cases} (a+R)^2\left[2\cos^{-1}\left(\frac{H+2R}{2(a+R)}\right) - 2\left(\frac{H+2R}{2(a+R)}\right)\sqrt{1 - \left(\frac{H+2R}{2(a+R)}\right)^2}\right] & 0 < H \leq 2a \\ 0 & H > 2a \end{cases}$$

Which is mathematically equivalent to results of previous work[8]

$$A(H, R, a) = \begin{cases} (a+R)^2(\Theta - \sin(\Theta)) & 0 < H \leq 2a \\ 0 & H > 2a \end{cases} \qquad \text{(Eq. 2.3)}$$

where $\Theta = 2\sin^{-1}\left(\frac{\sqrt{(2a-H)(2a+H+4R)}}{2(a+R)}\right)$. This is shown by setting $x = \left(\frac{H+2R}{2(a+R)}\right)$ and

using the identities $2x\sqrt{1-x^2} = \sin\left(2\sin^{-1}\left(\sqrt{1-x^2}\right)\right)$ and $Cos^{-1}(x) = Sin^{-1}\left(\sqrt{1-x^2}\right)$ such

that Equation 2.2 becomes:

$$A(H, R, a) = (a+R)^2\left[2\sin^{-1}\left(\sqrt{1-x^2}\right) - \sin\left(2\sin^{-1}\left(\sqrt{1-x^2}\right)\right)\right] \qquad \text{(Eq. 2.4)}$$

By setting $\Theta = 2\sin^{-1}\left(\sqrt{1-x^2}\right) = 2\sin^{-1}\left(\frac{\sqrt{(2a-H)(2a+H+4R)}}{2(a+R)}\right)$, we get exact

published results as before. Thus, the potential energy normalized (in the dilute

regime) is:

$$V_{depletion}(H) = -ck_B T A(H, R, a) \qquad \text{(Eq. 2.5)}$$

However, it is important to note that this is a simplified derivation; in

treating PEO as an ideal gas (dilute regime), interactions between individual

17

polymers (2nd and higher order virial-coefficients) are not taken into account. Experimental measurements are needed to obtain the osmotic pressure (Π) of polymer-induced depletion forces. Thus, the depletion-attraction potential energy used in our modeling was:

$$V_{depletion}(H) = -\Pi A(H, R, a)$$ (Eq. 2.6)

Π is the measured depletant osmotic pressure $(\lim_{c \to 0} \Pi = c k_B T)$. Fortunately, measurements of the osmotic pressure for the dilute and semi-dilute regime of 20k PEO have been reported[13] (Figure 2.3), allowing quick translation between wt% of 20k PEO and osmotic pressure values.
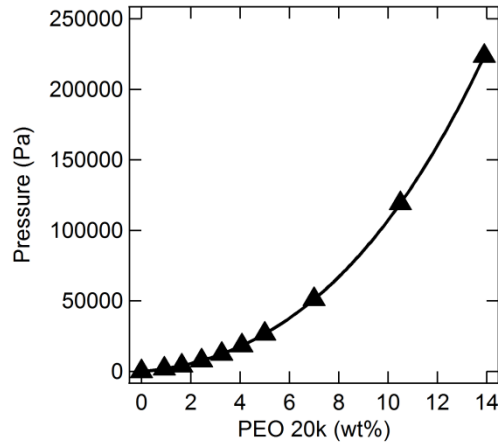
Figure 2.3| **The osmotic pressure measured for increasing wt% of 20k PEO.** Experimentally derived data points (triangle markers) for the osmotic pressure (Pa) is used to obtain a best-fit line to extrapolate pressures for any given wt% of 20k PEO, where $Log_{10}(\Pi) = 0.57 + 2.75\,(PEOwt\%)^{0.21}$.

2.1.2 Experimental Considerations: Depletant Size[2]

One of the experimental limitations of the osmotic stress technique is the finite range of the depletion force, which is characterized by the size of the depletant (thus defining the excluded volume/area). Ordinarily, this is not an issue with most colloidal systems; in solution, the distance between large colloidal particles will eventually fall in range of the depletion force by even Brownian motion alone. However, this assumption will not hold if there is a repulsive force or steric spacers between colloids that are larger than the range of the depletion force.

In particular, cytoskeletal systems often exhibit higher-order networks made up biopolymers spaced by sidearms or other proteins[14,15]. If the spacing between biopolymers is larger than that of the depletants being used, it is quite possible that the depletants will interpenetrate the region between biopolymers, exerting no osmotic pressure and precluding the basis for adding osmotic depletants to begin with!

This limitation can be overcome with the use of larger depletants (or, in the case of ideal polymers, increasing polymer MW), but larger depletants are not without drawbacks, as well. Often, larger depletants have not been characterized as well or over the same thermal range as smaller depletants. Furthermore, increase in depletant size means a concomitant decrease in

---

[2]This section has been adapted, in part, with permission from Chung *et al*, Nature Communications 2015, **112**. Copyright 2016 Nature Publishing Group, USA

depletant density, effectively limiting the realizable osmotic pressure range due to the depletant solubility limit.

For widely-spaced microtubule bundles (see chapter 4 of this dissertation), we used a high-molecular weight poly(ethylene oxide), MW=100 kDa (PEO100k). PEO100k was used as the osmotic depletant of choice compared to better-characterized depletants to parameters unique to our system: as stable inter-microtubule distances of up to 38 nm were observed, the size of the depletant had to be equal or greater than that distance in order to create a concentration differential inside/outside the microtubule bundle. Prior work[12] measured the radius of gyration (R_G) of a function of PEO molecular weight (*MW*):

$$R_G = 0.215 MW^{0.583} \qquad\qquad \text{[nm]} \qquad\qquad \text{(Eq. 2.7)}$$

Thus, the effective depletant radius[16], a = $2R_G\pi^{-1/2}$ = 19.95 nm, or an effective depletant diameter, $d \approx 40$ nm, satisfies our experimental conditions that polymer not penetrate the space between microtubules in microtubule bundles.

A previous study[17] measured the osmotic pressure (in Pa), *P*, of an aqueous solution of varying concentrations (cg mL^{-1}), *wt%*, of poly(ethylene oxide) (M_W=105,000 g mole^{-1}) at 35° C, which was taken as an reasonable approximation of the behavior of PEO100k at 37° C, absent further data. Data was fit to a 2nd order polynomial (following the mathematical form of a virial expansion for an ideal gas) to determine a formula to relate an arbitrary PEO100k concentration to a corresponding osmotic pressure:

$$P = 147.38\text{wt\%} + 338.19\text{wt\%} \qquad [\text{Pa}] \qquad \qquad (\text{Eq. 2.8})$$

2.2 Small-angle X-ray scattering

Small-angle X-ray scattering (SAXS) is an ideal technique for understanding the structure of both biological macromolecules and their higher order assemblies in solution, without the use of non-biological tags or labels. While there are a great many resources available on X-ray scattering[18–20], as with the prior section I will deal with the basics of X-ray scattering with the eventual goal of describing SAXS as it is relevant to our system of microtubules and Tau. This is not to say that the described formalism is limited only to microtubules; the power in scattering is that both the incident particle (X-rays, neutron, light) and associated wavelengths can be adjusted, appropriate for the sample scattering length and geometry.
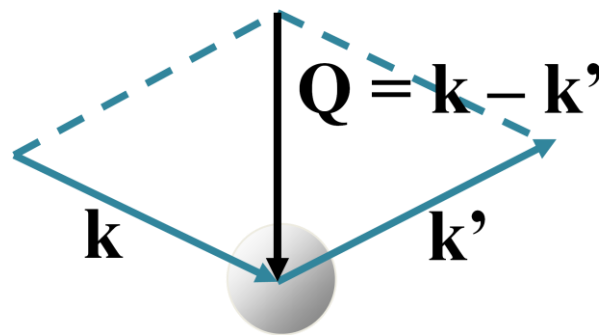
Fig. 2.4 | Scattering off an arbitrary object. Q is the difference between the incident and scattered wave vector, also known as the scattering vector.

The basic process of elastically scattering an X-ray photon (e.g. a photon with energy 100 eV to 100 keV) off an object can be depicted in Fig. 2.4, in which the scattered intensity is observed as a function of the scattering vector $\mathbf{Q}$, such that:

$$\hbar\mathbf{Q} = \hbar\mathbf{k}\text{-}\hbar\mathbf{k'} \qquad\qquad\qquad\qquad\qquad \text{(Eq. 2.9)}$$

Where $\hbar\mathbf{k}$ and $\hbar\mathbf{k'}$ are the initial and final momentum of the photon scattered, respectively. It is worth noting that this chapter (and thesis) will be focused on elastic scattering (i.e. the photon energy is conserved and only momentum transfer occurs during the scattering process). While there are a myriad of techniques (and associated theories) dealing with inelastic X-ray scattering (e.g. Compton scattering, which occurs more prominently with high energy x-rays), the photons we use to analyze our samples of interest are in the lower energy hard X-ray regime (5 to 10 keV) which precludes much (if any) contribution from inelastic scattering.

Experimentally, photons are emitted from a source towards a sample and the scattered intensity (as a function of $\mathbf{Q}$) is captured via a 2-dimensional detector and subsequently analyzed via line-shape analysis or model fitting. While there have been many advances in both the X-ray sources (from 3rd generation synchrotron sources to 1st generation X-ray free electron lasers) and detectors (2D CCDs and active pixel solid state detectors), the theoretical framework by which X-ray scattering is approached has remained, more or less, unchanged for quite some time.

2.2.1 The Form Factor: Scattering off an Object

While small-angle X-ray scattering experiments measure the intensity of light scattered $I(\mathbf{Q})$, our calculations begin with the form factor $f(\mathbf{Q})$ (which, when multiplied by its complex conjugate, yields $I(\mathbf{Q})$). The form factor $f(\mathbf{Q})$ is ameasure of the scattering amplitude of a wave by an isolated object (objects in a dilute regime can be considered isolated), which is the Fourier transform of the electron number density $\rho(\mathbf{r})$ as a function of the scattering vector $\mathbf{Q}$:

$$f(\mathbf{Q}) = \int \rho(\mathbf{r})e^{i\mathbf{Q}\cdot\mathbf{r}}d\mathbf{r} \qquad\qquad (\text{Eq. 2.10})$$

Implicit in the calculation of the form factor is *a priori* knowledge of the general shape of the objects being scattered. Practically speaking, this knowledge can be obtained via other real space techniques (i.e. electron microscopy, atomic force microscopy) or explicit assumptions/calculations made, with subsequent measurements by X-rays allowing iterative refinements of primitive to more advanced models that realistically capture accurate and relevant information about the objects.

For the sake of simplicity, let us take the case of the atomic form factor, or the scattering amplitude of electrons of an atom. To illustrate the importance of the selection of the "correct" scattering vector $\mathbf{Q}$ we examine the limiting cases of atomic form factor (i.e. scattering off of individual atoms):

$$f(\mathbf{Q}) = \begin{cases} Z & \text{for} & \mathbf{Q} \to 0 \\ 0 & \text{for} & \mathbf{Q} \to \infty \end{cases} \qquad\qquad (\text{Eq. 2.11})$$

The first case is the limit in which the phase factor $e^{i\mathbf{Q}\cdot\mathbf{r}}$ approaches unity, in which case Eq. 2.10 just devolves into the integration of the electron number density of the atom (or simply, Z). The second case will have the phase factor $e^{i\mathbf{Q}\cdot\mathbf{r}}$ fluctuate around the unit circle in which case all contributions from the number density cancel each out (i.e. scattering from other electrons destructively interfere with each other with no resultant scattering).

(As an aside, this is not to say that $\mathbf{Q}$ must be chosen in order to obtain realizable form factor; indeed, if $\mathbf{Q}$ is so small such that the inverse is larger any length scale associated with the object, form factors can be approximated as Gaussians and other important information, such as the radius of gyration of the particle, can be accessed in what is known as the Guinier regime. On the other hand, at larger $\mathbf{Q}$ scattering due to the form factor becomes less of an issue, which is especially helpful when scattering due to the form factor starts to become "noise" in data, see section 2.2.5.)

The case of the atomic form factor should clearly indicate that the electron density of larger objects can be calculated, as long as the appropriate $\mathbf{Q}$ range is selected. Indeed, it is by this principle that X-ray scattering is used to measure the size and shape of objects larger than just atoms, like biomacromolecules such as microtubules.

2.2.2. The Form Factor for a Microtubule, or a Hollow Cylinder

As mentioned previously, microtubules are hollow, protein nanotubes made up of a variable number of protofilaments. To first order, microtubules can be approximated as hollow cylinders with well-defined wall thickness δ (equal to the protofilament radial thickness) of constant electron density ρ_0, with a variable (fit parameter) inner radius r_{in}, to account for the changing protofilament number.

A note must be made about ρ_0. While the constant electron density ρ_0 seems to be a gross oversimplification of the charge distribution of proteins, for globular proteins this assumption holds up quite nicely[10,16,21,22], especially at the $\mathbf{Q}$ range over which the microtubule form factor is relevant (Eq. 2.11). Furthermore, as we are dealing with objects in solution, what we are really concerned with is $\Delta\rho_0$, or the difference in charge density between solution and object, which corresponds to the change density difference between the buffer solution (effectively, water) and the microtubule.

In describing the electron density of a hollow cylinder, the choice of coordinate system is obvious. Using a real-space cylindrical coordinate system (Fig. 2.4, left) with corresponding reciprocal-space coordinate system (Fig 2.4, right) simplifies the math involved a great deal. In this case, reciprocal-space (or $\mathbf{Q}$-space) represents the Fourier transform of the real-space. An appropriate analogy is just as the Fourier transform of a radio signal over time is the sum of waves with different frequencies, the Fourier transform of an real space object

25

can be considered to be a sum of waves with different lengthscale distributions in the reciprocal space.
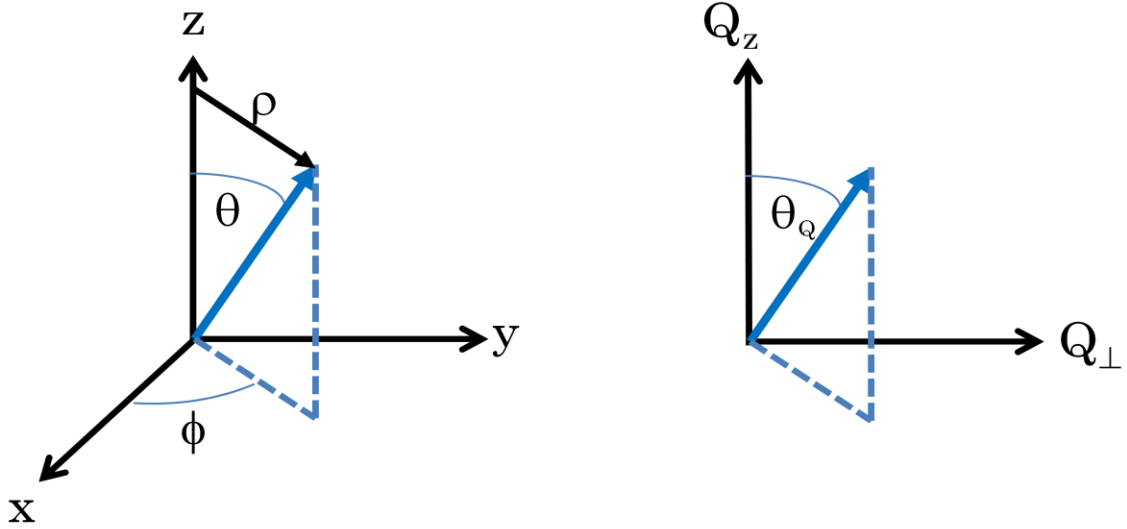
Figure 2.4| A cylindrical coordinate system in real-space (left) and Q-space (right)

Assuming an azimuthally-symmetric cylinder of length 2H axially aligned with the z-axis and, the resultant form factor (Eq. 2.9) can be written in $\mathbf{Q}$ space as:

$$f(Q_\perp,Q_z) = \rho_0 \int_{-H}^{H} e^{-iQ_z \cdot z}\, dz \int_{r_{in}}^{r_{in}+\delta} \rho\, d\rho \int_0^{2\pi} e^{-iQ_\perp \cdot \rho \cos\theta}\, d\theta \qquad \text{(Eq. 2.11)}$$

The first integral and third integral reduces to a Bessel function of the first kind of order zero, $J_0(Q_z H)$ and $2\pi * J_0(Q_\perp \rho)$, respectively. Thus, the form factor for a hollow cylinder is:

$$f(Q_\perp,Q_z) = \frac{2\pi\rho_0 J_0(Q_z H)}{Q_\perp}\left[(r_{in} + \delta) * J_1\big(Q_\perp(r_{in} + \delta)\big) - r_{in} * J_1(Q_\perp r_{in})\right] \qquad \text{(Eq. 2.12)}$$

Thus, the predicted intensity scattered $I(\mathbf{Q})$ for a microtubule is

$$I(\mathbf{Q}) = ff^* = \left(\frac{2\pi\rho_0 J_0(Q_z H)}{Q_\perp} \left[(r_{in} + \delta) * J_1\big(Q_\perp(r_{in} + \delta)\big) - r_{in} * J_1(Q_\perp r_{in}) \right] \right)^2 \qquad \text{(Eq. 2.13)}$$

It is helpful to point out at this time that this would be the ideal scattering off of one microtubule, aligned in one particular direction. However, we are scattering not just off of one microtubule, but multiple microtubules oriented in all directions.

2.2.3. The Form Factor for Microtubules (Ensemble-Averaging)

Experimentally, X-ray scattering does not just probe one microtubule, but rather probes all microtubules in a volume defined by size of the X-ray beam hitting the sample. In practice, that means that the probed parameter r_{in} is actually the ensemble-averaged inner radius $\langle r_{in} \rangle$, which allows us to measure the average number of protofilaments in cross-section of the overall microtubule population. While the microtubule wall thickness δ is also being probed over the entire microtubule population, we take advantage of the fact that the wall thickness remains, more or less, constant for microtubules (as the protofilament thickness does not change).

Furthermore, our prior calculations for $I(\mathbf{Q})$ (Eq. 2.13) explicitly assumed that microtubules were aligned on one axis, while microtubules in solution are free to take any and all orientations. Thus, the predicted scattering of microtubules must be orientationally-averaged to account for all possible microtubule orientations, such that:

$$I(\mathbf{Q}) = \langle I(\mathbf{Q}) \rangle_{Orient.} = \frac{1}{4\pi} \int_0^\pi \int_0^{2\pi} I(\mathbf{Q}) \sin\theta \, d\theta \, d\phi \qquad \text{(Eq. 2.14)}$$

At this point, the utility of numerical integration becomes quite apparent.

2.2.4. The Structure Factor: Scattering off Lattices

The previous calculations assumed no positional correlations between the objects being scattered. However, if objects were to be arranged in a lattice, the resultant scattering of the lattice would be modulated, given certain conditions are met. For the sake of brevity, the derivation by Als-Nielsen and McMorrow[19] will be quickly demonstrated here, but a more in-depth explanation can be found in the source material. These new scattered intensities will result from the lattice sum (or structure factor) over positions in a 3D lattice, with the 3D lattice defined by:

$$\mathbf{R_n} = n_1 \mathbf{a}_1 + n_2 \mathbf{a}_2 + n_3 \mathbf{a}_3 \qquad \text{(Eq. 2.15)}$$

And the structure factor defined by:

$$S(\mathbf{Q}) = \sum_{\mathbf{R_n}} e^{i\mathbf{Q} \cdot \mathbf{R_n}} \qquad \text{(Eq. 2.16)}$$

Upon inspection, the terms which contribute most towards the sum will be when the phase factor $e^{i\mathbf{Q} \cdot \mathbf{R_n}}$ approaches unity, or when the following condition is satisfied:

$$\mathbf{Q} \cdot \mathbf{R_n} = 2\pi * \text{integer} \qquad \text{(Eq. 2.17)}$$

To find a solution, we need to construct a lattice in $\mathbf{Q}$ space such that

$$\mathbf{a_i} \cdot \mathbf{a_j^*} = 2\pi\delta_{ij} \tag{Eq. 2.18}$$

Where δ_{ij} is the Kronecker delta $(\delta_{i=j} = 1, \delta_{i \neq j} = 0)$. This reciprocal lattice can then be defined as:

$$\mathbf{G} = h\,\mathbf{a_1^*} + k\,\mathbf{a_2^*} + l\,\mathbf{a_3^*} \tag{Eq. 2.19}$$

with h, k, and l as integers. If we were to take the dot product of this reciprocal lattice with the 3D real-space lattice, we see that:

$$\mathbf{G} \cdot \mathbf{R_n} = 2\pi\,(h\mathrm{n}_1 + k\mathrm{n}_2 + l\mathrm{n}_3) \tag{Eq. 2.20}$$

By our initial definitions that n_1, n_1, n_1, h, k, and l all be integers, $(h\mathrm{n}_1 + k\mathrm{n}_2 + l\mathrm{n}_3)$ must also be an integer and thus the conditions set out in Eq. 2.17 is satisfied. Indeed, we see the lattice sum contribution is the greatest when $\mathbf{Q} = \mathbf{G}$, otherwise known as the Laue condition.

This Laue condition gives us the framework to solve for structure factor peaks, or where we would expect the lattice sum to contribute the greatest based off of the reciprocal lattice.

2.2.5. The Structure Factor: Scattering off 2D Hexagonal Lattices

While in 3-dimensions there are 14 lattices types[23], the extreme axial length of microtubules compared to its other dimensions means that effectively microtubules can only be found in 2D lattices. Of particular interest is 2D hexagonal lattice, with peak positions in $\mathbf{Q}$ space at:

$$\mathbf{G} = (h\text{-}k)\frac{2\pi}{\sqrt{3}d}\,\hat{q}_x + (h+k)\frac{2\pi}{\sqrt{3}d}\,\hat{q}_y \tag{Eq. 2.21}$$

with d corresponding to the hexagonal lattice parameter. While the scattered intensity is the product of the form factor multiplied with its complex conjugate and the lattice sum, we can choose a large enough Q such that the form factor is, more or less, constant. Then, if we were to orientationally-average (Eq. 2.14) the intensity as before, we find that the peak positions should lie at:

$$|\mathbf{G}| = \frac{4\pi}{\sqrt{3}d} \sqrt{h^2+k^2+hk} \qquad\qquad\qquad \text{(Eq. 2.22)}$$

With the first peak (the peak corresponding the h=1, k=0) occurring at

$$q_{10} = \frac{4\pi}{\sqrt{3}d} \qquad\qquad\qquad\qquad\qquad \text{(Eq. 2.23)}$$

The lattice symmetry of the objects being scattered cannot be determined from the first peak position alone, but peak positions must be compared (relative to each other) to see which geometry is appropriate. This becomes problematic when the scattering of the structure factor is convolved with that of the form factor, which can extinguish apparent structure factor peaks.

2.2.6. The Form and Structure Factor, Together (Convolution Theorem)

We know the form factor and structure factor to be the Fourier transform of the electron density (or more specifically, electron density difference) of the object (Section 2.2.1) and lattice (Section 2.2.5) being scattered, respectively. However, often we are not solely dealing with form factor or structure factor, but rather a combination of the two (i.e. a lattice of objects). Thus, in real-space, the

resultant system can be described by the convolution of an object and the lattice in which the objects are found (Fig. 2.5)

Figure 2.5| A system of scattering centers in a lattice can be mathematically described as the convolution ($\otimes$) of the scattering center with the lattice.

This mathematical description allows us to take advantage of the *convolution theorem*, which states that the Fourier transform of the convolution of two real-space function is the pointwise product of their Fourier transforms. In other words, to obtain the mathematical description of the form factor and structure factor simultaneously, we only need to multiple the two to obtain the desired mathematical result in **Q**-space. We will take advantage of this theorem, especially when fitting out X-ray scattering data.

2.3   References

1.   Ellis, R. J. Macromolecular crowding: Obvious but underappreciated. *Trends Biochem. Sci.* **26,** 597–604 (2001).

2.   Zhou, H.-X., Rivas, G. & Minton, A. P. Macromolecular crowding and confinement: biochemical, biophysical, and potential physiological consequences. *Annu. Rev. Biophys.* **37,** 375–97 (2008).

3.   Lekkerkerker, H. N. W. and Tuinier, R. *Colloids and the Depletion Interaction. Springer* **1-222, Ind,** (2011).

4.   Asakura, S. & Oosawa, F. Interaction between particles suspended in solutions of macromolecules. *J. Polym. Sci.* **33,** 183–192 (1958).

5.   Parsegian, V. A., Rand, R. P., Fuller, N. L. & Rau, D. C. Osmotic stress for the direct measurement of intermolecular forces. *Methods Enzymol.* **127,** 400–416 (1986).

6.   Zimmerman, S. B. & Trach, S. O. Estimation of macromolecule concentrations and excluded volume effects for the cytoplasm of Escherichia coli. *J. Mol. Biol.* **222,** 599–620 (1991).

7.   Brocchieri, L. & Karlin, S. Protein length in eukaryotic and prokaryotic proteomes. *Nucleic Acids Res.* **33,** 3390–3400 (2005).

8.   Jones, C. W., Wang, J. C., Ferrone, F. A., Briehl, R. W. & Turner, M. S. Interactions between sickle hemoglobin fibers. *Faraday Discuss.* **123,** 221–

236; discussion 303–322, 419–421 (2003).

9.   Israelachvili, J. N. *Intermolecular & Surface Forces*. (Academic Press Limited, 1992).

10.   Andreu, J. M. *et al.* Low resolution structure of microtubules in solution. *J. Mol. Biol.* **226,** 169–184 (1992).

11.   Tuinier, R. & Fleer, G. J. Concentration and solvency effects on the pair interaction between colloidal particles in a solution of nonadsorbing polymer. *Macromolecules* **37,** 8764–8772 (2004).

12.   Devanand, K. & Selser, J. C. Asymptotic Behavior and Long-Range Interactions in Aqueous Solutions of Poly (ethylene oxide). *Macromolecules* **24,** 5943–5947 (1991).

13.   Rand, R. P. Osmotic Stress. at <//www.brocku.ca/ researchers/peter_rand/osmotic/osfile.html#data>

14.   Beck, R., Deek, J., Jones, J. B. & Safinya, C. R. Gel-expanded to gel-condensed transition in neurofilament networks revealed by direct force measurements. *Nat. Mater.* **9,** 40–46 (2010).

15.   Chung, P. J. *et al.* Tau Mediates Microtubule Bundle Architectures Mimicking Fascicles of Microtubules found in the Axon Initial Segment. *Under Rev.*

16.   Chung, P. J. *et al.* Direct force measurements reveal protein Tau confers

short-range attractions and isoform-dependent steric stabilization to microtubules. *Proc. Natl. Acad. Sci.* **112,** E6416–E6425 (2015).

17. Nagahama, K., Inomata, H. & Saito, S. Measurement of osmotic pressure in aqueous solutions of poly(ethylene glycol) and poly(N-isopropylacrylamide). *Fluid Phase Equilib.* **96,** 203–214 (1994).

18. Warren, B. E. *X-ray diffraction. Analysis* **1,** (1990).

19. Als-Nielsen, J. & McMorrow, D. *Elements of Modern X-ray Physics: Second Edition. Elem. Mod. X-ray Phys. Second Ed.* (2011). doi:10.1002/9781119998365

20. Cullity, B. D. Elements of X-Ray Diffraction. *Am. J. Phys.* **25,** 394 (1957).

21. Needleman, D. J. *et al.* Radial compression of microtubules and the mechanism of action of taxol and associated proteins. *Biophys. J.* **89,** 3410–3423 (2005).

22. Choi, M. C. *et al.* Human microtubule-associated-protein tau regulates the number of protofilaments in microtubules: A synchrotron X-ray scattering study. *Biophys. J.* **97,** 519–527 (2009).

23. Chaikin, P. M. & Lubensky, T. C. *Principles of condensed matter physics. Biochem. Biophys. Res. Commun.* **67,** (2000).

3. Direct force measurements reveal Tau confers short-range attractions and isoform-dependent steric stabilization to microtubules[1]

Microtubules (MTs) are hollow cytoskeletal filaments assembled from αβ-tubulin heterodimers. The microtubule-associated protein Tau, an unstructured protein found in neuronal axons, binds to MTs and regulates their dynamics. Aberrant Tau behavior is associated with numerous neurodegenerative dementias including Alzheimer's. Here, we report on a direct measurement of forces between paclitaxel-stabilized MTs coated with distinct Tau isoforms by synchrotron small-angle-X-ray-scattering (SAXS) of MT-Tau mixtures under osmotic pressure (P). In going from bare MTs to MTs with Tau coverage near the physiological sub-monolayer regime (Tau/tubulin-dimer molar ratio, Φ_{Tau}=1/10), isoforms with longer N-terminal tails (NTTs) sterically stabilized MTs preventing bundling up to $P_B \approx$10,000-20,000 Pa, an order of magnitude larger than bare MTs. In contrast, Tau with short NTTs showed little additional effect in suppressing the bundling pressure ($P_B \approx$1,000-2,000 Pa) over the same range. Remarkably, the abrupt increase in P observed in the P-Φ_{Tau} phase diagram for longer isoforms suggest a mushroom-to-brush transition occurring between Φ_{Tau}=1/13 and Φ_{Tau}=1/10, which correspond to MT-bound Tau with NTTs that are considerably more extended than SAXS data for Tau in solution indicates. Modeling of Tau-mediated MT-MT interactions support the hypothesis that longer NTTs transition to a polyelectrolyte brush at higher coverages. Higher

---

[1] This section has been adapted with permission from Chung *et al*, Proceedings of the National Academy of Sciences 2015, **112**. Copyright 2015 National Academy of Sciences, USA

pressures resulted in isoform-independent irreversible bundling due to short-range attractions arising from the polyampholytic nature of Tau. These findings suggest an isoform-dependent biological role for regulation by Tau, with longer isoforms conferring MT steric stabilization against aggregation, either with other bio-macromolecules or into tight bundles, preventing loss of function in the crowded axon environment.

3.1. Introduction

Microtubules (MTs), a structural component of the eukaryotic cytoskeleton, are protein nanotubes involved in a range of cell functions including intracellular trafficking, cell motility, segregating chromosomes, and establishing cell shape[1,2]. MTs are composed of straight protofilaments (PFs), which are head-to-tail assemblies of globular $\alpha\beta$-tubulin heterodimers that self-organize with lateral PF-PF interactions stabilizing the hollow MT (Fig. 3.1a, left)[3–5]. MT structure and assembly dynamics are regulated and functionally differentiated *in vivo* by microtubule-associated proteins (MAPs)[1,6]. One MAP in particular, Tau (Fig. 3.1a, right), is primarily localized to the axons of mature vertebrate neurons[1,7]. While Tau is involved in numerous functions, which remain to be fully elucidated[8], a well-characterized function of Tau upon binding to MTs (Fig. 3.1a, left) in mature neurons is in the modulation of MT dynamic instability (i.e. cycles of slow polymerization and rapid disassembly) by

enhancing tubulin assembly while suppressing MT depolymerization[9–11]. This ensures proper trafficking of organelles along relatively stable MTs in axons[1,12–15]. Chemical modifications of Tau, including hyperphosphorylation and mutations leading to loss of function, have been implicated in Alzheimer's disease and a wide range of neurodegenerative disorders including Fronto-Temporal Dementia with Parkinsonism linked to chromosome 17 (FTDP-17), Pick's, supranuclear palsy[16–20], and, more recently, chronic traumatic encephalopathy (CTE) in athletes suffering concussions[21].

The human central nervous system generates six Tau isoforms as a result of alternative RNA splicing[22]. Tau structure is often described sequentially: the N-terminal tail (NTT) consists of a projection domain (PD, with no affinity for MTs and projecting off its surface[23,24]) and a proline-rich region (PRR, with weak affinity for MTs), then the microtubule-binding region (MTBR; a series of 3-4 18 amino acid long imperfect repeats separated from one another by 13-14 amino acid long inter-repeats), and finally a C-terminal tail (Fig. 3.1b)[25–28]. The number of imperfect repeats is determined by the excision or inclusion of exon 10 (leading to 3-repeat Tau or 4-repeat Tau, respectively) while the excision or inclusion of exons 2 and/or 3 determines the length of the projection domain, i.e., "short", "medium" or "long" (Fig. 3.1b). While all of the Tau isoforms are intrinsically disordered in solution[29], it is unclear whether or not the cationic domains in the repeat:inter-repeat region that specifically bind to the MT surface adopt folded structures upon attachment (Fig. 3.1a, left). While Tau

strongly binds to the MT surface ($\approx$1-3 µM affinity)[10,26], recent work suggests Tau-MT interactions are highly dynamic and that Tau can assume numerous structures[30,31].
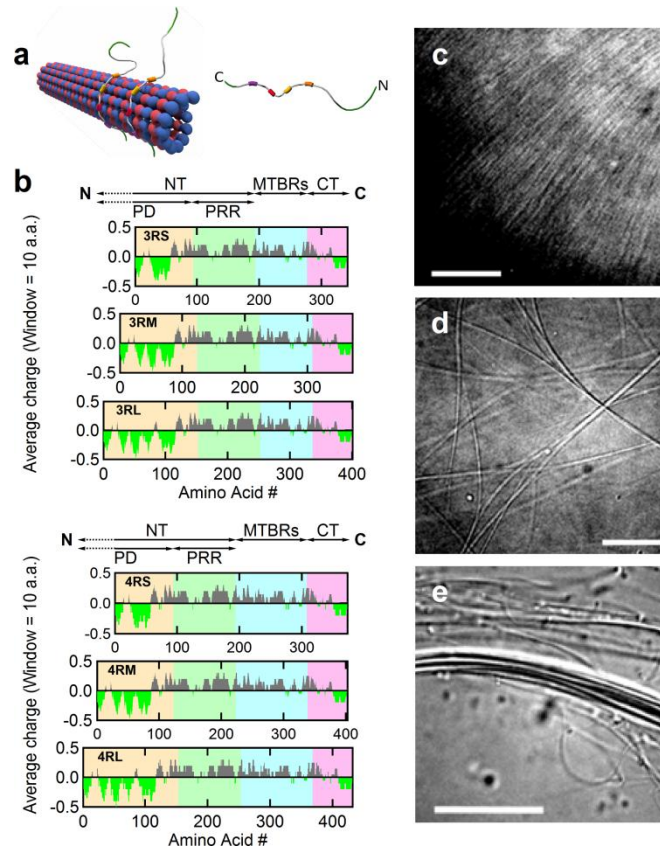
Fig. 3.1| MAP Tau binds to the microtubule surface and modulates the higher-order structure of microtubules with increasing osmotic pressure. (**a**) Schematic of a microtubule with bound Tau protein (left) and a single Tau protein (right, labeled with N- and C- terminus ends) with four MT-binding repeats (colored boxes). (**b**) Charge (averaged over 10 residues) versus amino acid residue number for six isoforms of human Tau. The charge distribution diagram of each isoform shows the cationic (grey) nature of Tau with the exception the amino- and carboxyl- terminal tails which include anionic (bright green) regions, which lead to dipole-like characteristics. The N-terminal (NT) is made up of the projection domain (PD, yellow background, first 92, 121, and 150 AAs for -S, -M and -L isoforms) and proline-rich region (PRR, green background, next 94 AAs), followed by MT-binding region (MTBR, blue background), and ending at the carboxyl-terminus (C) with the C-terminal (CT, pink background). Tau isoforms have either 3 or 4 microtubule-binding repeats (3R-, 4R-) as a result of excluding

(or including) exon 10 (33 amino acids), which contains second microtubule-binding repeat and the interrepeat region between first and second repeat. Additionally, the exclusion of exons 2 and 3 (both 29 amino acids), exclusion of exon 2, or no exclusions in the PD result in the short (-S), medium (-M), or long (-L) isoforms, respectively. (c, d, e) Differential interference contrast microscopy of samples at Φ_{3RL}=1/40 show the presence of an unbundled (c) and two distinct bundled phases (d, e) at 0, 1, and 10 wt% of 20k PEO, respectively.

Previous synchrotron small-angle-X-ray-scattering (SAXS) work revealed that increasing coverage of paclitaxel-stabilized MTs by any of the six Tau isoforms led to an increase in the average number of protofilaments in MTs [32]. This increase in the ensemble-averaged inner radius of MTs, $<R_{in}^{MT}>$, indicated that MAP Tau isoforms do not just bind and stabilize MTs, for example, by enhancing PF-PF interactions, but also change the shape of αß-tubulin and thus PFs, leading to a change in curvature of MTs. This conclusion is consistent with recent NMR work demonstrating that Tau binds, at least in part, between tubulin heterodimers[31].

While Tau affects tubulin shape and inter-αβ-tubulin interactions within individual MTs, much less is known about how MT-bound Tau modifies inter-microtubule forces. This study focuses on elucidating the structure and interactions of paclitaxel-stabilized MTs[33–35] assembled at varying Tau/tubulin-dimer molar ratios (Φ_{Tau}= 1/10, 1/13, 1/20, 1/40, 1/100, spanning the physiological range observed in axons[36]) using synchrotron SAXS in the presence of an osmotic depletant. By varying osmotic pressure (induced by 20k polyethylene oxide, or 20k PEO) and Tau-grafting density (Tau per MT-outer surface area[32], controlled by Φ_{Tau} as Tau binds stoichiometrically to MTs up until

$\Phi_{Tau} \approx 1/5$), the force response of Tau-coated MTs was directly measured via SAXS line-shape analysis[37]. Previous literature noted the functional dependence of the carboxyl-terminal MTBR of Tau in stabilizing individual MTs[26–28], but herein we present data demonstrating that inter-MT forces are functionally dependent on and regulated by the N-terminal tail projection domain of Tau. Specifically, at $\Phi_{Tau} = 1/10$, isoforms with longer projection domains suppressed MT bundling pressures by an order of magnitude more than bare MTs and MTs with short projection domain isoforms of Tau. This result indicates a gain of function of Tau isoforms with longer NTTs (by longer projection domains) in adopting brush-like conformations at higher coverages to impart steric stabilization to individual microtubules. This is in striking contrast to other neuronal cytoskeletal systems, such as the protruding long sidearms of neurofilaments, which have been found to always be in a brush-like phase with no observed subunit composition-dependence on sidearm conformation[38,39]. In the high-pressure limit, where Tau chains from opposing MT surfaces are osmotically forced to interpenetrate, irreversible MT bundling was observed, which was attributed to the polyampholytic nature of Tau leading to short-range attractions between anionic/cationic residues on neighboring Tau chains.

3.2.   Results and Discussion

3.2.1. Phase behavior of MT/Tau mixtures under osmotic pressure

Structurally distinct higher-order phases of paclitaxel-stabilized MTs co-assembled with Tau at different P were initially observed by video-enhanced differential-interference-contrast (DIC) microscopy (Fig. 3.1c-e). Consistent with previous results without Tau[40,41], MTs at high concentration undergo a transition from an orientationally ordered nematic state (N_{MT}, Fig. 3.1c) to two distinct higher-ordered bundled phases (Fig. 3.1d,e) as a function of increasing osmotic pressure. The bundled phases result from PEO-induced depletion attraction. The internal structure of these higher-ordered phases at different Tau coverages was elucidated with *in situ* SAXS-osmotic pressure measurements. Line-shape analysis of azimuthally-averaged SAXS data of the samples (Fig. 3.2) revealed three distinct phases, correlating to the distinct structures seen in DIC microscopy. Fig. 3.2d shows SAXS profiles with increasing P in mixtures of MTs and 4RS Tau at Φ_{4RS} = 1/10. At low osmotic pressures (Fig. 3.2d bottom profile, 0 to 0.46 wt% of 20k PEO), where DIC shows the N_{MT} phase, fits of background-subtracted scattering corresponded to a hollow-cylinder form factor, with inner radii (~8 nm) and cylinder thickness (4.9 nm) consistent with electron microscopy data of MTs[42]. This behavior is similar to previous reports of bare MTs where SAXS profiles of the N_{MT} phase shows no evidence of a correlation peak[5,32,40,41,43,44]. At intermediate osmotic pressures (~1-3 wt% of 20k PEO), where DIC shows bundled MTs (Fig. 3.1d), a scattering

structure factor was readily apparent with more than five orders of diffraction peaks indexed to a 2D rectangular lattice (Fig. 3.2d, labeled R^B_{MT} at 1.63 wt% PEO). SAXS studies of bare MTs[40] have shown that the rectangular symmetry results from the buckling of MTs, from circular to non-circular in cross-section, because the larger PEO concentration on the outside compared to the inside lumen of MTs produces an excess pressure on the MT wall (Fig. 3.2b). The gradient is expected because the radius of gyration of 20k PEO $\approx$ 6.9 nm is close to the inner radius of MTs[45] and at these intermediate concentrations PEO does not readily enter the lumen due to an entropic confinement penalty.
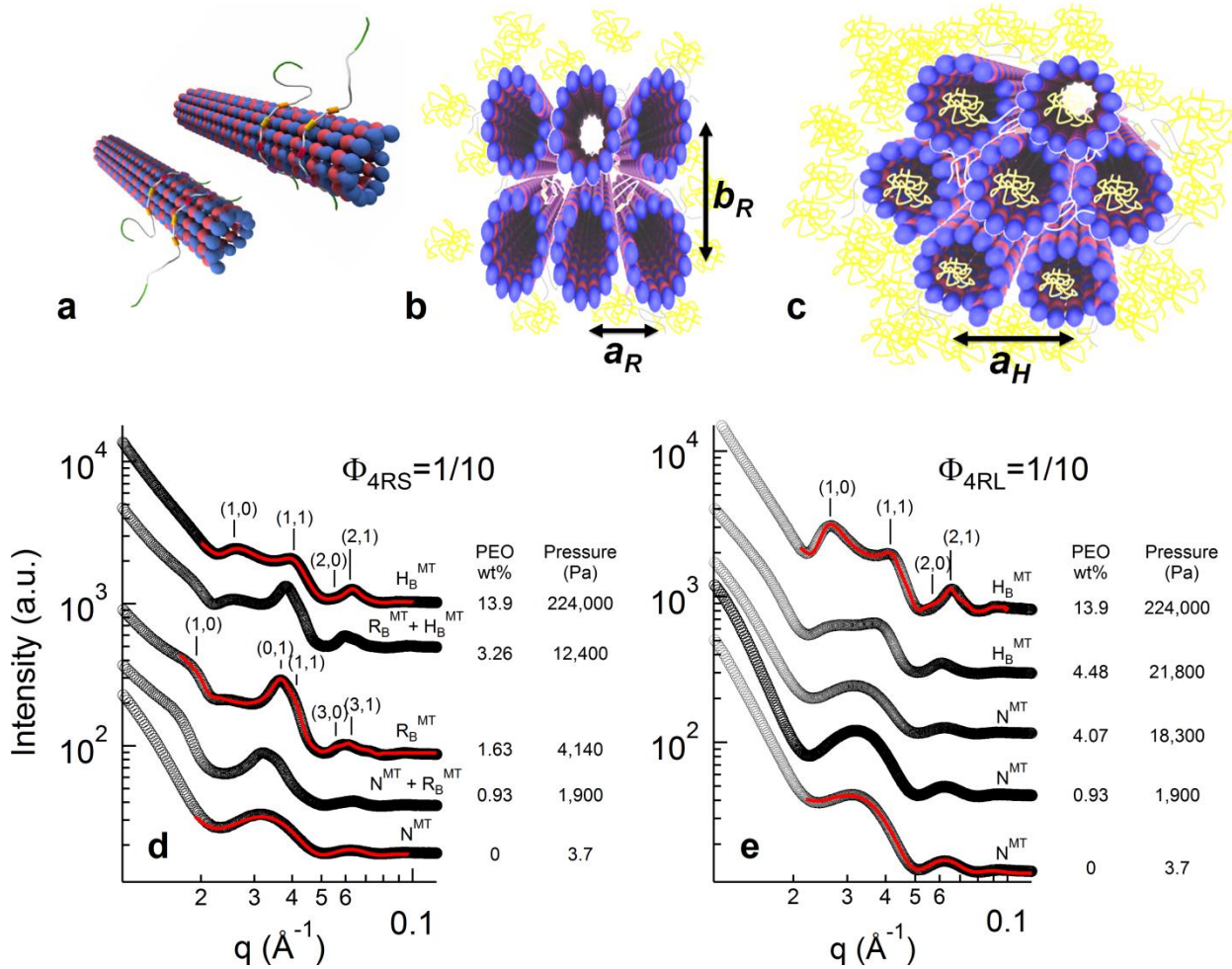
Fig. 3.2 | **Microtubule bundling transitions with increasing osmotic pressure are Tau isoform and concentration dependent.** (a, b, c) Schematic of the (a) nematic (N_{MT}, with orientational order and no positional order), (b) buckled rectangular bundle (R^B_{MT}, characterized by the rectangular lattice constants a_R and b_R), and (c) hexagonal bundle (H_{MT}, characterized by the hexagonal lattice constant a_H) phases of Tau-MTs, with PEO colored in yellow. (d, e) Azimuthally averaged synchrotron SAXS data of Tau-MTs plotted as a function of increasing osmotic pressure induced by 20k PEO, with PEO concentration and corresponding pressure shown next to each profile. A reaction mixture (d), $\Phi_{4RS}=1/10$ (4RS Tau/tubulin-dimer molar ratio), exhibits an osmotic pressure-induced phase transition from nematic (N_{MT}) to buckled rectangular (R^B_{MT}, $a_R=17.0$ nm and $b_R=30.7$ nm) and from buckled rectangular to hexagonal (H_{MT}, $a_H=30.2$ nm), with coexistence regimes between two phases. However, another mixture (e, $\Phi_{4RL}=1/10$) displays a transition from nematic (N_{MT}) to hexagonal (H_{MT}, $a_H=29.3$ nm) phases, bypassing the buckled rectangular phase entirely. SAXS data was analyzed and presented fit parameters extracted with fitted model scattering curves (red lines) corresponding to the model appropriate structure and form factor, as described in text.

43

At higher osmotic pressures (~3-14 wt% of 20k PEO), the Bragg diffraction peaks could now be indexed to a 2D hexagonal bundled phase with lattice parameter a_H (Fig. 3.2d, labeled H_{MT} at 13.9 wt% PEO). The structural transition at higher P from the R^B_{MT} (Fig. 3.2b) to the H_{MT} (Fig. 3.2c) results from a transition from buckled (non-circular) to unbuckled (circular) MTs. The unbuckling occurs at concentrations near the chain overlap concentration ($c^* \approx$ 7.5 wt% for 20k PEO) where the external crowding of PEO eventually forces PEO chains to enter the MT lumen[46,47] and thus equalizing the outside/inside pressure on MTs. The absence and presence of 20k PEO in the MT lumen in the R^B_{MT} and H_{MT}, respectively, has been directly confirmed with labeled PEO in fluorescence microscopy studies of bare MTs with increasing osmotic pressure[40,41].

For most samples the scattering from one phase clearly dominated, but samples at certain Tau coverages and osmotic pressures exhibited scattering from coexisting phases (N_{MT} + R^B_{MT}, R^B_{MT} + H_{MT}). Generally, MTs transitioned from N_{MT} to the R^B_{MT} and finally to the H_{MT} under increasing osmotic pressure, as it did for Φ_{4RS}=1/10 (Fig. 3.2d). Strikingly, for Tau isoforms with longest PDs (3RL, 4RL), R^B_{MT} was entirely bypassed at the highest Tau coverage (i.e. N_{MT} transitioned directly to the H_{MT}). Fig. 3.2e shows SAXS profiles for 4RL Tau at Φ_{4RL}=1/10 where the N_{MT} remains stable well into the intermediate osmotic pressure range with MT bundling being suppressed up to P_B = 21,800 Pa (= 4.48 wt% 20k PEO) before transitioning to the bundled H_{MT}. This is in contrast to

SAXS data for Tau isoforms with short PDs, which undergo bundling at nearly an order of magnitude lower P_B (Fig. 3.2d, profile at P = 1,900 Pa, 0.93 wt% 20k PEO). To fully elucidate the Tau isoform-dependence of MT bundling we mapped out the phase behavior by systemically altering all relevant variables (Tau isoform, Tau/tubulin-dimer molar ratio, and osmotic pressure).

The osmotic pressure – Tau/tubulin composition (P-Φ_{Tau}) phase diagram of all six wild-type Tau isoforms is shown in Fig. 3.3, revealing regions of stability for unbundled N_{MT} and bundled R^B_{MT} and H_{MT}. All three structural phases (either singularly or in co-existence) were exhibited at all concentrations for Tau isoforms with the short PD (Fig. 3.3a, 3.3d). However, Tau isoforms with the longest PDs (3RL, 4RL) suppress the R^B_{MT} at high Φ_{Tau} (Fig. 3.3c for Φ_{3RL} = 1/10, Fig. 3.3f for Φ_{4RL} = 1/13 and 1/10). Tau isoforms with medium length PDs (3RM, 4RM) also show a much narrower pressure range for the R^B_{MT} for $\Phi_{3RM,4RM}$ =1/13 and 1/10 (Fig. 3.3b,e).

Remarkably, the phase diagram reveals that at the highest coverages of Tau with longer PDs ($\Phi_{3RM,4RM}$=1/10 and $\Phi_{3RL,4RL}$=1/10 and 1/13, both near the physiological regime), significantly higher osmotic pressures are required to stabilize microtubules against bundling (P_B~10,000 Pa and P_B~20,000 Pa at Φ=1/10 for –M and –L isoforms, respectively). This is in marked contrast to Tau with short PD, which seems to have little effect on the bundling pressure (P_B~1,000 Pa) at all measured coverages. The dramatic increase in pressure strongly indicates that the conformation of the medium and long PDs have

transitioned from a "mushroom" state (Fig. 3.3g, left) to a "brush" state (Fig. 3.3g, right). This would give rise to an enhanced repulsive force of substantial magnitude between MTs, requiring much higher osmotic pressures to overcome that repulsion and bundle.
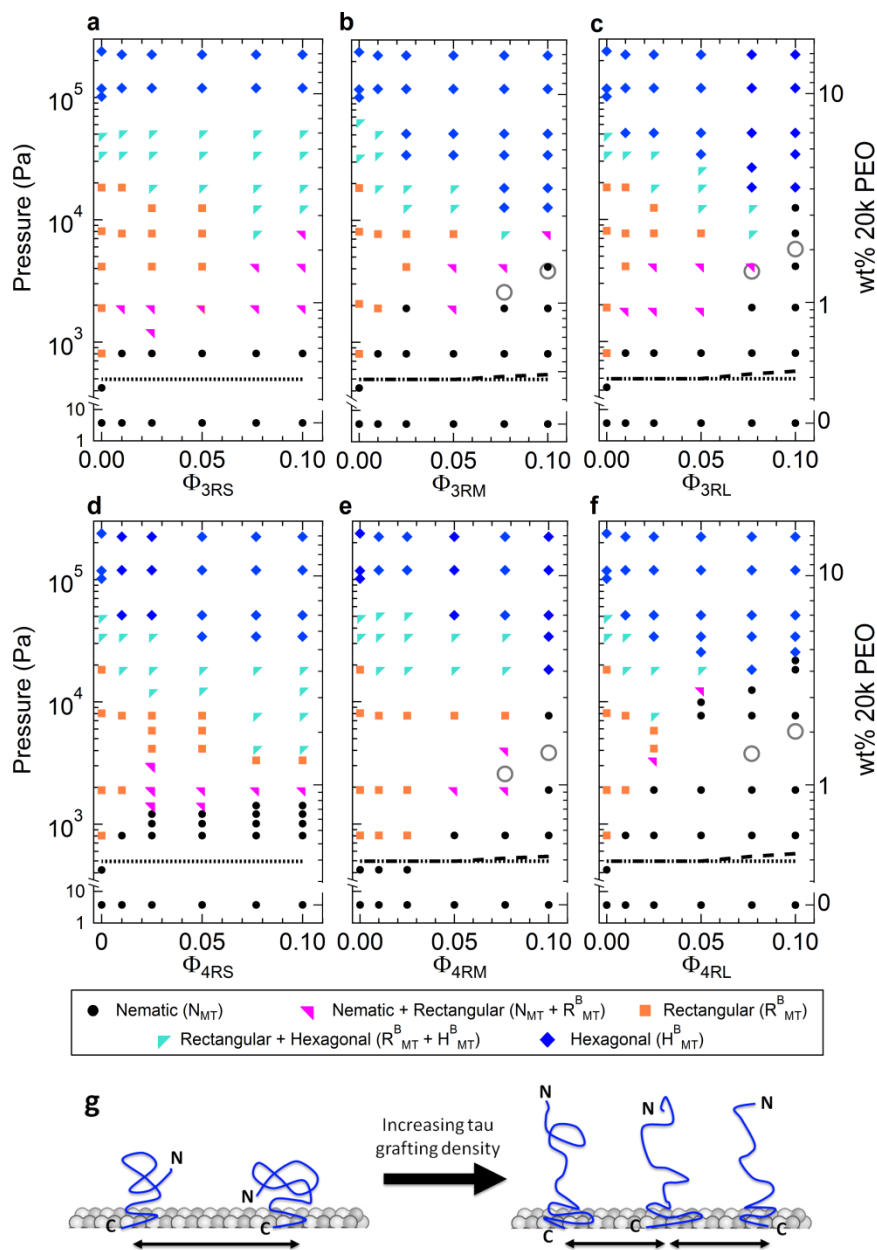

Fig. 3.3| Osmotic pressure against Tau/tubulin concentration phase diagram for all six Tau isoforms. (a-f) MT/Tau phases, determined by SAXS analysis, plotted

as a function of increasing osmotic pressure (left Y-axis) induced by increasing wt% of 20k PEO (right Y-axis, which has independent Log domains to match PEO concentrations) against various Tau/tubulin-dimer molar ratios (Φ_{Tau}) of 3RS (a), 3RM (b), 3RL (c), 4RS (d), 4RM (e), and 4RL (f) isoforms of Tau. The observed phases were nematic (N), buckled rectangular (R^B_{MT}), hexagonally bundled (H_{MT}) phases, or regions of phase coexistence. For isoforms with the longer projection domain (M- and L-), the microtubule bundling pressure, P_B, increased abruptly at higher Tau coverages (Φ_{Tau}= 1/10). Notably, increasing Tau coverage of the 3RS and 4RS isoforms of Tau show little effect in affecting the MT bundling pressure. As described in text, the lines/open circles in the phase diagram correspond to the expected P_B for the soft-cylinder model for bare MTs (dotted line), charged soft-cylinder model for selected Tau isoforms (–M and –L) bound to MTs (dashed line), and the charged brush model for Tau for selected Tau isoforms (–M and –L) at the highest coverages (Φ_{Tau}=1/10, 1/13, grey open circles). (**g**) Cartoon depicting the mushroom (left) and brush (right) states of Tau's N-terminal tail with increasing grafting density.

Classically, polymers undergo a mushroom-to-brush transition when the grafting distance between polymers is comparable to the diameter of the tethered polymer. Using SAXS[48], the physical diameter of the medium and long PDs in solution was shown to be ~10 nm (in similar buffer conditions to those used in our study). This physical diameter was calculated as twice the physical radius, which is proportional to the radius of gyration[49] ($D_{Phys.}=2R_{Phys.}=2(5/3)^{1/2}R_g$). The radius of gyration for unstructured proteins was found[50] to fit the Flory equation R_g=0.1927N$^{0.588}$ nm, which for the projection domains of –M and –L isoforms (N$_{PD}$=121, 150) is 3.30 nm and 3.75 nm, respectively (in agreement with SAXS measurements of the PD in solution[48]), giving us D$_{Phys}$=8.5 nm (-M) and 9.6 nm (-L). This follows previous measurements from SAXS (R_g=6.5 nm)[51], dynamic light-scattering (R_g=6.6 nm)[51], and Monte Carlo simulations (R_g=6.5 nm)[52] that confirm the R_G of isolated 4RL

Tau in solution scales as a random-coil conformation protein. However, the grafting distance, $d_g^{Tau} = 4.5*(\Phi_{Tau}/2)^{-1/2}$ nm (4.5 nm is the average tubulin monomer-monomer distance and the factor of 2 arises because Φ is a Tau to tubulin-dimer ratio), at the lowest Φ_{Tau} where the abrupt increase in bundling pressure is observed ($\Phi_{3RM,4RM}$=1/10 and $\Phi_{3RL,4RL}$=1/13) corresponds to d_g^{Tau} = 20.3 and 23.1 nm for –M and –L isoforms of Tau, respectively. Both grafting distances are considerably larger than the physical diameter, indicating that the Tau PD protruding away from the MT surface, at grafting densities prior to the transition to the brush state, is considerably more extended than the PD in solution.

3.2.2.   Modeling the interaction potential of MTs with MAP Tau

To elucidate the distinct contributions of the -M and -L Tau isoforms with longer projection domains (PDs, Fig. 3.1b) in suppressing bundling at higher osmotic pressures, we modeled the pairwise potential energy between two microtubules in the absence and presence of Tau. The model presented here balances the repulsive interactions (due to the overall anionic MT and the PD of surface-adsorbed Tau) against the depletion attraction resulting from the addition of PEO (i.e. the PEO-induced osmotic pressure, which effectively forces MTs together).

The overall bare charge of α- and β- tubulin (summing over negative and positive charged residues including CTTs and bound nucleotides/ions) is -21.7e and -22.6e at pH 6.8, respectively (NCBI protein database: NP_001159977.1, NP_001040014.1). The α- and β- tubulin CTTs, which contain either neutral or negative residues, have a bare charge of -9e and -11e, respectively[53]. Due to the high charge of tubulin and its CTT, partial counterion neutralization of tubulin is expected; indeed, previous work[54] measured an effective charge of -23e per dimer (via microtubule electrophoretic movement in microchannels) against a calculated bare charge of -50e per dimer at pH 6.9. This gave an effective charge renormalization prefactor $r = Q_{eff}/Q_{bare} = 0.46$, which was subsequently used in our calculations. The repulsive electrostatic potential energy between two MTs with wall-to-wall separation H may then be written in terms of a contribution from the renormalized charge of the CTTs and, separately, from the remaining renormalized charge of αβ-tubulin dimers:

$$V_{MT}^{Repulsive}(H) = V_{cyl}^{hard\ MT}(H) + V_{cyl}^{soft\ CTT}(H) \qquad \text{(Eq. 3.1)}$$

The first term in Eqn. 3.1) describes the electrostatic repulsion between MTs modeled as hard cylinders with mean surface charge density $\sigma = \sigma_{Tub\text{-}CTT} = -0.387e$ nm^{-2} due to the renormalized charge of αβ-tubulin dimers minus the charge of the CTTs. Thus, we write[55]:

$$V_{cyl}^{hard}(H) = \frac{2\sqrt{\pi R}\sigma^2}{\varepsilon_r \varepsilon_0 \kappa^{3/2}} Li_{1/2}(e^{-\kappa H}) \qquad \text{[Energy/Length]} \qquad \text{(Eq. 3.2)}$$

In Eq. 3.2, $\kappa = 1/\lambda_D$ with λ_D the Debye-Hückel screening length (0.85 nm in our experiments), $\varepsilon_r \varepsilon_0$ is the permittivity, and $Li_{1/2}(z) = \sum_{k=1}^{\infty} z^k / k^{1/2}$ is the polylogarithm function of order ½. The second term in Eq. 3.1 takes into account the contribution of the CTTs modeled as "soft cylinders" (i.e. where the charge of the CTTs is distributed within a layer of thickness L around the MTs), giving rise to a soft repulsive potential[56]:

$$V_{cyl}^{soft\,CTT}(H) = \frac{2\sqrt{\pi R}\rho^2}{\varepsilon_r \varepsilon_0 \kappa^{7/2}} \sinh^2(\kappa L) Li_{1/2}(e^{-\kappa H}) \quad \text{H>2L} \qquad \text{[Energy/Length]} \qquad \text{(Eq. 3.3)}$$

R = 12.5 nm is the MT outer radius and $\rho = -\,rfNe/(d_g^2 L)$ is the charge density (charge/volume) of the polyelectrolyte layer, where r = 0.46 is the charge renormalization factor, e is the elementary charge, $f \approx$ ½ is the net ionization fraction of CTTs[53], N =19.5 is the mean number of residues in the CTTs, d_g = 4.6 nm is the grafting distance between CTTs, and $L \approx$ 4.0 nm is the mean height of the CTTs[57]. For separations H<2L, where the polyelectrolyte layer is compressed, L is replaced by H/2 in Eq. 3.3. In this equation, the added salt leads to the presence of a double layer and the exponential screening of the electrostatic interactions between the polyelectrolyte-grafted surfaces.

The total effective interaction potential between bare MTs in the presence of PEO may be written as:

$$V_{MT}^{Total}(H) = V_{cyl}^{\text{hard MT}}(H) + V_{cyl}^{\text{soft CTT}}(H) + V_{Depletion}(H) \qquad \text{(Eq. 3.4)}$$

The third term is the depletion attraction between cylinders (energy per unit length) due to the presence of non-interacting 20k PEO polymer "depletants" with an effective radius $a = 2R_g/(\pi)^{1/2} \approx 7.8$ nm, with $R_g = 6.9$ nm for 20k PEO[58,59]:

$$V_{\text{Depletion}}(H) = -\Pi\, A(H,R,a) \qquad\qquad 0 < H \leq 2a \qquad\qquad \text{(Eq. 3.5)}$$

Here, $A(H,R,a) = (a+R)^2(\Theta - \sin(\Theta))$ is the overlap in the excluded area, (where $\Theta = 2\sin^{-1}\left(\dfrac{\sqrt{(2a-H)(2a+H+4R)}}{2(a+R)}\right)$), and Π is the osmotic pressure of the depletant, including second and higher order virial-coefficients to account for deviations from the ideal gas derivation for depletion attraction. For 20k PEO, measurements of Π (Pa) fit an empirical expression, $Log_{10}(\Pi) = .57 + 2.75*(PEOwt\%)^{.21}$ where *PEOwt%* is the wt% of 20k PEO[37,60]. For $H > 2a$ depletion attraction vanishes as the overlap in the excluded area term $A(H,R,a)$ is zero.
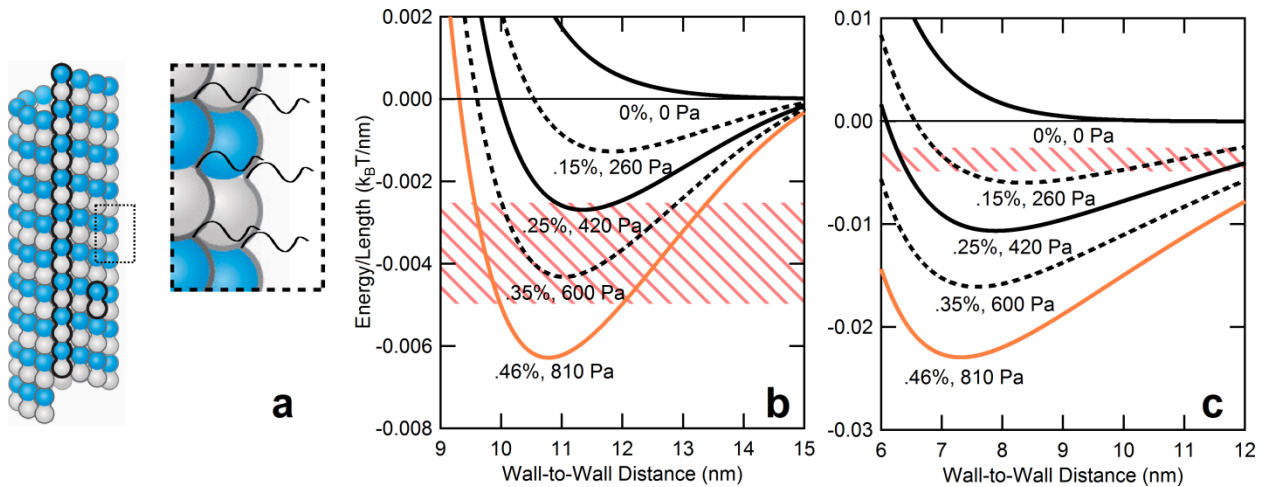
Fig. 3.4 | **Modeling MT-MT interactions requires more than a simple charged cylinder model.** (**a**) Schematic of bare MT and expanded view showing negatively charged C-terminal tails of α- and β- tubulin. The presence of C-terminal tails on the MT surface requires the model to incorporate a "soft" polyelectrolyte layer above the surface of the MT. (**b**) Curves derived from the soft-cylinder model

plotted for actual PEO wt% used in experiments (solid lines) and in-between concentrations (dashed lines). Colors (from black to orange) are coordinated with data in Fig. 3.3 (Φ_{Tau}=0). The pink-striped zone corresponds to a potential depth of 5 to 10 k_BT for 2 μm MTs (see Fig. 3.10 for MT length distribution) where one would expect MT bundling. The orange curve which falls in this zone corresponds to the lowest pressure where MT bundles are observed in the absence of Tau (see Fig. 3.3). (c) Assuming the same potential depth (pink-striped zone, 5 to 10 k_BT for 2 μm length MTs) for MT bundling, the charged hard-cylinder model (i.e. all tubulin charge on the surface) predicts bundling at lower PEO concentrations compared to what is observed experimentally (between 0.25 and 0.46 wt% PEO).

Figure 3.4b is a plot of V_{MT}^{Total} (*H*)/length versus *H* as a function of increasing wt% 20k PEO. The solid curves (color coordinated with data points in Fig. 3.3) correspond to experimental PEO concentrations studied and the dashed curves to in-between PEO concentrations. We see that with increasing PEO concentration the potential curve begins to develop a well defined minimum with a bound state and depth of 5 to 10 k_BT (where MT bundles may be expected to be stable) appearing between ≈ 0.30 wt% and ≈ 0.5 wt% of 20k PEO. We see in Fig. 3.3 that the onset of MT bundling at $\Phi_{Tau} = 0$ is between 0.25 wt% and 0.46 wt% 20k PEO concentrations (*P* between 420 Pa and 810 Pa), in reasonable agreement with the MT model that takes into account the added repulsion from the short polyelectrolyte CTTs. (The horizontal dotted line in Fig. 3.3 (a-f) corresponds to the pressure where the depth of the potential between MTs (Eq. 3.4) is 7.5 ± 2.5 k_BT.) Figure 3.4c shows that if one ignores the CTTs and models MTs as charged hard cylinders with mean surface charge density σ = σ_{Tub} = -0.497 e nm^{-2} then the potential curve develops a minimum at much lower PEO

concentrations and predicts that bundling with a potential depth ≈ 7.5 k_BT would occur as low as ≈ 0.15 wt% PEO, significantly lower than the experimentally observed bundling between 0.25 wt% and 0.46 wt% PEO. (The potential energy curves in Fig. 3.4c are calculated from the first and third terms in Eq. 3.4 assuming the renormalized net negative charge of αß-tubulin dimer (-44.3e per dimer, including the CTTs) is located on the surface of the hard cylinder)

To model the contribution of Tau isoforms with longer projection domains (as the short projection domain showed no appreciable change in P_B) to the MT-MT interaction potential energy we considered the overall anionic projection domain (PD) of the N-terminal tail (NTT) (Fig. 3.1b) to be extended away from the negative MT surface with the remaining weakly-positive proline-rich region (PRR) of the NTT being very weakly-bound in a pancake-like conformation[61] near the surface (consistent with NMR spectroscopy[31]) with a height of ~1 nm, in agreement with simulation[62,63] and AFM experiments[64]. The PRR, MT-binding region, and C-terminal tail were taken to contribute to the overall charge of αß-tubulin dimers.

We first estimated Tau's contribution (with Tau's PD in the mushroom conformation, Fig. 3.3g, left) within the soft potential model described above. The total potential considered (V_{MT+Tau} soft) used the soft potential term for the PD, Eq. (4), with $r=1$, where charge renormalization is not required because the combination of a low net ionization ($f_{net} \approx 0.1$) of PD and the low Tau coverage

results in a low charge density polyelectrolyte layer surrounding the microtubule. Furthermore, the V_{cyl} $^{hard\ MT}$ (H) term incorporated the modified surface charge density $\sigma = -0.387 + 0.253*\Phi_{Tau}$ (e nm^{-2}) accounting for the renormalized, reduced negative charge (i.e. the charge of tubulin-dimer minus the charge of the CTTs (-0.387e nm^{-2}) plus the added charge from Tau without the PD ($0.253*\Phi_{Tau}$ e nm^{-2} for $0 \leq \Phi_{Tau} \leq .1$). For the soft potential, Eq. 3.3 was used with the appropriate substitutions for parameters related to the PD: (f, N_{PD}, L_{TauPD}) = (0.120,121,20.1 nm) and (0.120,150,23.1 nm) for the medium (-M) and (-L) tau isoforms, respectively. Here, f is the net ionization fraction of the PD, N_{PD} is the degree of polymerization of the PD, and L_{TauPD} is the height of the PD. The Φ_{Tau} at which the mushroom-to-brush transition (Fig. 3.3g) occurs gives us an estimate for the polyelectrolyte layer height of the longer PDs. As discussed in the previous section, the lowest Φ_{Tau} where the transition is observed ($\Phi_{3RM,4RM} = 1/10$ and $\Phi_{3RL,4RL} = 1/13$) corresponds to a $d_g^{Tau} = 20.3$ and 23.1 nm for –M and –L isoforms of Tau, which we used for L_{TauPD}.

Figure 3.5 (a,b) shows V_{MT+Tau} ^{soft}/k$_B$T versus H for 3RM and 3RL isoforms plotted with increasing wt% 20k PEO (0.46, 0.93, 1.63, 2.44) and (0.46, 0.93, 1.63, 2.44, 3.26, 4.07) for the higher Tau coverages Φ_{Tau} = 1/13, 1/10, respectively. These PEO concentrations correspond to the lower range of PEO wt% data shown in Fig. 3.3. The potential curves with depth between 5 $k_B T$ and 10 $k_B T$ (where one would expect bundling) are predicted to occur even for the lowest concentration ≈ 0.46 wt% PEO while bundling at these higher Tau

coverages requires much larger PEO concentrations as seen in Fig. 3.3 (the pink striped lines in Fig. 3.5 a-d correspond to a potential depth of 7.5 ± 2.5 $k_\mathrm{B}T$ for MTs with average length of 2 μm). Although the soft potential model predicts a slight increase in repulsion from the Tau PD (and subsequent increase in wt% of PEO to bundle MTs), the difference is minor compared to MTs without Tau (the dashed lines versus the dotted lines in Fig. 3.3b,c,e,f) and fails to capture the dramatic increase in osmotic pressure required to bundle MTs assembled with the longer -M and -L isoforms at higher coverages (Φ_Tau=1/13, 1/10). For the 3RS isoform the MT interaction potential within the soft potential model ($V_\mathrm{MT+Tau}{}^\mathrm{soft}$) is dominated by the high density CTTs, which make a larger contribution than the 3RS PD in this coverage range.
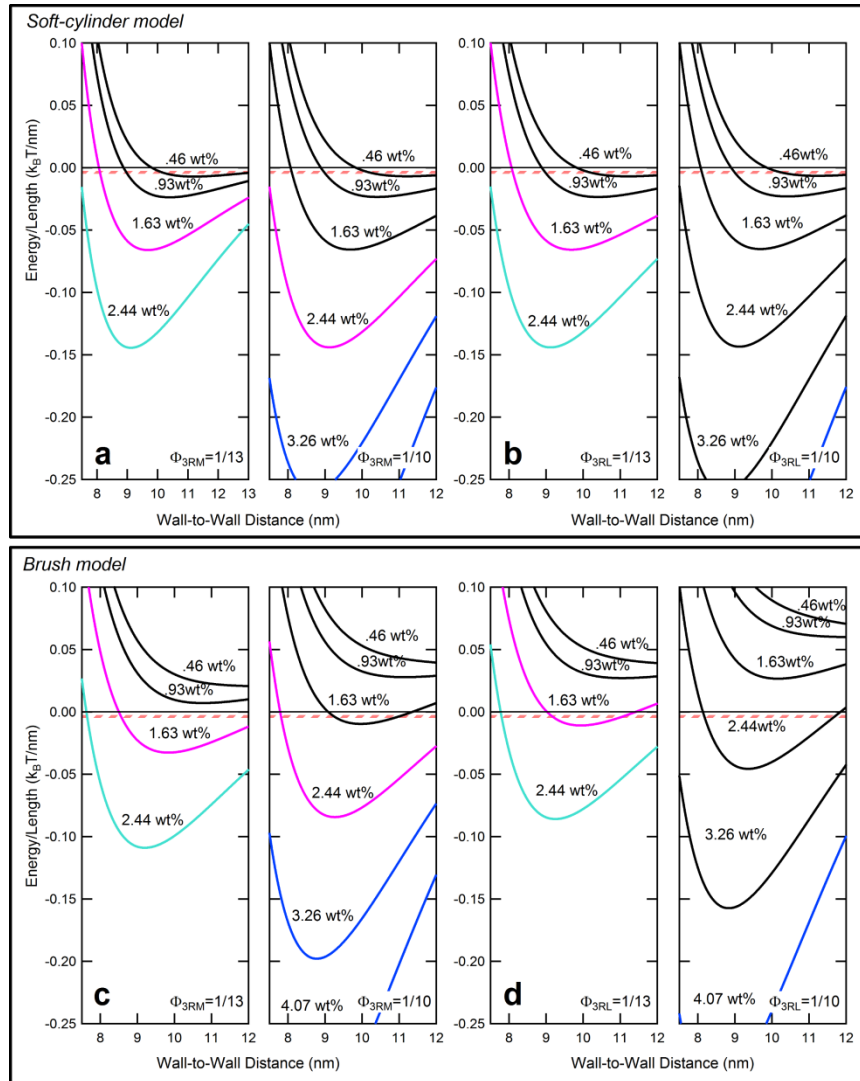
Fig. 3.5| The charged brush model for tau isoforms with longer (-M, -L) projection domains better captures the bundling behavior of MT/tau mixtures at higher tau coverages (Φ_{Tau}=1/13, 1/10). (**a-d**) Potential energy curves plotted for high coverages of $\Phi_{3RM,3RL}$=1/13 and $\Phi_{3RM,3RL}$=1/10 using the soft-cylinder model (a, b) and the charged brush model (c, d), as discussed in the text. The curves are for [0.46, 0.93, 1.63, and 2.44] wt% PEO for $\Phi_{3RM,3RL}$=1/13 (left panels, a-d) and [0.46, 0.93, 1.63, 2.44, 3.26, and 4.07] wt% PEO for $\Phi_{3RM,3RL}$=1/10 (right panels, a-d). The concentrations are those used in experiments and the curves are color coded as in Fig. 3.3 where the first colored curves indicates the PEO concentration where bundling is first observed (see Fig. 3.3, Φ_{Tau}=1/13, 1/10 for -M, -L isoforms). The pink-striped zone corresponds to a potential depth of 5 to 10 k_BT for 2 μm MTs (see Fig. 3.10 for MT length distribution) where one would expect MT bundling. Comparison between the model shows that the charged-brush model for the projection domain (c, d) gives better qualitative agreement between theory and experiment compared to the soft-cylinder model (a, b).

The soft potential model (dashed lines in Fig. 3.3c,d,e,f) is not able to account for the dramatic increase in the bundling pressure, which suggests a polyelectrolyte brush model would be more appropriate for Tau with the longer PDs at high coverage (Φ_{Tau}=1/13, 1/10). We note that L_{TauPD} (20.3 and 23.1 nm for –M and –L isoforms of Tau, respectively) used is in fact an *underestimate* of the brush height, as the applied height is only relevant for Tau coverage up until the point of the mushroom-to-brush transition, beyond which the brush height should increase as Φ_{Tau} increases.

Within the polyelectrolyte brush model the total potential considered ($V_{MT+Tau}{}^{brush}$) consisted of the terms in Eq. (4) (with $V_{cyl}{}^{hard\ MT}(H)$ incorporating σ= -0.387+0.253*Φ_{Tau} (e nm^{-2}) to account for the added charge from Tau minus the charge of the PD as described above in the previous section) plus the interaction potential between cylindrical MTs coated with Tau's PD in the brush state ($V_{cyl}{}^{brush,Tau-PD}(H)$). Following Pincus and Witten the interaction potential between polyelectrolyte brushes in a (1:1) salt solution with concentration c_s may be written as[65,66] (see SI Note S2.3):

$$V_{cyl}{}^{brush,Tau-PD}\,(H)/k_BT = \frac{2\pi\sqrt{R_{MT}}\,f_{tauPD}^2 N_{tauPD}^2}{c_s\left(d_g^{tau}\right)^4}\left(\frac{1}{\sqrt{H}}-\frac{1}{\sqrt{2L_{TauPD}}}\right) \qquad \text{(Eq. 3.6)}$$

In this equation, the counterion distribution is predominantly determined by the local counterions needed to neutralize the polyelectrolyte-grafted surface.

The repulsive potential between opposing grafted-polyelectrolyte surfaces results from both the counterion pressure and contributions from chain configurational entropy.

Figure 3.5 (c,d) show plots of V_{MT+Tau}^{brush}/k_BT versus H for 3RM and 3RL isoforms with increasing wt% 20k PEO (0.46, 0.93, 1.63, 2.44 wt% for $\Phi_{Tau} = 1/13$ and 0.46, 0.93, 1.63, 2.44, 3.26, 4.07 wt% for $\Phi_{Tau} = 1/10$). The colored potential curves correspond to PEO concentrations where bundling is observed in experiments as shown in Fig. 3.3. Compared to the soft-cylinder model we see that the longer Tau PDs modeled as grafted charged brushes now provide a significant increased repulsion at the higher Tau coverages (Fig. 3.5 (c,d) compared to (a,b) where the potential curves develop minima at significantly higher PEO concentrations).

Overall, the qualitative agreement with similar trends at high Tau coverage between experimentally observed PEO bundling concentrations (Fig. 3.3) and the prediction by the charged brush model (open grey circles in Fig. 3.3 b,c,e,f for PEO concentrations predicting potential depth between 7.5 k_BT for 2 μm MTs) for the -M and -L Tau isoforms is clear. It is also clear that the use of an estimate for the height of the brush is responsible for the lack of quantitative agreement. Thus, the analysis of the data suggest that the longer Tau PDs (-M, -L) undergo a conformational change and are likely in a more extended state at $\Phi_{Tau} = 1/10$, conferring steric stabilization up to osmotic pressures $\approx$ 10,000 to 20,000 Pa, an order of magnitude higher compared to the short Tau isoforms.

3.2.3. Tau induces attraction between MTs at high osmotic pressure

To characterize the P-distance curves in the bundled phase regime we analyzed the SAXS data in the high P regime (30,000 Pa $< P <$ 120,000 Pa) where the system was in the hexagonal (H_{MT}) phase with unbuckled MTs with circular cross-section. At low P in the N_{MT} phase, the SAXS data was fit to the square of the MT form factor $|F_{MT}|^2$, where MTs are modeled as hollow cylinders with inner radius ($<R_{in}^{MT}> \approx 8.0$ nm, a fit parameter) and constant wall thickness w = 4.9 nm, consistent with electron microscopy models of MTs[41] (see e.g. Fig. 3.2 d,e, lowest profiles). As shown previously[5,67], the MT wall-to-wall spacing ($D_{w-w} = a_H - 2*(<R_{in}> + w)$) in the H_{MT} can be quantitatively determined by measuring the X-ray structure factor (giving the hexagonal lattice parameter a_H) and simultaneously the MT form factor yielding $<R_{in}>$ and w. The structure factor was taken to be the sum of Bragg diffraction peaks at the reciprocal lattice vectors $|\mathbf{G_{hk}}| = G_{10}(h^2+k^2+hk)^{1/2}$, $G_{10} = 4\pi/(3^{1/2}a_H)$. Each peak was represented as a squared lorentzian: $[A_{hk}/(W_q^2 + (q_\perp - G_{hk})^2)]^2$, with G_{hk}, amplitudes A_{hk} and a single peak width proportional to W_q (where $1/W_q \approx$ bundle size in cross-section), as fitting parameters. The background subtracted SAXS data for unoriented MT bundles was fit to the MT bundle structure factor multiplied by $|F_{MT}|^2$ and averaged over all orientations in q-space (solid lines in Fig. 3.2d,e top profiles).
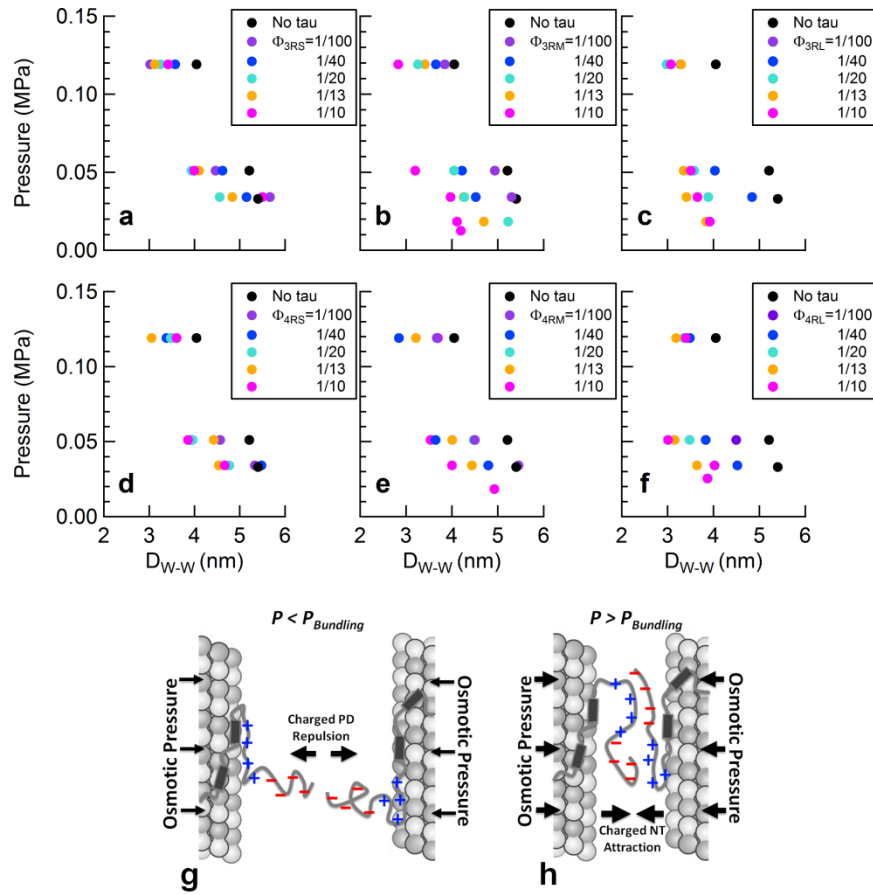
Fig. 3.6| At high osmotic pressures Tau mediates short range attractions between microtubules in the bundled phase. (a-f) The wall-to-wall distance between microtubules in hexagonally-packed bundles plotted as a function of increasing osmotic pressure. Increasing concentrations of (a) 3RS, (b) 3RM, (c) 3RL, (d) 4RS (e) 4RM, and (f) 4RL isoforms decrease the wall-to-wall distance between MTs, indicative of the onset of Tau-induced short range attractions (black circles correspond to distances between bare MTs). (g, h) Schematic cartoons show differing MT-MT interactions mediated by Tau. (g) The repulsion of the anionic component of Tau projection domains at long distances where low-osmotic pressures do not favor chain inter-penetration. (h) The favorable cationic/anionic interaction between overlapping Tau projection domains (possibly including sections of the proline rich region) at short distances where high osmotic pressure favor chain inter-penetration.

Most interestingly, SAXS analysis showed that for a majority of given osmotic pressures, not only did the addition of Tau serve to decrease the lattice

parameter relative to "naked" MTs (Fig. 3.6a-f, filled black circles), but increases

in concentration of Tau further decreased the lattice parameter (Fig. 3.6a-f filled

colored circles). While the decrease due to Tau concentration was apparent in

Tau isoforms with the short projection domain ($\Delta D_{w-w} \approx 0.7$ nm, Fig. 3.6a, d), the

effect was noticeably more pronounced for Tau isoforms with the long projection

domain ($\Delta D_{w-w} \approx 1.5$ nm, Fig. 3.6c, f). The data are consistent with the onset of

Tau-induced short-range attractions arising from the polyampholytic nature of

Tau (i.e. with negative and positive amino-acid residues) and, in particular, the

dipolar nature of the N-terminal tail of all six isoforms (the PD and overall

cationic proline-rich-region, Fig. 3.1b). With increasing osmotic pressures

overcoming longer-ranged repulsions of the overall anionic Tau-PD (Fig. 3.6g,

discussed in the previous section), Tau's N-terminal tails on neighboring MTs

are expected to interpenetrate leading to the formation of favorable short-range

anionic/cationic electrostatic bonds between overlapping chains and effectively

reducing the MT wall to wall spacing (Fig. 3.6h). Similar chain interpenetration

behavior has been reported for protruding neurofilament sidearms, which are

also unstructured polyampholytes, at high osmotic pressures[68–70].

To confirm that the attractive regime was mediated by Tau we conducted

reversibility experiments. When bare MTs were osmotically pressured into the

rectangular-buckled phase at 4,100 Pa (Fig. 3.7a, top profile at 1.63 wt% PEO),

lowering of PEO to below the bundling concentration resulted in a reversible

transition back to the unbundled N_{MT}, consistent with the repulsive nature of

MTs (Fig. 3.7a, lower profile at 0.09 wt% PEO). However, bundling of Tau covered MTs (Φ_{3RS}=1/10) into the R^B_{MT} at the same osmotic pressure (Fig. 3.7b, top profile at 1.63 wt% PEO) followed by a similar dilution did not lead to the unbundled N_{MT} but rather remained in a bundled phase for up to 60 hours after dilution (Fig. 3.7b, lower profile at 0.09 wt% PEO), indicative of stable Tau-induced short range attraction. Interestingly, the MT bundles did not retain the original rectangular symmetry of the R^B_{MT} but rather transitioned to the hexagonal bundled state, H_{MT}. This was to be expected because removal of most of the PEO effectively removed the pressure difference between the outside wall of the MT and the inside luminal wall causing MTs to unbuckle and revert back to their circular cross-section.
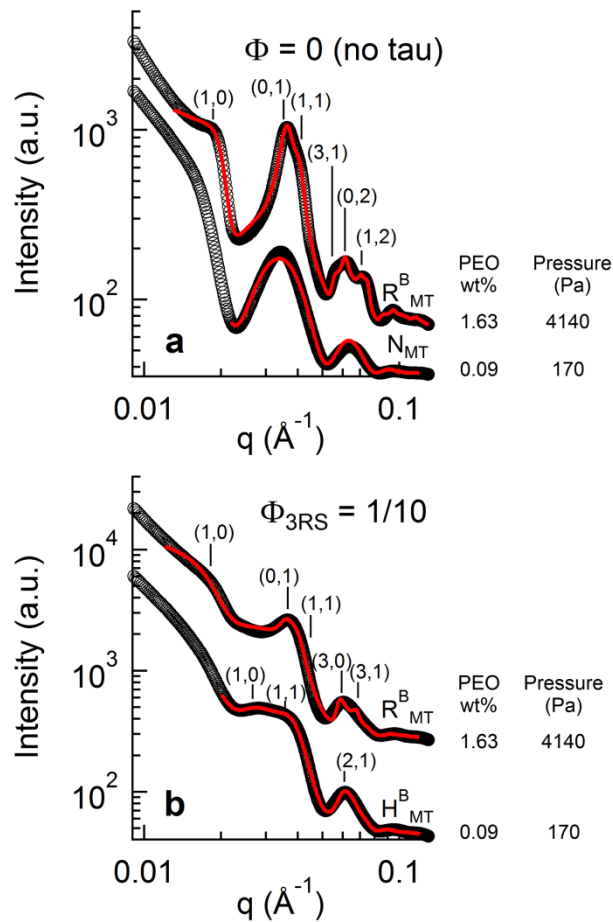
Fig. 3.7 | MAP Tau-induced irreversible MT bundling. (a, b) Reversibility experiments confirm the short range attractions are due to Tau. With no Tau (a), SAXS data analysis shows an osmotic pressure-induced (1.63 wt% 20k PEO) R^B_{MT}, (a, top, a_R=17.3 nm and b_R=30.9 nm) relaxes into a N_{MT} by diluting PEO to 0.09wt% (a, bottom). In the presence of Tau (b, Φ_{3RS}=1/10), a similar dilution from 1.63wt% to 0.09wt% of 20k PEO shows that the bundled state remains (demonstrating the presence of Tau-induced short range attractions), but the bundled phase now transitions from the buckled R^B_{MT} phase (b, top, a_R=17.5 nm and b_R=32.7 nm) to the unbuckled H_{MT} phase (b, bottom, a_H=32.2 nm) due to the large dilution of PEO as described in the text. SAXS data was analyzed and presented fit parameters extracted with fitted model scattering curves (red lines) corresponding to the model appropriate structure and form factor, as described in text.

3.3. Conclusions

We have investigated Tau-mediated forces between MTs over a range of Tau/tubulin-dimer molar ratios (Φ_{Tau}=1/100 to 1/10, which includes the physiological regime) using small-angle-X-ray-scattering on mixtures subjected to osmotic pressure. The current study has revealed that MAP Tau fundamentally alters the repulsive forces between MTs in an isoform-dependent manner. In particular, the jump in osmotic pressure required to bundle microtubules coated with -M and -L Tau isoforms at the higher physiological coverages reveals a gain of function of Tau isoforms with longer N-terminal tails (NTTs, due to the longer projection domains), in imparting steric stabilization to individual microtubules against bundling. Significantly, the Φ_{Tau} at which the jump occurs shows the conformation of the NTT of tau bound to the MT surface at low coverages (before the mushroom-to-brush transition) is substantially more extended ($\approx$a factor of two) than would be expected from SAXS measurements of the radius of gyration of Tau's NTT in solution[48].

What is highly significant in the current work is the demonstration of the functional property of the projection domain, in sterically stabilizing MTs upon undergoing a transition to a charged brush state, from a direct force measurement. Previous identification of Tau's projection domain was based entirely on its lack of binding affinity to MTs and did not give insight to its biophysical functions[24]. Steric stabilization against cellular bio-macromolecules is essential in preventing microtubule loss of function in the crowded axon

environment. Furthermore, the conformation of Tau on the MT surface is intrinsically connected to its coverage. The discovery of two distinct conformation states of MT-bound Tau, namely mushroom or brush, further emphasizes the need for future biophysical measurements of MT bound Tau to be conducted in both regimes.

It is interesting to note that the expression of the six different Tau isoforms is developmentally regulated where fetal brain expresses only the shortest isoform (3RS) while the adult brain (with Tau concentration increasing along the length of the axon away from the cell body) expresses an approximately 1:1 ratio of 3R and 4R Tau[71]. This would suggest that the 3RS isoform is likely to be expressed at a higher level in fetal brain (i.e. compared to the adult brain), enabling steric stabilization of fetal MTs at higher coverage where 3RS Tau would be in a more extended brush conformation. With respect to the adult brain, although the composition of different isoforms is not known at different points along the length of the axon (where the ratio of -S, -M, and -L N-terminal configurations in adult brain, averaged over the entire exon, is 4:5:1, respectively[72]), our finding points to a minimum coverage needed by the longer isoforms (either –M or -L) in order to impart steric stabilization to MTs.

This minimum coverage required for MT steric stabilization by Tau could also shed light on a possible pathway for neurodegeneration. In the diseased state, Tau is often found to be hyperphosphorylated with a weaker binding affinity to MTs. Should MTs lose sufficient Tau coverage to the degree where

projection domains transition from brush to mushroom and fail to sterically stabilize MTs, intracellular trafficking on MTs could be significantly hampered by the non-physiological close-bundled state in the crowded axonal environment.

At high pressures in the MT bundled phase regime, the polyampholytic nature of Tau resulted in a coverage-dependent electrostatic attraction between microtubules. This regime of "tight-bundles", resisted by longer projection domains, may conceivably be accessed in vivo in the presence of excess molecular crowding forces. This would have negative consequences for organelle trafficking by MTs where the small MT wall-to-wall spacings, ranging between 3 and 5 nm, would be expected to interfere with motors carrying cargo[73].

In addition to the biological interest in MAP Tau as a key component of the axonal cytoskeleton, the directed assembly of MTs by intrinsically disorder protein Tau is also of broad interest from a biomolecular materials and biophysics perspective. This is because the unique manifestation of short-range attraction and long-range repulsion by Tau of microtubules gives inspiration for the design of biomaterials with multiple interaction motifs.

3.4. Methods

3.4.1. Tubulin purification

Tubulin was purified, as described[74,75]. Briefly, MAP-rich tubulin was isolated from bovine brain via successive *in vitro* polymerization/depolymerization cycles.

66

After suspension in PEM50 (50 mM PIPES pH 6.85, 1 mM $MgCl_2$, 1mM EGTA) and 0.1 mM GTP, tubulin was purified by running through a P-11 phosphocellulose column (GE Healthcare, Madison, Wisconsin), with non-tubulin elements binding to the column. Tubulin (>99% purity) was drop frozen with liquid nitrogen and stored at -70°C, with protein concentration determined by Bradford assay.

3.4.2. Tau purification

Tau was expressed and purified, as described[11,76]. Briefly, the human cDNA for all six Tau isoforms were encoded in pRK expression vectors and expressed via BL21(DE3) cells. Bacteria was collected and lysed through sonication and boiling. After isolation via centrifugation, the soluble Tau was bound to a P-11 phosphocellulose column and eluted by increasing NaCl concentrations. SDS-PAGE was used to identify fractions where Tau was collected and fractions were run and bound through a HiTrap phenyl HP (GE Healthcare) column, whereby Tau was again eluted by decreasing $(NH_4)_2SO_4$ concentrations. Fractions with Tau were identified as before and suspended in BRB80 (80 mM PIPES at pH 6.8, 1 mM $MgSO_4$, 1 mM EGTA) and 0.1% β-mercaptoethanol. Concentration was determined by SDS-PAGE comparison to Tau standard, with original concentration determined by amino acid analysis.

3.4.3. Sample preparation

Microtubules were polymerized from 45 μM (5 mg/mL) of tubulin, 1 mM GTP, 5 wt% glycerol mixed in PEM50 buffer (50mM PIPES, 1mM EGTA, 1 mM $MgCl_2$ at pH 6.8) at 35° C for 20 minutes, after which 40 μM taxol, dissolved in DMSO, was added (matching the subsequent final tubulin concentration) to stabilize microtubules. Tau was then added to pre-assembled MTs to desired Φ_{Tau} with a small amount of 1M KCl in buffer to bring the solution to a final concentration of 25 mM KCl. Varying concentration of 20,000 MW poly(ethylene oxide), or 20k PEO, dissolved in buffer was then added, with osmotic pressure induced calculated as a function of 20k PEO concentration: log(P)=1.57 +2.75 x [PEO wt%].[21], where P is the pressure in dynes cm^{-2} and PEO wt% is the weight percentage of 20k PEO[37].

3.4.4. Differential interference contrast microscopy

A CCD camera (SensiCam[QE], Cooke) mounted on a Diaphot 300 (Nikon) with Xenon lamp (Sutter Instrument, Novato, CA) was used for optical microscopy measurements with samples placed between two microscopic slides sealed by wax.

3.4.5. Small-angle X-ray scattering

SAXS was carried out at the Stanford Synchrotron Radiation Laboratory (Palo Alto, CA) beamline 4-2 at 9 KeV with a Si(111) monochromator. Scattering data was taken with a 2D area detector (MarUSA, Evanston, Illinois) with a sample to detector distance of ≈3.5 meters. Prepared samples were spun down at 16,000 x g for 30 minutes and loaded into 1.5 mm diameter quartz capillaries (Hilgenberg GmbH, Malsfeld, Germany) at 3.5K RPM. Data analysis incorporated structure and form factors (as described in text) fit with non-linear least-squared fitting routines, with background subtraction of SAXS data tha

3.5. Detailed calculations of inter-microtubule potential energies

3.5.1. Electrostatic potential energy between two hard, charged cylinders

To first order, the electrostatic repulsive forces between MTs can be modeled as the potential energy between two parallel, charged cylinders. This is calculated by applying the Derjaguin approximation[77] (which has its limits, but is used for simplicity) to relate the potential energy between planar surfaces to curved surfaces of radius R:

$$V_{cyl}(H) = \sqrt{R} \int_{H}^{\infty} V_{plane}(h) \frac{dh}{\sqrt{h-H}} \tag{Eq. 3.7}$$

Where $V_{plane}(h)$ (energy per unit area) and $V_{cyl}(H)$ (energy per unit length) are the potential energies for surface-to-surface distances for parallel planes and cylinders, respectively (Fig. 3.8).
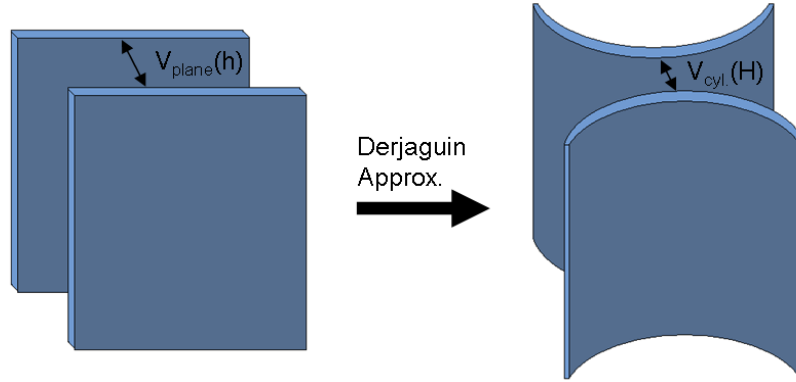
Fig. 3.8| The Derjaguin approximation takes planar potential energies and converts them to equivalent potential energies for curved surfaces. In our particular case, the electrostatic planar potential for surface-to-surface distance h is "bent" to an equivalent potential for two parallel cylindrical surfaces with surface-to-surface distance H

The potential energy per unit area between two charged surfaces (in the Debye-Hückel regime) with "hard" surface charge density σ in an electrolyte solution (of permittivity $\varepsilon_r \varepsilon_0$) is[78]

$$V_{plane}^{hard}(h) = \frac{2\sigma^2 e^{-\kappa h}}{\kappa \varepsilon_r \varepsilon_0} \qquad \text{(Eq. 3.8)}$$

Where κ is the inverse of the Debye-Hückel length, the characteristic decay length of electrostatic potential energy in an electrolyte solution of concentration c_s. For monovalent salt concentration c_s, the Debye-Hückel length is calculated[78]

as $\lambda_D = 1/\kappa = \left[\varepsilon_r \varepsilon_0 k_B T / (2e^2 c_s)\right]^{1/2}$. Inserting Equation 3.8 into Equation 3.7 yields the cylindrical potential energy per unit length for surface-to-surface distance H, as calculated by Ohshima and Hyono[56]:

$$V_{cyl}^{hard}(H) = \frac{2\sqrt{\pi R}\sigma^2}{\varepsilon_r \varepsilon_0 \kappa^{3/2}} Li_{1/2}(e^{-\kappa H}) \qquad \text{(Eq. 3.9)}$$

Where $Li_{1/2}(z) = \sum_{k=1}^{\infty} z^k / k^{1/2}$, the polylogarithm function of order 1/2. The reduced potential energy per unit length rewritten for our system in terms of cylinder radius (microtubule radius, $R_{MT} \approx 12.5$nm), Debye-Hückel length $\lambda_D = .85$nm for PEM50 (50 mM PIPES, 1mM MgCl$_2$ and 1 mM EGTA at pH 6.8 with 75 mM NaOH) with 25 mM KCl added (equivalent to a 100 mM solution of 1:1 electrolyte plus 1 mM of MgCl$_2$), surface charge density σ_{MT}, and salt concentration $c_s \approx .075$nm^{-3} (for a monovalent salt equivalent to PEM50 at pH 6.8 with 25 mM added KCl):

$$\frac{V_{cyl}^{hardMT}(H)}{k_B T} = \frac{\sqrt{\pi R_{MT}}\sigma_{MT}^2 \kappa^{1/2}}{e^2 c_s} Li_{1/2}(e^{-\kappa H}) \qquad \text{(Eq. 3.10)}$$

The surface charge density σ, absent a physical measurement, is usually calculated from the net charge of the sequence without accounting for partial neutralization by counterions. Measurements of microtubule electrophoretic movement in microchannels provide an estimate of the partial counterion neutralization [54]. At pH 6.9, the bare-charge of the tubulin (Q_{bare}) and bound

71

nucleotides/ions was calculated to be -50e per dimer, but the effective charge (Q_{eff}) was measured as -23e per dimer. Thus, we calculate the effective charge renormalization prefactor $r = Q_{\text{eff}}/Q_{\text{bare}} = 0.46$.

In our experiments the bare charge of α-tubulin (NCBI protein database: NP_001159977.1) and ß-tubulin (NP_001040014.1) with bound nucleotides/ions was calculated to be -21.7e and -22.6e, respectively, at pH 6.8 (via http://protcalc.sourceforge.net/), giving a sum bare-charge of -44.3e per tubulin-dimer. As both experiments were in similar buffer conditions, we use the effective charge renormalization prefactor r to calculate the effective charge Q_{eff} = $r\, Q_{\text{bare}} \approx$ -20.4e per tubulin-dimer. As the dimer area $\approx$ 41 nm^2 (product of dimer height, 8 nm, and protofilament-protofilament distance, 5.13 nm)[79], this gives an effective renormalized suface charge density $\sigma_{\text{MT}} =$ -0.497e nm^{-2}.

3.5.2. MT bundling using the hard cylinder model

Equation S2.6 and 3.10 are used to model the pairwise interaction of microtubules using depletion attraction and the hard cylinder model for microtubules.

$$V_{MT}(H) \;=\; V_{depletion}(H) \;+\; V_{cyl}^{hardMT}(H) \tag{Eq. 3.11}$$

The sum of the potential energies (Eq. 3.11) is plotted as a function of wt% of 20k PEO (Fig. 3.9). If we consider the average length of microtubules (~2 μm, Fig.

3.10) and expect the bundled state to correspond to a potential energy depth of 5 to 10 k_BT, the model predicts bundling at a wt% of 20k PEO as low as 0.15. As the nematic (non-bundled) phase is experimentally observed at a higher wt% of 20k PEO (0.25), the model does not capture the magnitude of repulsive forces.
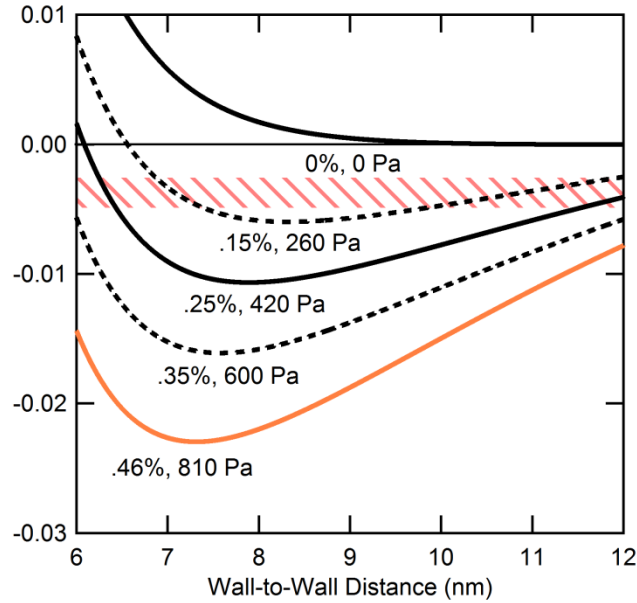
Fig. 3.9| The energy per unit length curves against the wall-to-wall distance using the simple charged-cylinder model for MTs. Curves derived from the model (equation S1.10) are plotted for actual PEO wt% used in experiments (solid lines) and in-between concentrations (dashed lines). Colors (from black to orange) are coordinated with data in fig. 3 (Φ_{Tau}=0). If the bundled state corresponds to a potential energy depth of 5 to 10 k_BT (the pink-striped zone) for 2 µm length MTs (see Fig. 3.10), the model predicts bundling would occur at .15 wt% of 20k PEO (and above) while experimentally bundling is seen between 0.25 and 0.46 wt% of 20k PEO (orange curve).
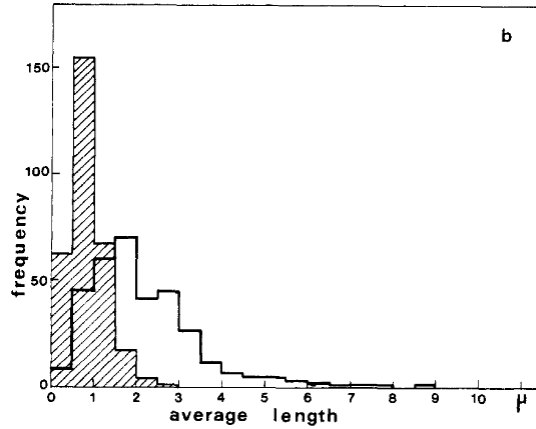
Fig. 3.10| The length distributions for taxol-stabilized microtubules. Near stoichiometric amounts of taxol to tubulin, the average length of microtubules is identified using electron microscopy and plotted after 1 min (hatched bars) and 30 mins (thick bars)[80]. The average length is taken to be 2 μm

3.5.3. Electrostatic potential energy between two soft, charged cylinders

It is apparent that the modeling of microtubules as charged "hard" cylinders underestimates the repulsive component, thus requiring a more advanced model. From our knowledge of tubulin crystallography[79], MTs do not have a constant charge density. Most of the charge is located on the C-terminal tails (CTT) of both α- and β- tubulin (18 and 21 residues, respectively[53], both with an average ionization fraction $f_{CTT}\approx0.5$). As a result of this high-charge density, not only does it make MTs akin to a polyelectrolyte-grafted colloids (Fig. 3.11) but the charge must be renormalized (with prefactor r), as in S1.3 with the MT surface. Due to the intrinsically disordered nature of the CTT, the height of the CTT is not well defined but is estimated to be $L_{CTT}\approx4$ nm from simulation data[57], with an expanded conformation expected by theory[81].

74
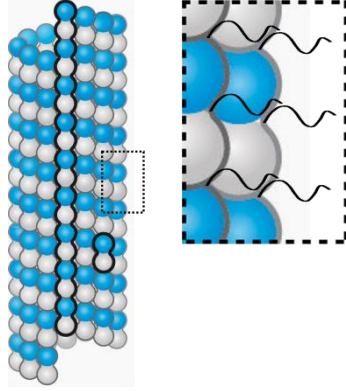
Fig. 3.11 | A close-up view of the microtubule surface reveals positively-charged C-terminal tails of α- and β- tubulin. While microtubules can be approximated to be hollow cylinders made up of tubulin with constant charge density, a more appropriate model takes into account the charge found in the CTTs that project off the microtubule surface.

A more sophisticated model for microtubules accounts for the polyelectrolyte layer above the microtubule surface, necessitating a shift from the hard cylinder model (with surface charge density, σ) to a soft cylinder (with volume charge density, ρ) model. The potential energy per unit area for a soft planar charged surface is[56]

$$V_{plane}^{soft\,CTT}(h) = \frac{\rho^2 \sinh^2(\kappa L)}{2\kappa^3 \varepsilon_r \varepsilon_0}\left[\coth\left(\frac{\kappa h}{2}\right) - 1\right] \qquad \text{(Eq. 3.12)}$$

Where L is the height of the polyelectrolyte layer and h is the surface-to-surface distance, *not* including the polyelectrolyte layer. Utilizing the Derajaguin approximation (Eq. 3.7), the soft cylinder model is calculated by Ohshima[56]:

$$V_{cyl}^{soft\,CTT}(H) = \frac{2\sqrt{\pi R}\,\rho^2}{\varepsilon_r \varepsilon_0 \kappa^{7/2}} \sinh^2(\kappa L) Li_{1/2}(e^{-\kappa H}) \qquad\qquad H \geq 2L \qquad\qquad \text{(Eq. 3.13)}$$

Where the volume charge density is the product of ionization fraction ($f_{CTT} \approx 1/2$), average number of residues in the CTT ($N_{CTT}=19.5$), and renormalization prefactor r, divided by the volume occupied by the CTT (simplified as the product of square of the CTT grafting distance [$(d_g^{CTT})^2 \approx 21$ nm^2] and the height of the CTT [$L_{CTT}=4$ nm]):

$$\rho = \frac{erfN}{d_g^2 L} \qquad\qquad \text{(Eq. 3.14)}$$

Equation 3.13 can be rewritten using the appropriate variables. To include the limit where $H < 2L$, the polyelectrolyte layer height is compressed to half the surface-to-surface distance, by geometry.

$$\frac{V_{cyl}^{soft\,CTT}(H)}{k_B T} = \begin{cases} \dfrac{\sqrt{\pi R_{MT}}\left(\dfrac{erf_{CTT}N_{CTT}}{\left(d_g^{CTT}\right)^2 L_{CTT}}\right)^2}{c_s \kappa^{3/2}} \sinh^2(\kappa L_{CTT}) Li_{1/2}(e^{-\kappa H}) & H \geq 2L_{CTT} \\[3em] \dfrac{\sqrt{\pi R_{MT}}\left(\dfrac{erf_{CTT}N_{CTT}}{\left(d_g^{CTT}\right)^2 H}\right)^2}{c_s \kappa^{3/2}} \sinh^2\left(\dfrac{\kappa H}{2}\right) Li_{1/2}(e^{-\kappa H}) & H < 2L_{CTT} \end{cases} \qquad \text{(Eq. 3.15)}$$
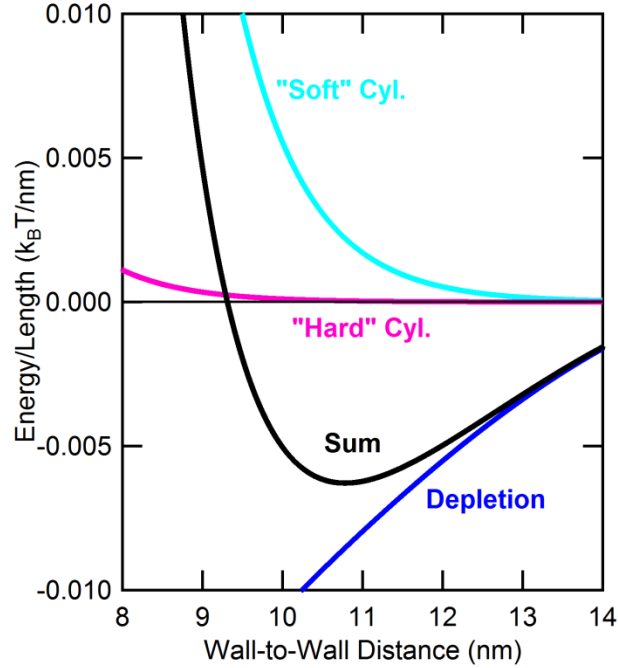
Fig. 3.12| Component breakdown of the potential energy per unit length for 0.46 wt% of 20k PEO. Note the dominant contribution of the soft-cylinder, owing to the short Debye-Hückel length which more effectively screens the hard-cylinder interactions.

3.5.4. MT bundling using the soft cylinder model

In our more advanced model (utilizing equation S1.15), contributing factors include the depletion attraction (from the 20k PEO, equation S1.5), "hard" electrostatic repulsion (from the remaining charge on the MT surface [where $\sigma_{\text{Tub-CTT}}$=-0.387e nm^{-2}], equation S1.9), and soft electrostatic repulsion from the tubulin CTT (equation S1.14)

$$V_{MT}^{Total}(H) \ = \ V_{Depletion}(H) \ + \ V_{cyl}^{hardMT}(H) + \ V_{cyl}^{soft\,CTT}(H) \qquad \text{(Eq. 3.16)}$$

The system potential energies were also plotted over a range of low wt% of 20k PEO (Fig. 3.13). The model captures the correct wt% of 20k PEO.
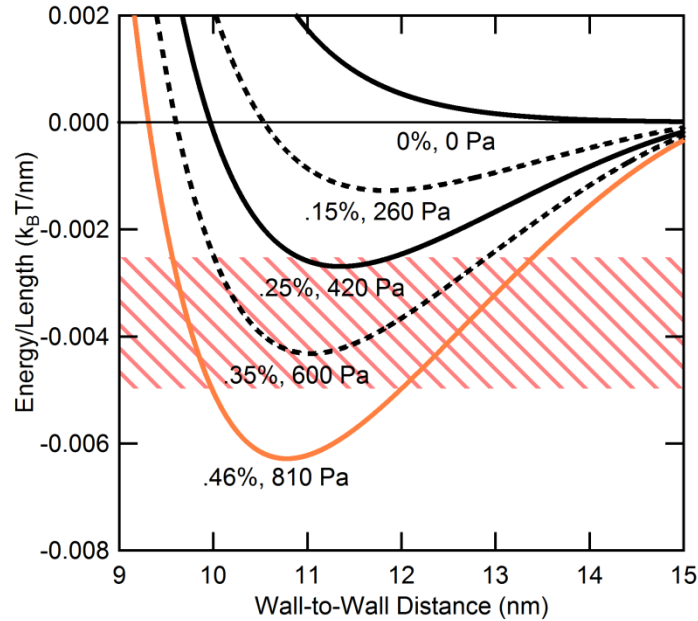
Fig. 3.13| The energy per unit length curves against the wall-to-wall distance utilizing the soft-cylinder model. Curves derived from the model (Eq. 3.16) are plotted for actual PEO wt% used in experiments (solid lines) and in-between concentrations (dashed lines). Colors (from black to orange) are coordinated with data in fig. 3.3 (Φ_{Tau}=0). If the bundled state corresponds to a potential energy depth of 5 to 10 k_BT (the pink-striped zone) for 2 µm length MTs (see Fig. 3.10), the model predicts bundling would occur at .46 and .35 wt% of 20k PEO, which is experimentally recapitulated (orange curve).

3.5.5. Height of Tau protruding normal to the microtubule surface

While treatment of the C-terminal tails of tubulin is relatively straightforward, models of Tau are more involved because of its polyampholytic nature. While it is known the microtubule-binding repeats are closely bound to the surface, less is known about the N- and C- terminal tails of Tau (NTT and

CTT, respectively). Due to the relative size of the Tau NTT (196 residues for the shortest isoform) compared to the Tau CTT (73 residues) and the prior knowledge that the projection domain of the NTT is known to project off the MT surface[24], only the contributions of the Tau NTT is considered.

The NTT consists of a highly-charged polyampholytic projection domain (PD, ~40% of residues charged) and a weakly-cationic proline-rich region (PRR, ~20% of residues charged). Simulations[62,63] suggest that the PRR is weakly-bound to the highly-anionic MT surface and the PD assumes an extended conformation normal to the MT surface. The dramatic increase in pressure required to bundle microtubules for the –M and –L Tau isoforms (see Fig. 3.3, main paper) suggest that Tau underwent a conformational change on the MT surface at $\Phi=1/13$ for the –L isoforms and $\Phi=1/10$ for the –M isoforms. This occurs when the diameter of Tau protein on the MT surface approaches the distance between Tau proteins on MTs.

Even though Tau is physisorbed on the MT surface, binding data[32] indicates that the concentration at which Tau is mixed with tubulin is the same concentration upon which Tau is bound to the MT surface (Up until $\Phi=1/5$ to 1/3). Thus, we treat Tau as essentially grafted to the MT surface, where

$$d_g^{Tau} = \frac{4.5}{2\sqrt{\frac{\Phi_{Tau}}{2}}} \text{ [nm]} \qquad\qquad \text{(Eq. 3.17)}$$

4.5 nm is the average tubulin monomer-monomer distance and the factor of 2 arises because Φ is a dimer ratio. The lowest Φ at which the transition is observed corresponds to a grafting distance of 20.3 nm and 23.1 nm for –M and –L isoforms of Tau, respectively, which will be used as L_{PD}, or the height of the projection domain.

The grafting distance (as a proxy for the polyelectrolyte brush height) is clearly an underestimate, as it is more appropriate for the height of Tau prior to the brush transition. However, it will serve as a useful estimate for our models.

3.5.6. Treatment of Tau isoforms with longer projection domains (3RM, 3RL) on microtubules (soft cylinder model)

The 3RM isoform of Tau is also examined using the same system potential energy as before (Eq. 3.16) with $r = 1$ (i.e. where charge renormalization is expected to be negligible because the combination of a low net ionization of the PD together with low Tau coverage leads to a low charge density polyelectrolyte layer surrounding the microtubule) and additional soft potential term for Tau with appropriate variable substitution ($L_{3RM,PD}$=20.3nm, $N_{3RM,PD}$=121, $f_{3RM,PD}$=.120, and eq. 3.16) (Fig. 3.14).
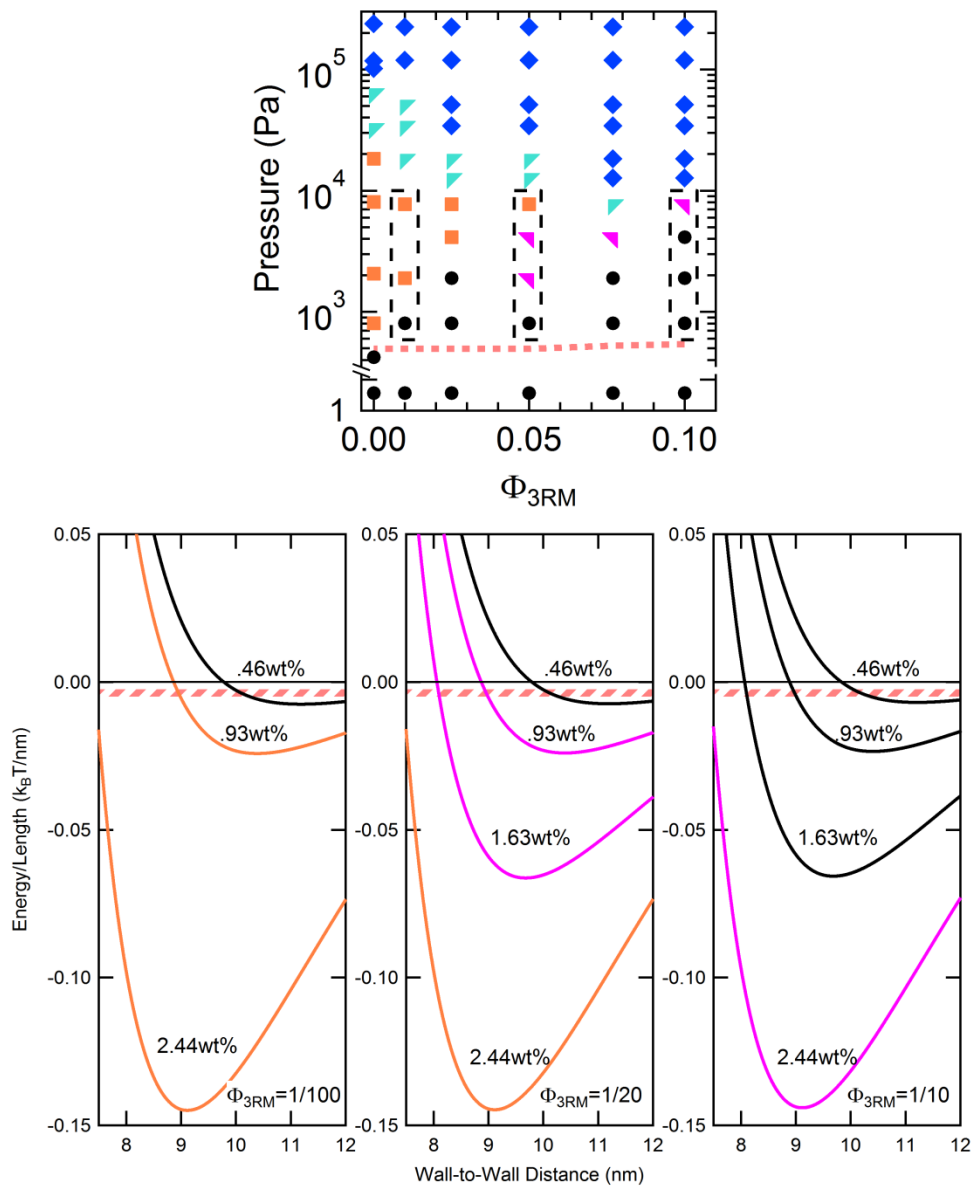
Fig. 3.14| The soft cylinder model did not capture the resultant increase in repulsion between microtubules coated with 3RM Tau. At osmotic pressures taken from selected experimental data points (top, dashed box), the normalized potential energy per unit length curves were plotted for Φ_{3RM}=1/100, 1/20, 1/10 (bottom), with the color of each model curve corresponding to phase observed experimentally. The phase diagram (top) has been marked (pink-dashed line) at the pressure where bundling is expected, if bundling is assumed to occur at a potential energy depth of 7.5 k_BT for 2 μm length MTs (see Fig. 3.10). The potential energy curves (bottom) also have a pink-striped zone, which corresponds to a potential energy depth of 5 to 10 k_BT.

The soft cylinder model for the 3RM isoform of Tau does not capture the increase in repulsion, especially at $\Phi_{3RM}=1/10$, where phases that were experimentally observed to be in non-bundled phases were, by our model, expected to be bundled. The model is similarly applied to the 3RL isoform of Tau, with appropriate substitution of variables ($N_{3RL,PD}=150$, $f_{3RL,PD}=.120$, $L_{3RL,PD}=23.1$ nm) (Fig. 3.15).
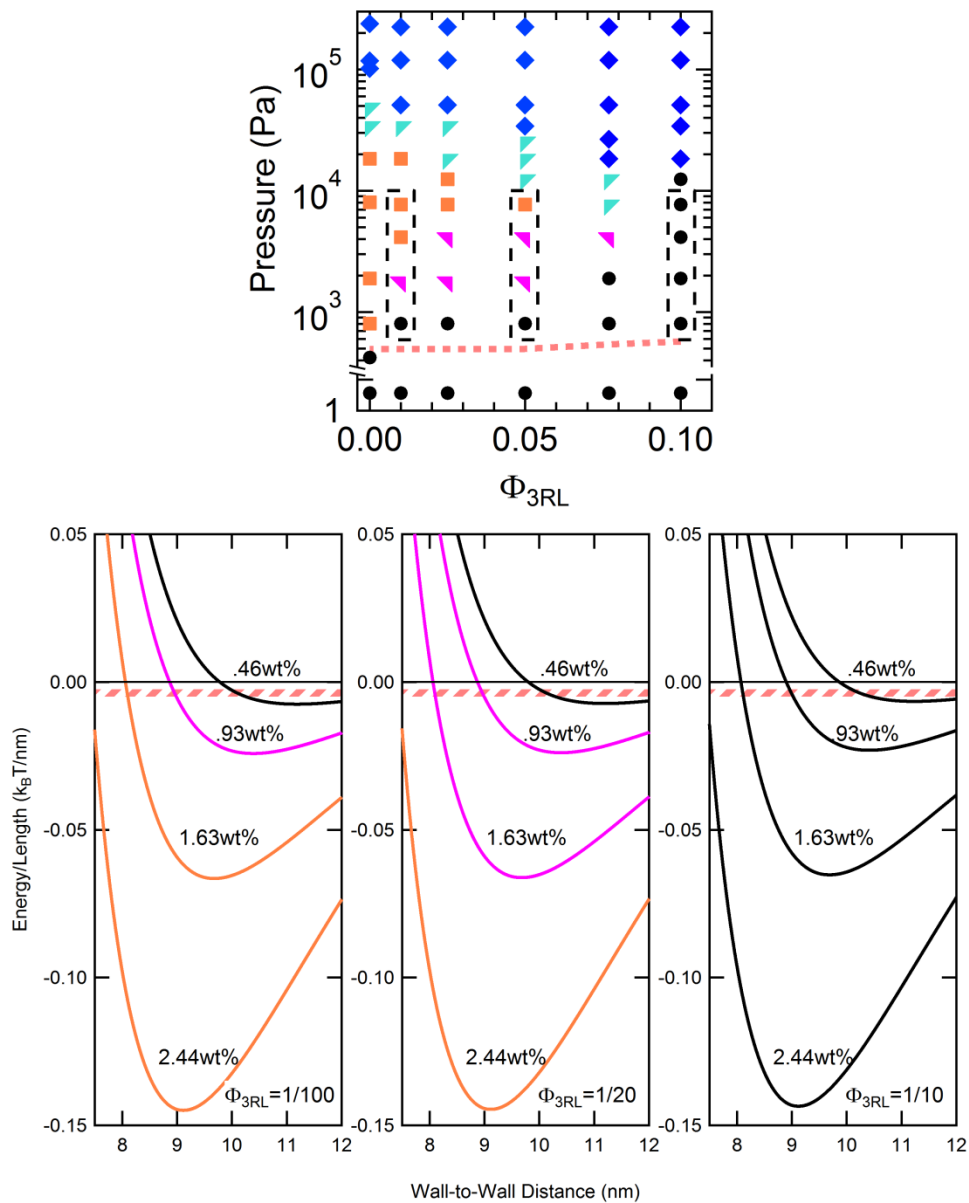
Fig. 3.15| The soft cylinder model did not capture the resultant increase in repulsion between microtubules coated with 3RL Tau. At osmotic pressures taken from selected experimental data points (dashed boxes, top), the normalized potential energy per unit length curves were plotted for Φ_{3RL}=1/100, 1/20, 1/10 (bottom), with the color of each model curve corresponding to phase observed experimentally. The phase diagram (top) has been marked (pink-dashed line) at the pressure where bundling is expected, if bundling is assumed to occur at a potential energy depth of 7.5 k_BT for 2 μm length MTs (see Fig. 3.10). The potential energy curves (bottom) also have a pink-striped zone, which corresponds to a potential energy depth of 5 to 10 k_BT.

83

Upon accounting for the Tau isoforms with the longer projection domains, there was not an appreciable increase in repulsion in the modeled MT-MT interactions. The soft cylinder model broke down for Tau and another model was required to recapitulate the increase in bundling pressure required to bundle MTs with higher coverage of the Tau isoforms with longer projection domains.

3.5.7. Treatment of Tau isoforms with longer projection domains (3RM, 3RL) on microtubules (charged brush model)

The soft cylinder model for Tau is insufficient. Instead, we treat the PD as a brush (with appropriate modifications). While the theory was developed for polyelectrolytes (and not polyampholytes), a polyelectrolyte brush model is used to examine the scaling of the disjoining pressure.

At high grafting density, interactions between polyelectrolytes on the same surface dominate and cause polyelectrolytes to stretch into a brush-like conformation (surface charge effects polyelectrolyte conformation, but the following model is chosen for its simplicity). Previously, Witten and Pincus[65] theorized that for a given polyelectrolyte solution (of counterion concentration c_0), the osmotic pressure in the presence of salt (c_s) is given by

$$P \cong c_0 k_B T \left(\frac{\kappa_0^2}{\kappa_0^2 + \kappa_s^2} \right)$$ (Eq. 3.18)

Where $\kappa_0^2 = 4\pi l_B c_0$ and $\kappa_s^2 = 4\pi l_B (2c_s)$ is the inverse square of the Debye-length of counterions and added monovalent salt, respectively. In the limit of high salt ($\kappa_s^2 \gg \kappa_0^2$) the pressure can be solved[66] as a function of as a concentration of monomers $(c_m = N_m (Ld^2)^{-1})$, where N_m is the degree of polymerization and Ld^2 is the space in which the polymers occupy) and net ionization fraction f

$$P \cong c_0 k_B T \left(\frac{\kappa_0^2}{\kappa_s^2} \right) = \frac{k_B T c_0^2}{2c_s} = \frac{k_B T (f c_m)^2}{2c_s} \qquad \text{(Eq. 3.19)}$$

The disjoining pressure, Π_{Plane}, as a function of the surface-to-surface distance h is then

$$\Pi_{plane}^{brush} = \frac{k_B T}{2c_s} \left(\frac{2fN}{d_g^2 h} \right)^2 \qquad h \leq 2L \qquad \text{(Eq. 3.20)}$$

The Derjaguin approximation is used as before (but instead, for force) to arrive at the equivalent disjoining pressure for two cylinders[18]

$$\Pi_{cyl}^{brush}(H) = \sqrt{R} \int_H^\infty \Pi_{Plane}^{Brush}(h) \frac{dh}{\sqrt{h-H}} = -\frac{\pi \sqrt{R} k_B T f^2 N^2}{c_s d_g^4} \left(\frac{1}{H^{3/2}} \right) \qquad \text{(Eq. 3.21)}$$

Equation 3.21 can be integrated to obtain the disjoining potential energy for the appropriate limits

$$V_{cyl}^{brush}(H) = -\int_H^{2L} \Pi_{cyl}^{Brush}(H')dH' = \frac{2\pi \sqrt{R} k_B T f^2 N^2}{c_s d_g^4} \left(\frac{1}{\sqrt{H}} - \frac{1}{\sqrt{2L}} \right) \qquad \text{(Eq. 3.22)}$$

This gives the reduced potential energy, with appropriate insertion of variables:

85

$$\frac{V_{cyl}^{brush,tauPD}(H)}{k_B T} = \begin{cases} \dfrac{2\pi\sqrt{R_{MT}}\, f_{TauPD}^2 N_{TauPD}^2}{c_s \left(d_g^{Tau}\right)^4}\left(\dfrac{1}{\sqrt{H}} - \dfrac{1}{\sqrt{2L_{TauPD}}}\right) & H < 2L_{TauPD} \\[2ex] 0 & H \geq 2L_{TauPD} \end{cases} \quad \text{(Eq. 3.23)}$$

The system potential energy is modeled, as before, but the contribution from Tau utilizing the soft cylinder model (4th term) is replaced with a contribution from Tau utilizing the polyelectrolyte brush model (Eq. 3.23) and the 2nd term is taken to include remaining anionic surface charge of the MT surface (without the tubulin CTT) and the positive contribution from the bound Tau (which excludes the PD, $\sigma_{MT\text{-}CTT,3RTau\text{-}NT}$=-(-0.387+0.253×$\Phi_{Tau}$) e nm^{-2})

$$V_{MT+Tau}^{Brush} = V_{Depletion} + V_{cyl}^{hardMT,tau} + V_{cyl}^{soft,CTT} + V_{cyl}^{brush,tauPD} \quad \text{(Eq. 3.24)}$$

Applying the charged brush model to the isoforms with the longer projection domains of Tau did recapitulate a jump in 20k PEO required to bundle the microtubules, especially at higher Tau coverages (Fig. 3.16 and 3.17). The brush model seemed to be a more appropriate (despite assumptions made!) for high coverages of the Tau isoforms with longer projection domains (3RM, 4RM, 3RL, 4RL).
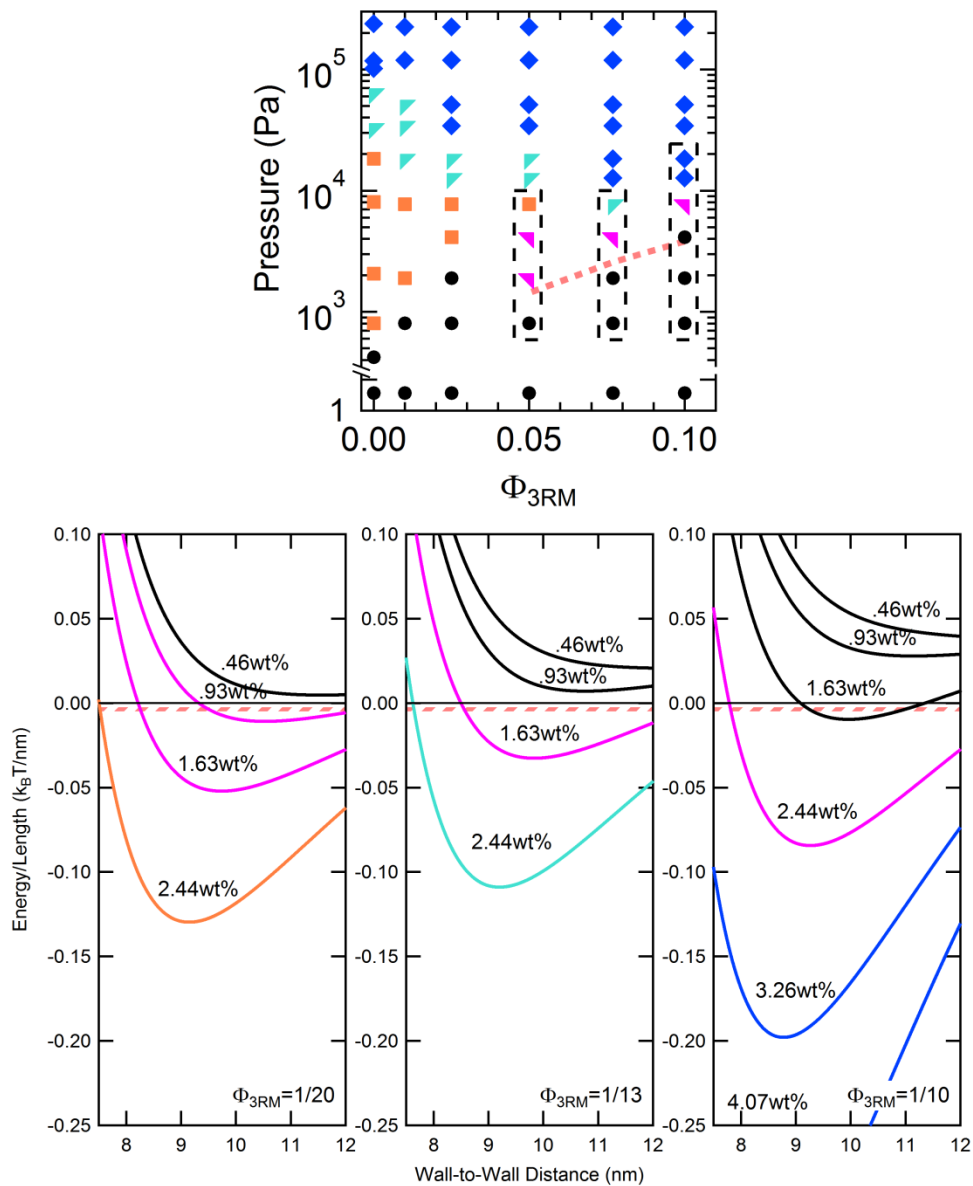
Fig. 3.16| The charged brush model for 3RM Tau at higher coverages of Tau is in closer agreement with experimental behavior. At osmotic pressures taken from selected experimental data points (top), the normalized potential energy per unit length curves were plotted for Φ_{3RM}=1/20, 1/13, 1/10 (bottom), with the color of each model curve corresponding to phase observed experimentally. The phase diagram (top) has been marked (pink-dashed line) at the pressure where bundling is expected, if bundling is assumed to occur at a potential energy depth of 7.5 k_BT for 2 μm length MTs (see Fig. 3.10). The potential energy curves (bottom) also have a pink-striped zone, which corresponds to a potential energy depth of 5 to 10 k_BT.

Fig. 3.17| The charged brush model for 3RL Tau at higher coverages of Tau is in closer agreement with experimental behavior. At osmotic pressures taken from selected experimental data points (top), the normalized potential energy per unit length curves were plotted for Φ_{3RL}=1/20, 1/13, 1/10 (bottom), with the color of each model curve corresponding to phase observed experimentally. The phase diagram (top) has been marked (pink-dashed line) at the pressure where bundling is expected, if bundling is assumed to occur at a potential energy depth of 7.5 k_BT for 2 μm length MTs (see Fig. 3.10). The potential energy curves (bottom) also have a pink-striped zone, which corresponds to a potential energy depth of 5 to 10 k_BT.

3.6.   References

1.   Biology, C. *Cell Biology*. (Saunders/Elsevier, 2008).

2.   Desai, A. & Mitchison, T. J. Microtubule polymerization dynamics. *Annu. Rev. Cell Dev. Biol.* **13,** 83–117 (1997).

3.   Amos, L. A. & Baker, T. S. The three-dimensional structure of tubulin protofilaments. *Nature* **279,** 607–612 (1979).

4.   Löwe, J., Li, H., Downing, K. H. & Nogales, E. Refined structure of alpha beta-tubulin at 3.5 A resolution. *J. Mol. Biol.* **313,** 1045–1057 (2001).

5.   Ojeda-Lopez, M. A. *et al.* Transformation of taxol-stabilized microtubules into inverted tubulin tubules triggered by a tubulin conformation switch. *Nat. Mater.* **13,** 195–203 (2014).

6.   Amos, L. A. & Schlieper, D. Microtubules and maps. *Adv. Protein Chem.* **71,** 257–298 (2005).

7.   Binder, L. I., Frankfurter, A. & Rebhun, L. I. The distribution of tau in the mammalian central nervous system. *J. Cell Biol.* **101,** 1371–1378 (1985).

8.   Morris, M., Maeda, S., Vossel, K. & Mucke, L. The Many Faces of Tau. *Neuron* **70,** 410–426 (2011).

9.   Drechsel, D. N., Hyman, A. A., Cobb, M. H. & Kirschner, M. W. Modulation of the dynamic instability of tubulin assembly by the microtubule-associated protein tau. *Mol. Biol. Cell* **3,** 1141–1154 (1992).

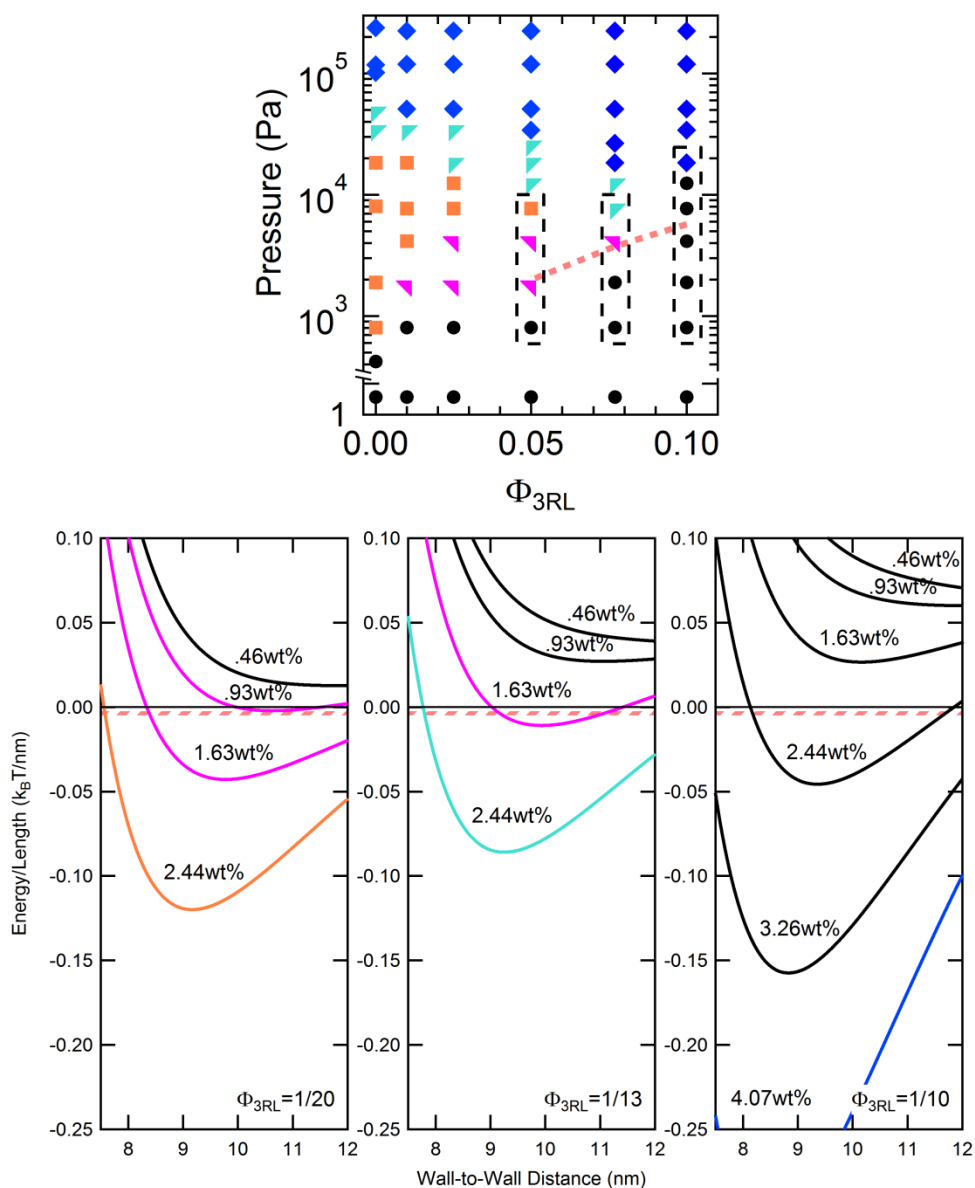10.   Gustke, N., Trinczek, B., Biernat, J., Mandelkow, E. M. & Mandelkow, E. Domains of tau protein and interactions with microtubules. *Biochemistry* **33,** 9511–9522 (1994).

11.   Panda, D., Samuel, J. C., Massie, M., Feinstein, S. C. & Wilson, L. Differential regulation of microtubule dynamics by three- and four-repeat tau: implications for the onset of neurodegenerative disease. *Proc. Natl. Acad. Sci. U. S. A.* **100,** 9548–9553 (2003).

12.   Weingarten, M. D., Lockwood, A. H., Hwo, S. Y. & Kirschner, M. W. A protein factor essential for microtubule assembly. *Proc. Natl. Acad. Sci. U. S. A.* **72,** 1858–1862 (1975).

13.   Witman, G. B., Cleveland, D. W., Weingarten, M. D. & Kirschner, M. W. Tubulin requires tau for growth onto microtubule initiating sites. *Proc. Natl. Acad. Sci. U. S. A.* **73,** 4070–4074 (1976).

14.   Drubin, D. G., Feinstein, S. C., Shooter, E. M. & Kirschner, M. W. Nerve

growth factor-induced neurite outgrowth in PC12 cells involves the coordinate induction of microtubule assembly and assembly-promoting factors. *J. Cell Biol.* **101,** 1799–1807 (1985).

15.   Esmaeli-Azad, B., McCarty, J. H. & Feinstein, S. C. Sense and antisense transfection analysis of tau function: tau influences net microtubule assembly, neurite outgrowth and neuritic stability. *J. Cell Sci.* **107** (**Pt 4,** 869–879 (1994).

16.   Huang, Y. & Mucke, L. Alzheimer mechanisms and therapeutic strategies. *Cell* **148,** 1204–1222 (2012).

17.   Kosik, K. S., Joachim, C. L. & Selkoe, D. J. Microtubule-associated protein tau (tau) is a major antigenic component of paired helical filaments in Alzheimer disease. *Proc. Natl. Acad. Sci. U. S. A.* **83,** 4044–4048 (1986).

18.   Hutton, M. *et al.* Association of missense and 5'-splice-site mutations in tau with the inherited dementia FTDP-17. *Nature* **393,** 702–705 (1998).

19.   Clark, L. N. *et al.* Pathogenic implications of mutations in the tau gene in pallido-ponto-nigral degeneration and related neurodegenerative disorders linked to chromosome 17. *Proc. Natl. Acad. Sci. U. S. A.* **95,** 13103–13107 (1998).

20.   Spillantini, M. G. *et al.* Mutation in the tau gene in familial multiple system tauopathy with presenile dementia. *Proc. Natl. Acad. Sci. U. S. A.* **95,** 7737–7741 (1998).

21.   McKee, A. C. *et al.* Chronic traumatic encephalopathy in athletes: progressive tauopathy after repetitive head injury. *J. Neuropathol. Exp. Neurol.* **68,** 709–735 (2009).

22.   Himmler, A., Drechsel, D., Kirschner, M. W. & Martin, D. W. Tau consists of a set of proteins with repeated C-terminal microtubule-binding domains and variable N-terminal domains. *Mol. Cell. Biol.* **9,** 1381–1388 (1989).

23.   Kanai, Y., Chen, J. & Hirokawa, N. Microtubule bundling by tau proteins in vivo: analysis of functional domains. *EMBO J.* **11,** 3953–3961 (1992).

24.   Chen, J., Kanai, Y., Cowan, N. J. & Hirokawa, N. Projection domains of MAP2 and tau determine spacings between microtubules in dendrites and axons. *Nature* **360,** 674–677 (1992).

25.   Lee, G., Cowan, N. & Kirschner, M. The primary structure and heterogeneity of tau protein from mouse brain. *Science (80-.).* **239,** 285–288 (1988).

26.   Butner, K. A. & Kirschner, M. W. Tau protein binds to microtubules

through a flexible array of distributed weak sites. *J. Cell Biol.* **115,** 717–730 (1991).

27. Lee, G., Neve, R. L. & Kosik, K. S. The microtubule binding domain of tau protein. *Neuron* **2,** 1615–1624 (1989).

28. Goode, B. L. & Feinstein, S. C. Identification of a novel microtubule binding and assembly domain in the developmentally regulated inter-repeat region of tau. *J. Cell Biol.* **124,** 769–781 (1994).

29. Schweers, O., Schönbrunn-Hanebeck, E., Marx, A. & Mandelkow, E. Structural studies of tau protein and Alzheimer paired helical filaments show no evidence for beta-structure. *J. Biol. Chem.* **269,** 24290–24297 (1994).

30. Levine, Z. A., Larini, L., LaPointe, N. E., Feinstein, S. C. & Shea, J.-E. Regulation and aggregation of intrinsically disordered peptides. *Proc. Natl. Acad. Sci.* **112,** 201418155 (2015).

31. Kadavath, H. *et al.* Tau stabilizes microtubules by binding at the interface between tubulin heterodimers. *Proc. Natl. Acad. Sci.* **112** , 7501–7506 (2015).

32. Choi, M. C. *et al.* Human microtubule-associated-protein tau regulates the number of protofilaments in microtubules: A synchrotron X-ray scattering study. *Biophys. J.* **97,** 519–527 (2009).

33. Derry, W. B., Wilson, L. & Jordan, M. A. Substoichiometric binding of taxol suppresses microtubule dynamics. *Biochemistry* **34,** 2203–2211 (1995).

34. Nogales, E., Wolf, S. G., Khan, I. A., Ludueña, R. F. & Downing, K. H. Structure of tubulin at 6.5 A and location of the taxol-binding site. *Nature* **375,** 424–427 (1995).

35. Elie-Caille, C. *et al.* Straight GDP-Tubulin Protofilaments Form in the Presence of Taxol. *Curr. Biol.* **17,** 1765–1770 (2007).

36. Black, M. M., Slaughter, T., Moshiach, S., Obrocka, M. & Fischer, I. Tau is enriched on dynamic microtubules in the distal region of growing axons. *J. Neurosci.* **16,** 3601–3619 (1996).

37. Parsegian, V. A., Rand, R. P., Fuller, N. L. & Rau, D. C. Osmotic stress for the direct measurement of intermolecular forces. *Methods Enzymol.* **127,** 400–416 (1986).

38. Jones, J. B. & Safinya, C. R. Interplay between liquid crystalline and isotropic gels in self-assembled neurofilament networks. *Biophys. J.* **95,** 823–835 (2008).

39. Janmey, P. A., Leterrier, J. F. & Herrmann, H. Assembly and structure of neurofilaments. *Curr. Opin. Colloid Interface Sci.* **8,** 40–47 (2003).

40. Needleman, D. J. *et al.* Synchrotron X-ray diffraction study of microtubules buckling and bundling under osmotic stress: A probe of interprotofilament interactions. *Phys. Rev. Lett.* **93,** 198104 (2004).

41. Needleman, D. J. *et al.* Radial compression of microtubules and the mechanism of action of taxol and associated proteins. *Biophys. J.* **89,** 3410–3423 (2005).

42. Andreu, J. M. *et al.* Low resolution structure of microtubules in solution. *J. Mol. Biol.* **226,** 169–184 (1992).

43. Raviv, U. *et al.* Microtubule protofilament number is modulated in a stepwise fashion by the charge density of an enveloping layer. *Biophys. J.* **92,** 278–287 (2007).

44. Raviv, U. *et al.* Cationic liposome-microtubule complexes: pathways to the formation of two-state lipid-protein nanotubes with open or closed ends. *Proc. Natl. Acad. Sci. U. S. A.* **102,** 11167–11172 (2005).

45. Devanand, K. & Selser, J. C. Asymptotic Behavior and Long-Range Interactions in Aqueous Solutions of Poly (ethylene oxide). *Macromolecules* **24,** 5943–5947 (1991).

46. Casassa, E. Equilibrium distribution of flexible polymer chains between a macroscopic solution phase and small voids. *J. Polym. Sci. Part B Polym. Lett.* **5,** 773–778 (1967).

47. Daoud, M. & De Gennes, P. G. Statistics of macromolecular solutions trapped in small pores. *J. Phys.* **38,** 85–93 (1977).

48. Mylonas, E. *et al.* Domain conformation of tau protein studied by solution small-angle X-ray scattering. *Biochemistry* **47,** 10345–10353 (2008).

49. *Small-Angle X-Ray Scattering*. (Academic Press, 1982).

50. Kohn, J. E. *et al.* Random-coil behavior and the dimensions of chemically unfolded proteins. *Proc. Natl. Acad. Sci. U. S. A.* **101,** 12491–12496 (2004).

51. Shkumatov, A. V, Chinnathambi, S., Mandelkow, E. & Svergun, D. I. Structural memory of natively unfolded tau protein detected by small-angle X-ray scattering. *Proteins Struct. Funct. Bioinforma.* **79,** 2122–2131 (2011).

52. Nath, A. *et al.* The conformational ensembles of α-synuclein and tau: Combining single-molecule FRET and simulations. *Biophys. J.* **103,** 1940–

1949 (2012).

53. Ludueña, R. F. A Hypothesis on the Origin and Evolution of Tubulin. *Int. Rev. Cell Mol. Biol.* **302,** 41–185 (2013).

54. van den Heuvel, M. G. L., de Graaff, M. P., Lemay, S. G. & Dekker, C. Electrophoresis of individual microtubules in microchannels. *Proc. Natl. Acad. Sci. U. S. A.* **104,** 7770–7775 (2007).

55. Sparnaay, M. The interaction between two cylinder shaped colloid particles. *Recueil* **78,** 680–709 (1959).

56. Ohshima, H. & Hyono, A. Electrostatic interaction between two cylindrical soft particles. *J. Colloid Interface Sci.* **333,** 202–208 (2009).

57. Tuszyński, J. A. *et al.* Molecular dynamics simulations of tubulin structure and calculations of electrostatic properties of microtubules. *Math. Comput. Model.* **41,** 1055–1070 (2005).

58. Tuinier, R. & Fleer, G. J. Concentration and solvency effects on the pair interaction between colloidal particles in a solution of nonadsorbing polymer. *Macromolecules* **37,** 8764–8772 (2004).

59. Jones, C. W., Wang, J. C., Ferrone, F. A., Briehl, R. W. & Turner, M. S. Interactions between sickle hemoglobin fibers. *Faraday Discuss.* **123,** 221–236; discussion 303–322, 419–421 (2003).

60. Cohen, J. A. & Highsmith, S. An improved fit to Website osmotic pressure data. *Biophys. J.* **73,** 1689–1694 (1997).

61. Dobrynin, A. V & Rubinstein, M. Adsorption of hydrophobic polyelectrolytes at oppositely charged surfaces. *Macromolecules* **35,** 2754–2768 (2002).

62. Leermakers, F. A. M., Jho, Y.-S. & Zhulina, E. B. Modeling of the 3RS tau protein with self-consistent field method and Monte Carlo simulation. *Soft Matter* **6,** 5533 (2010).

63. Jho, Y. S., Zhulina, E. B., Kim, M. W. & Pincus, P. A. Monte Carlo simulations of tau proteins: Effect of phosphorylation. *Biophys. J.* **99,** 2387–2397 (2010).

64. Schaap, I. A. T., Hoffmann, B., Carrasco, C., Merkel, R. & Schmidt, C. F. Tau protein binding forms a 1 nm thick layer along protofilaments without affecting the radial elasticity of microtubules. *J. Struct. Biol.* **158,** 282–292 (2007).

65. Witten, T. A. & Pincus, P. Structure and Viscosity of Interpenetrating

Polyelectrolyte Chains. *Europhys. Lett.* **3,** 315–320 (2007).

66. Pincus, P. Colloid stabilization with grafted polyelectrolytes. *Macromolecules* **24,** 2912–2919 (1991).

67. Needleman, D. J. *et al.* Higher-order assembly of microtubules by counterions: from hexagonal bundles to living necklaces. *Proc. Natl. Acad. Sci. U. S. A.* **101,** 16099–16103 (2004).

68. Beck, R., Deek, J., Jones, J. B. & Safinya, C. R. Gel-expanded to gel-condensed transition in neurofilament networks revealed by direct force measurements. *Nat. Mater.* **9,** 40–46 (2010).

69. Safinya, C. R., Deek, J., Beck, R., Jones, J. B. & Li, Y. Assembly of Biological Nanostructures: Isotropic and Liquid Crystalline Phases of Neurofilament Hydrogels. *Annu. Rev. Condens. Matter Phys.* **6,** under review (2014).

70. Kornreich, M. *et al.* Composite bottlebrush mechanics: α-internexin fine-tunes neurofilament network properties. *Soft Matter* **11,** 5839–5849 (2015).

71. Kosik, K. S., Orecchio, L. D., Bakalis, S. & Neve, R. L. Developmentally regulated expression of specific tau sequences. *Neuron* **2,** 1389–1397 (1989).

72. Hong, M. *et al.* Mutation-specific functional impairments in distinct tau isoforms of hereditary FTDP-17. *Science* **282,** 1914–1917 (1998).

73. Conway, L., Gramlich, M. W., Ali Tabei, S. M. & Ross, J. L. Microtubule orientation and spacing within bundles is critical for long-range kinesin-1 motility. *Cytoskeleton* **71,** 595–610 (2014).

74. Miller, H. P. & Wilson, L. Preparation of microtubule protein and purified tubulin from bovine brain by cycles of assembly and disassembly and phosphocellulose chromatography. *Methods Cell Biol.* **95,** 2–15 (2010).

75. Toso, R. J., Jordan, M. A., Farrell, K. W., Matsumoto, B. & Wilson, L. Kinetic stabilization of microtubule dynamic instability in vitro by vinblastine. *Biochemistry* **32,** 1285–1293 (1993).

76. Bunker, J. M., Wilson, L., Jordan, M. A. & Feinstein, S. C. Modulation of microtubule dynamics by tau in living cells: implications for development and neurodegeneration. *Mol. Biol. Cell* **15,** 2720–2728 (2004).

77. Derjaguin, B. & Landau, L. Theory of the stability of strongly charged lyophobic sols and of the adhesion of strongly charged particles in solutions of electrolytes. *Prog. Surf. Sci.* **43,** 30–59 (1993).

78. Israelachvili, J. N. *Intermolecular & Surface Forces*. (Academic Press Limited, 1992).

79. Sackett, D. L. Structure and function in the tubulin dimer and the role of the acidic carboxyl terminus. *Subcell. Biochem.* **24,** 255–302 (1995).

80. Carlier, M. F. & Pantaloni, D. Taxol effect on tubulin polymerization and associated guanosine 5'-triphosphate hydrolysis. *Biochemistry* **22,** 4814–4822 (1983).

81. Christos, G. A., Carnie, S. L. & Creamer, T. P. Monte Carlo simulations of partially ionized polyelectrolytes: conformational properties. *Macromolecules* **25,** 1121–1124 (1992).

4. Tau mediates microtubule bundle architectures mimicking fascicles of microtubules found in the axon initial segment[1]

Tau, an intrinsically disordered protein (IDP) expressed in neuronal axons, binds to microtubules and regulates their dynamics. Tau dysfunction is linked to neurodegeneration but the molecular mechanism of Tau-induced microtubule bundling remains unknown. Although there have been observations of string-like microtubule bundles in the axon initial segment (AIS) and hexagonal bundles in neurite-like processes in non-neuronal cells overexpressing Tau, cell free reconstitutions have been unable to replicate either geometries. We report the energy landscape of Tau-mediated, GTP-dependent "active" microtubule bundles at 37°C revealed by synchrotron SAXS and TEM. Widely-spaced bundles (energy minimum at microtubule wall-to-wall distance $D_{\text{w-w}} \approx 26\text{-}38$ nm) with hexagonally-ordered and string-like symmetry are observed, the latter mimicking bundles found in the AIS. A second minimum ($D_{\text{w-w}} \approx 16\text{-}23$ nm), indicative of antiparallel dipole-dipole interactions of interpenetrating Tau projection domains (PDs), is revealed via osmotic pressure. Widely-spaced bundles reveal that anionic block repulsions of Tau PDs compete with transient, short-range cationic/anionic charge-charge attractions mediated by opposing weakly penetrating PDs, a sum of sub-$k_{\text{B}}T$ interactions heretofore unreported in IDP systems. Although previous work postulated that the PD of the amino-terminal tail was required for widely-spaced bundles, remarkably, amino-

---

terminal tail truncation demonstrates the carboxyl-terminal tail alone can similarly mediate relatively wide-spacings. This landscape would be significantly affected by Tau charge-altering modifications associated with neurodegeneration.

4.1. Introduction

Microtubules, a component of the eukaryotic cytoskeleton, are made up of αβ-tubulin heterodimers that dynamically assemble into hollow nanotubes composed of straight protofilaments[1]. Microtubules are involved in a wide variety of cell functions (e.g. intracellular trafficking, cell motility, chromosome segregation) through functionalization, in part, by microtubule-associated proteins (MAPs). One MAP in particular, Tau, is localized to neuronal axons and stabilizes microtubules upon binding (Fig. 4.1a) by partially suppressing microtubule dynamic instability (alternating periods of polymerization of tubulin into microtubules interrupted by catastrophe, or the rapid disassembly of microtubules following loss of the microtubule GTP cap). While Tau is developmentally regulated in neurons, Tau dysfunction in mature axons has been linked to many neurodegenerative "tauopathies" (including Alzheimer's[2], FTDP-17[3], and, more recently, chronic traumatic encephalopathy in athletes suffering concussions[4]). Tau consists of an amino-terminal tail (NTT) containing a projection domain (PD) and proline-rich region (PRR), followed by the

microtubule-binding region (MTBR), and a carboxyl-terminal tail (CTT). Alternative splicing results in 6 wild type (WT) isoforms (Fig. 4.1b); the MTBR either has 4 or 3 imperfect repeats (4R- or 3R- Tau isoforms), depending on expression/non-expression of exon 10. The PD length depends on expression of exons 2 and/or 3 with +/+, +/-, and -/- resulting in long (-L), medium (-M), and short (-S) length PDs, respectively.
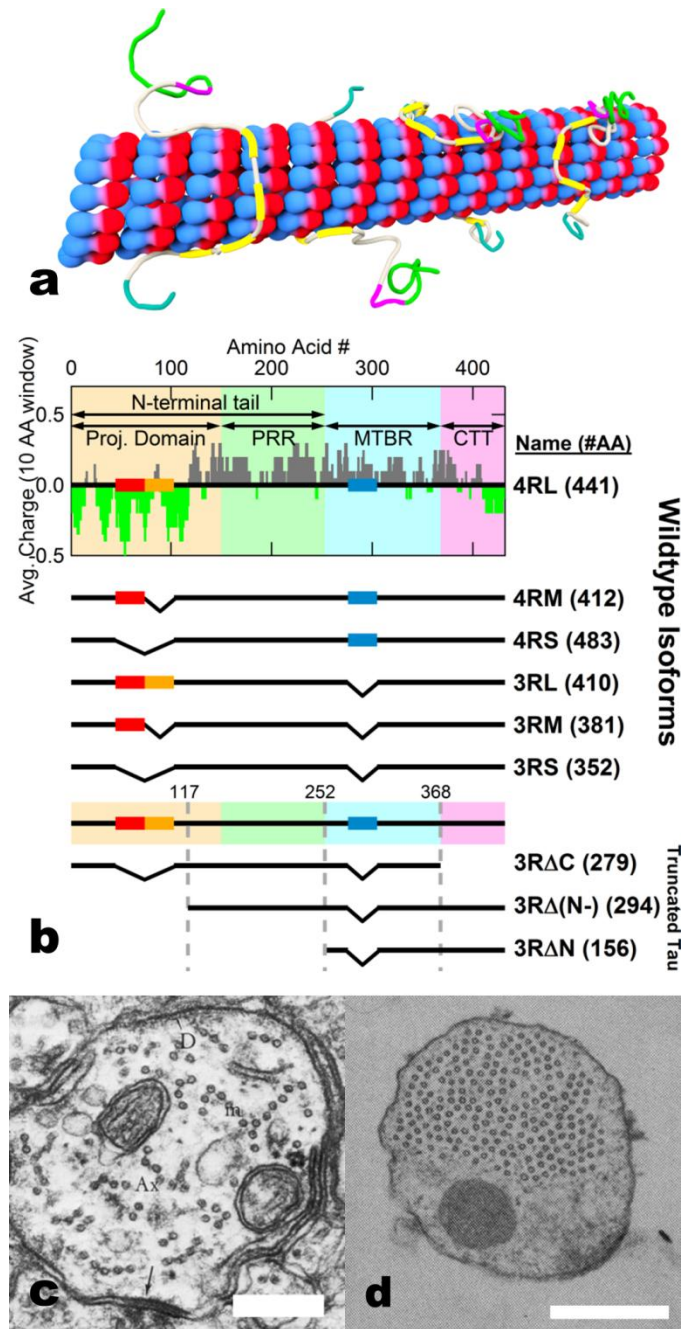
Fig. 4.1| Tau-mediated microtubule assemblies and Tau charge distribution. a, Cartoon showing Tau binding to a microtubule (red/blue) through its microtubule-binding region (yellow), with the projection domain (green/purple) and CTT (gray/teal) extending off the microtubule surface. b, The average charge of fully expressed 4RL Tau (top) as a function of primary sequence, with alternative splicing of exons 2 (red rectangle), 3 (orange), and 10 (blue) resulting in the 5 additional wild type isoforms. Wild type Tau consists of the amino-terminal tail (NTT) which includes the projection domain (PD, orange background) and proline-rich region (PRR, green), the microtubule-binding

region (MTBR, blue) and carboxyl-terminal tail (CTT, pink). Truncated Tau constructs were designed to understand the domain dependence of the CTT (3RSΔC, missing CTT), anionic component of the projection domain (3RΔ(N-), missing anionic block of NTT), and the entire NTT (3RΔN, missing NTT). **c,** Prior electron microscopy revealed linear microtubule bundles in the axon initial segment (adapted from Peters *et al.*[5]). **d,** Subsequent Tau cDNA transfection of Sf9 cells revealed hexagonal arrays of microtubules in neurite-like processes (adapted from Chen *et al.*[6]). Scale bars, 250 nm (**c**) and 500 nm (**d**).

While it is generally accepted that Tau interacts with individual microtubules, the interactions between microtubules mediated by Tau remains unclear. Prior to the discovery of Tau, groundbreaking electron microscopy studies of the fine structure of axons in mature rat hippocampal neurons revealed[5,7] that the AIS contained widely-spaced ($D_{w\text{-}w} \approx 25\text{-}30$ nm) string-like microtubule bundles ("fascicles of microtubules", Fig. 4.1c). Fascicles are now believed[8] to be a cardinal feature of the AIS, acting as a filter by allowing passage of kinesin motors with axon-specific cargo and thus contributing to neuronal polarity (i.e. ensuring distinct molecular environments for axons and dendrites). Later, seminal studies[6,9] of non-neuronal cells overexpressing transfected Tau cDNA had concluded that the Tau PD determines inter-microtubule distances in observed widely-spaced hexagonally-ordered microtubule arrays (Fig. 4.1D), although the studies could not discern whether bundles result from the presence of Tau-mediated attractions or due to a repulsive lattice under confinement. The answer to the very important question of whether Tau, which is localized to the axon region, induces microtubule bundles similar to those found in the AIS, remains controversial. Cell free

reconstitutions[10,11] resulted in no microtubule bundles which led to the conclusion that the absence of bundles was due to the purely repulsive nature of Tau. Complicating matters was the frequent use of paclitaxel to stabilize microtubules[12,13]. Synchrotron small-angle X-ray-scattering (SAXS) has shown[14] that WT Tau does not bundle paclitaxel-stabilized microtubules over the relevant Tau-coverage regime in axons[15]. In eliminating microtubule dynamic instability it was possible the normal behavior of microtubules was being suppressed, without it being clear that paclitaxel-stabilized results were reflective of biological reality.

Here, we report on experiments designed to elucidate the molecular mechanism of Tau-mediated microtubule-microtubule interactions in paclitaxel-free reaction mixtures of tubulin, GTP, and WT Tau/truncated Tau (Φ_{Tau} = 1/40 to 1/5) under dissipative out-of-equilibrium conditions at 37°C (i.e. mimicking the cytoskeletal environment of nerve cells with samples consuming the energy released by GTP hydrolysis). SAXS and plastic embedded transmission electron microscopy (TEM) were used to obtain both angstrom-resolution ensemble-averaged structural information and nanometer-scale real-space local fine structure, respectively. Remarkably, we observed dissipative, "active" (i.e. GTP-dependent and at 37° C) steady-state structures that were stable over time (> 24 hours). The microtubule reaction mixture exhibited Tau-induced phase separation into microtubule bundles (forming domains of high and low concentrations of microtubules in optical microscopy), in contrast to paclitaxel-

stabilized microtubules[14], unambiguously demonstrating an attractive component to Tau-mediated interactions between widely-spaced microtubules.

4.2. Methods

4.2.1. Purification of Proteins (Tubulin, WT and Truncated Tau)

Tubulin was purified from MAP-rich microtubules extracted from bovine brains. MAP-rich microtubules were obtained from crude brain extract by three polymerization/depolymerization cycles, after which tubulin was separated from MAPs with a phosphocellulose anionic exchange column. Tubulin was suspended in PEM50 (50 mM PIPES pH 6.8, 1 mM $MgSO_4$, and 1 mM EGTA) with protein concentration between 7 and 12 mg mL^{-1}, as measured by BSA concentration standard. Solution was drop-frozen in liquid nitrogen and stored in a -70° C freezer until use.

Tau was expressed in BL21(DE3) competent cells (Life Technologies, Carlsbad, CA) that were transfected with the pRK172 expression vector, coded for the appropriate wild type isoform or truncated Tau. After incubation in auto-induction media (10g of tryptone (CAS#: 91079-40-2), 5g of yeast extract (CAS#: 8013-01-2), 0.5g of dextrose (CAS#: 50-99-7), 2g of α-D-lactose (CAS#: 5989-81-1) and 5 mL of glycerol (CAS#: 56-81-5) per liter of 25 mM Na_2HPO_4, 25 mM KH_2PO_4, 50 mM NH_4Cl, 5 mM Na_2SO_4 in DI water) for 24 hours, cells were collected, lysed, and resuspended in BRB80 buffer (80 mM PIPES at pH 6.8, 1

mM EGTA, 1 mM MgSO$_4$). The solution were then bound to a phosphocellulose anionic exchange column, eluted with increasing concentration of (NH$_4$)$_2$SO$_4$ in BRB80. Tau was further purified by a HiTrap hydrophobic interaction chromatography column (GE Healthcare Life Sciences, Pittsburgh, PA), eluted with decreasing concentration of (NH$_4$)$_2$SO$_4$ in BRB80. Tau was then concentrated and buffer exchanged through successive centrifugation cycles using Amicon Ultra-15 Centrifugal Units with MWCO=10,000 (EMD Millipore, Darmstadt, Germany). The concentration of each tau stock was determined by SDS-PAGE comparison with a Tau mass standard (originally measured via amino acid analysis).

Truncated Tau mutants were designed via QuikChange Site-Directed Mutagenesis Kit (Agilent Technologies, Santa Clara, CA) with appropriate introduction/deletion of start and stop codons: 3RSΔC (truncation of the entire CTT, deleting residues 280-352 of 3RS), 3RΔ(N-) (truncation of the anionic component of the NTT, deleting residues 2-117 of 3RL), and 3RΔN (truncation of the entire NTT, deleting residues 2-255 of 3RL). Truncated Tau were then expressed/purified, as above.

4.2.2. Sample Preparation

After thawing frozen tubulin and Tau stocks, samples were prepared on ice, mixing tubulin, GTP, and Tau such that final concentrations were 5 mg mL^{-1}, 2

103

mM, appropriate molar ratio of Tau to tubulin, respectively, in a final volume of 50 μL of PEM50 buffer. Samples were then polymerized in a 37° C for 40 minutes. If necessary, sample was brought to appropriate KCl concentration.

4.2.3. Osmotic Pressure Samples

A previous study[16] measured the osmotic pressure (in Pa), P, of an aqueous solution of varying concentrations (cg mL^{-1}), $wt\%$, of poly(ethylene oxide) (M_W=105,000 g mole^{-1}) at 35° C, which was taken as an reasonable approximation of the behavior of PEO100k at 37° C, absent further data. Data was fit to a 2nd order polynomial (following the mathematical form of a virial expansion) to determine a formula to relate an arbitrary PEO100k concentration to a corresponding osmotic pressure (P, in Pa):

$$P = 147.38\text{wt}\% + 338.19\text{wt}\% \qquad [\text{Pa}] \qquad (\text{Eq. 4.1})$$

PEO100k was used as the osmotic depletant of choice compared to better-characterized depletants to parameters unique to our system: as stable inter-microtubule distances of up to 38 nm were observed, the size of the depletant had to be equal or greater than that distance in order to create a concentration differential inside/outside the microtubule bundle. Prior work[17] measured the radius of gyration (R_G) of a function of PEO molecular weight (MW):

$$R_G = 0.215 MW^{0.583} \qquad [\text{nm}] \qquad (\text{Eq. 4.2})$$

Thus, the effective depletant radius[18], a $= 2R_G\pi^{-1/2} = 19.95$ nm, or an effective depletant diameter, $d \approx 40$ nm, satisfies our experimental conditions that polymer not penetrate the space between microtubules in microtubule bundles.

4.2.4. Small-angle X-ray scattering (SAXS)

After polymerization, samples are loaded into 1.5 mm diameter quartz mark tubes (Hilgenberg GmbH, Malsfeld, Germany) and subsequently spun in a capillary rotor in a Universal 320 R centrifuge (Hettich, Kirchlengern, Germany) at 10,000 RPM, 37° C for 30 minutes to protein density suitable for SAXS. To ensure structures were not induced by centrifugation, samples were observed over a period of 36 hours, with no major changes to scattering or extracted parameters. Additionally, phase separation of microtubules into bundles with the addition of Tau was observed in DIC microscopy without centrifugation.

After centrifugation, varying concentration of PEO100k in PEM50 was added for SAXS samples under osmotic pressure. Samples are subsequently sealed with epoxy and placed in a custom made sample oven (maintained at 37° C) with X-ray-transparent Kapton windows for scattering measurements.

SAXS measurements are carried out at the Stanford Synchrotron Radiation Laboratory (Palo Alto, CA) beamline 4-2 at 9 KeV (λ=1.3776 Å) with a Si(111) monochromator. Scattering data is taken with a 2D area detector (MarUSA, Evanston, Illinois) with a sample to detector distance of $\approx$3.5 meters (calibrated

with a silver behenate control). X-ray beam size on the sample was 150 μm in the vertical and 200 μm in the horizontal directions.

4.2.5 SAXS Analysis

Scattering data was azimuthally-averaged and small angle scattering was subsequently background subtracted by fitting the minima of scattering intensities to a polynomial equation. Data was then fit to the appropriate model using a custom MATLAB fitting routine using the Levenberg-Marquadt non-linear fitting routine. microtubules were modeled as homogenous, hollow cylinders (with no expected scattering from Tau/PEO due to low electron density relative to water) with ensemble-averaged inner radius $<r_{in}>$ (a fit parameter), wall thickness δ (49 Å, an input parameter[19]), and microtubule length L (20 μm, an input parameter[20]), averaged all orientations in q-space:

$$|F_{MT}|^2 \propto |[\sin(q_z L/2)/q_\perp q_z][(r_{in}+\delta)J_1(q_\perp(r_{in}+\delta))-r_{in}J_1(q_\perp r_{in})]|^2 \qquad \text{(Eq. 4.3)}$$

Where $q_\perp$, q_z are wavevectors perpendicular and parallel to the tubular axis, and J_1 is the Bessel function of order 1. The structure-factor peaks (at reciprocal lattice vector for a hexagonal array, $|G_{hk}| = q_{10}(h^2+k^2+hk)^{1/2}$) were modeled as squared lorentzians with peak amplitude A_{hk} (a fit parameter) and peak width κ_{hk} (a fit parameter, with κ_{10} corresponding to the average bundle width $L \approx 2(\pi\ln4)^{1/2}/\kappa_{10})$[13]:

$S(q_\perp) = \Sigma([A_{hk}/(\kappa_{hk}^2+(q_\perp-G_{hk})^2)]^2$ (Eq. 4.4)

Fits of the intensity data, $I(q)= |F_{\text{microtubule}}|^2 \, S(q_\perp)$ yielded the hexagonal lattice

parameter a_H (=$4\pi/[3^{1/2}q_{10}]$) and ensemble-averaged inner radius $<r_{\text{in}}>$. κ_{10} was

fit independently while all other κ_{hk} fit simultaneously, with κ_{hk} approximately

twice that of κ_{10}.

4.2.6 Plastic embedded TEM Sample Preparation and TEM

Samples for thin sections were centrifuged to a pellet at 10,000 rpm in 37˚ C

for 30 minutes. Supernatant was removed and pellet fixed with 2%

glutaraldehyde and 4% tannic acid overnight. The pellet was stained with 0.8%

OsO_4 in PEM50 buffer for 1 hour and subsequently rinsed 4 times with PEM50.

Another stain of 1% uranyl acetate stain was applied for 1 hr and rinsed with

deionized water.

Fixed and stained pellets were subsequently dehydrated with

25%/50%/75%/100% solutions of acetone in deionized water for 15 minutes

apiece. Samples were embedded in resin then embedded in spur plastic and

incubated overnight, with resin poured into flat embedding molds and held at

65˚ C for 48 hours and cooled overnight.

Plastic embedded samples were then cut to ≈50 nm slices with a

microkeratome and transferred to highly stable Formvar carbon-coated copped

EM grids (Ted Pella, Redding, CA). Data were taken using the JEOL 1230 Transmission Electron Microscope.

4.2.7 DIC Samples and DIC

A SensiCam^{QE} CCD camera (Cooke, Auburn Hills, MI) mounted on a Nikon Diaphot 300 with Xenon lamp (Sutter Instrument, Novato, CA) was used for optical microscopy measurements. Samples were centrifuged to a pellet at 10,000 rpm for 30 minutes in 37° C and placed between two microscopic slides sealed by wax. Images were taken while slides were kept at 37° C by heat stage.

4.2.8 Calculation of R_G

Previously, the radius of gyration (R_G) of WT Tau and truncated Tau domains in solution were found[21,22] to scale as an unstructured protein with random-coil behavior, with $R_G=0.1927N^{0.588}$ nm, which was subsequently used to calculate the R_G of the projection domain and truncated Tau used in our experiments.

4.3   Results

4.3.1 SAXS reveals hexagonally-ordered MT bundles mediated by Tau

SAXS is especially well-suited to investigate Tau-directed higher-order assembly of microtubules, as solution scattering yields assembly structures in

near physical conditions without tags/labels. Azimuthally-averaged scattering of microtubules co-assembled with WT Tau isoforms ($\Phi_{Tau}=1/10$) registers Bragg peak positions consistent with a 2D-hexagonal array (q_{10}, $q_{11}=3^{1/2}q_{10}$, $q_{20}=2q_{10}$, $q_{21}=7^{1/2}q_{10}$, $q_{30}=3q_{10}$, $q_{22}=12^{1/2}q_{10}$) of microtubules with center-to-center distance $a_H = 4\pi/(3)^{1/2}q_{10}$ (Fig. 4.2a). Some peak positions are not apparent due to their proximity to the form factor minima (in particular, q_{11} and q_{22}), necessitating line-shape analysis to separate scattering from individual microtubules (form factor, see Fig. 4.2a, bottom profile), the lattice of microtubules (structure factor), and background small-angle scattering. Following previous work[14,23], we modeled microtubules as hollow cylinders with ensemble-averaged inner radius $<r_{in}>$ (a fit parameter) and constant wall thickness δ (49 Å, in agreement with electron microscopy of microtubules[19]). Each structure factor peak at reciprocal lattice vector $q_{hk} = q_{10}(h^2+k^2+hk)^{1/2}$ was represented as squared lorentzians (fit results as red solid lines in Fig. 4.2a, see Methods).
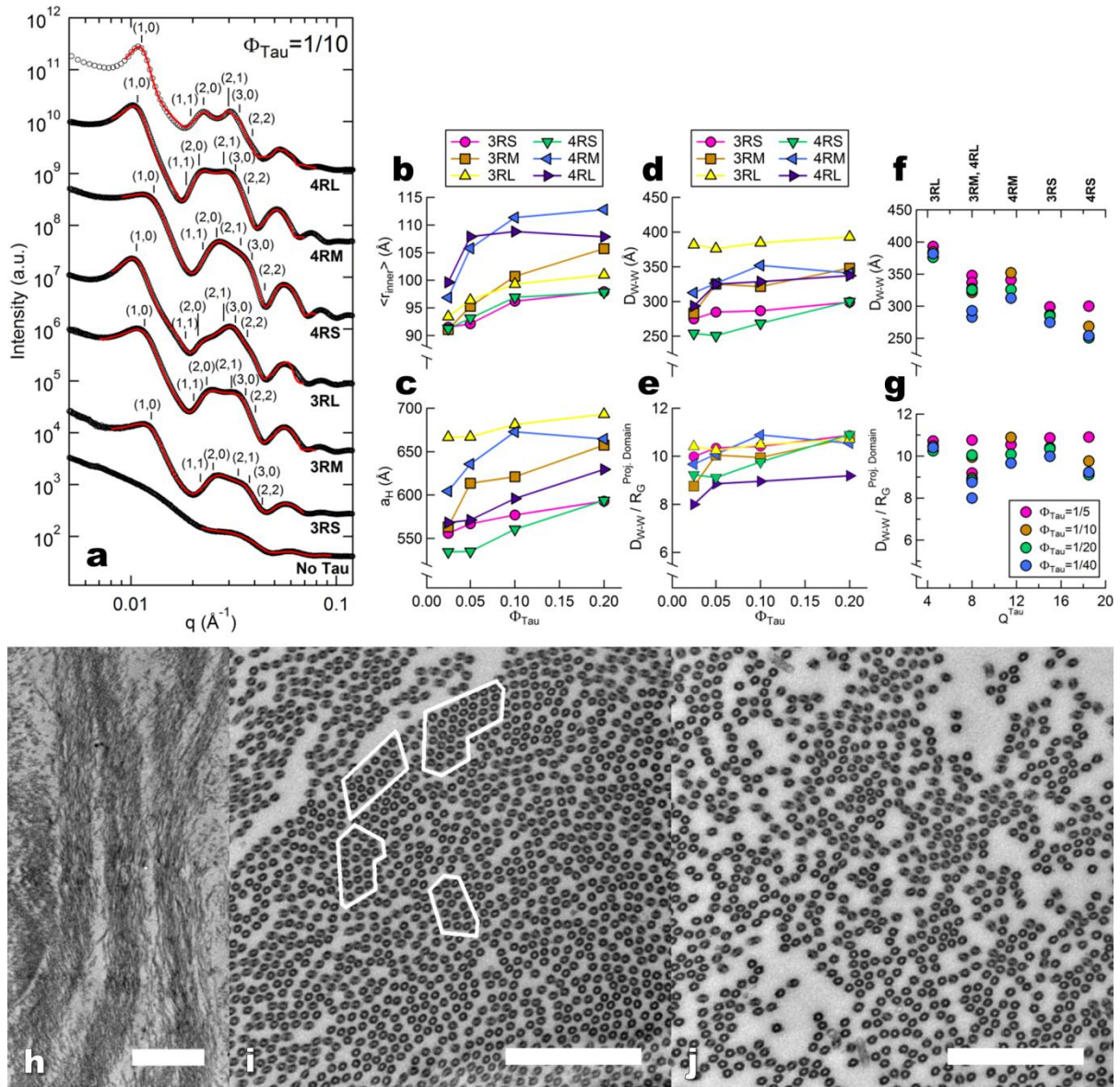
Fig. 4.2| SAXS and TEM show that Tau-assembled microtubules in active bundles at 37° C in 2 mM GTP recapitulate key *in vivo* features of microtubule wall-to-wall spacing and linear bundles. a, Azimuthally-averaged SAXS data of WT Tau and microtubules registers Bragg peak positions consistent with hexagonal lattices for all six isoforms, as opposed to just microtubule form factor for no Tau (bottom profile). b-e, Line-shape analysis of SAXS data [resultant fits in red on (a)] yields the ensemble-averaged microtubule inner radius $<r_{in}>$ (b), hexagonal lattice parameter a_H (c), wall-to-wall distance D_{w-w} (d), and D_{w-w} normalized by the calculated projection domain radius of gyration, R_G^{PD} (e) (see Methods). f, g, D_{w-w} and D_{w-w}/R_G^{PD} as a function of Tau net charge (Q^{Tau}) shows a monotonic decrease in D_{w-w} and a nearly constant $D_{w-w}/R_G^{PD} \approx 8$-11, respectively. h, Electron microscopy of microtubules assembled with Tau ($\Phi_{3RM}=1/20$) at low magnification show distinct bundled domains, demonstrating phase separation.

110

i, Domains of hexagonally-ordered arrays of microtubules (identified in white outlines, Φ_{3RL}=1/20) with vacancies likely resulting from the suppressed (but still occurring) dynamic instability. **j,** Linear bundles of microtubules (Φ_{3RL}=1/20), a result of extensive vacancy introduction and mimicking string-like microtubule bundles in the AIS. In (**i**) and (**j**) the staining process exaggerates the microtubule wall thickness. Scale bars, 1 μm (**h**) and 500 nm [(**i**) and (**j**)].

Even after ≈ 24 hours there are no major changes in scattering, indicating that although the microtubules are dynamic (i.e. hydrolyzing GTP), they have reached a steady state. The fit parameters $<r_{in}>$, a_H, calculated microtubule wall-to-wall distance $D_{w\text{-}w}$ (= a_H - 2($<r_{in}>$ + δ)) and $D_{w\text{-}w}$ normalized to the PD radius of gyration (R_G^{PD}) in solution (2.8/3.3/3.8 nm for –S/–M/–L Tau isoforms, see Methods) are plotted in Figure 2b-e as a function of increasing Φ_{Tau}. The $D_{w\text{-}w}$ ≈ 26-38 nm is similar to inter-microtubule spacings seen in cells (Fig. 4.1c). For both 3-repeat and 4-repeat Tau isoforms increasing PD length (increasing anionic block size, Fig. 4.1b) leads to increases in $D_{w\text{-}w}$ (e.g. at Φ_{Tau} = 0.1 in Fig. 4.2d $D_{w\text{-}w}$ increases from 29.9 nm (26.9 nm) to 38.5 nm (32.7 nm) in going from 3RS (4RS) to 3RL (4RL)). This behavior is consistent with observations in transfected cells[6,9] where Tau isoforms with longer PDs exhibit microtubule bundles with larger spacing. Notably, $D_{w\text{-}w}/R_G^{PD}$ is nearly constant (≈ 8-11, Fig. 4.2e). Surprisingly, for the same PD, smaller 3-repeat isoforms show a larger $D_{w\text{-}w}$ compared to longer 4-repeat isoforms. This may be appreciated by plotting $D_{w\text{-}w}$ and $D_{w\text{-}w}/R_G^{PD}$ for the six WT isoforms as a function of the total overall charge of Tau (Q^{Tau}, Fig. 4.2f,g), where we see that $D_{w\text{-}w}$ decreases systematically as the

overall cationic charge of Tau increases, indicating the electrostatic nature of Tau-mediated attractions between anionic microtubules.

4.3.2 TEM reveals active MT architecture mimicking that of the AIS

TEM independently confirms phase separation of microtubules into bundles (Fig. 4.2h, Φ_{3RM} = 1/20) seen in DIC microscopy. TEM cross-sections exhibit microtubule domains in widely-spaced hexagonally-ordered 2D arrays (Φ_{3RL}=1/20, white outlines in Fig. 4.2i), consistent with SAXS diffraction peaks. However, there is also an additional feature not apparent in SAXS data: vacancies amidst areas of high microtubule density (akin to vacancy defects in crystalline materials). The vacancies are likely the result of the dissipative nature of the reaction mixture: although Tau partially suppresses dynamic instability in a Tau-concentration dependent manner[24], microtubule dynamic instability is still occurring (for $\Phi_{Tau} \leq 1/5$) and introduces significant vacancies in the microtubule array. While the more ordered regions are readily picked up in SAXS, TEM also reveals significantly less ordered regions where microtubules appear to form linear bundles (Φ_{3RL}=1/20, Fig. 4.2j), mimicking string-like bundles ("fascicles of microtubules"[7]) found in the axon initial segment (AIS, Fig. 4.1c). These linear bundles may be the result of extensive vacancy introduction, with microtubules retaining their attraction towards each other but losing one or more of their nearest neighbors.

4.3.3 Truncated Tau shows the Tau PD is unnecessary for MT bundles

To further elucidate the nature of Tau-mediated microtubule-microtubule interactions, truncated Tau mutants (Fig. 4.1a, Truncated Tau) were expressed/purified, and used for similar SAXS measurements (Fig. 4.3a) and subsequent parameter extraction from line-shape analysis (Fig. 4.3b-g): 3RSΔC (truncation of the entire CTT), 3RΔ(N-) (truncation of the anionic component of the NTT), and 3RΔN (truncation of the entire NTT). CTT elimination of 3RS Tau (3RSΔC) has scattering associated with widely-spaced bundles (Fig. 4.3a, top profile) and extracted parameters $<r_{in}>$, a_H, and D_{w-w} (Fig. 4.3b-d) similar to that of 3RS WT Tau (Fig. 4.2b-d), strongly indicating that the CTT is not critical to the WT mechanism of widely-spaced bundles. Elimination of the entire anionic block from the projection domain (3RΔ(N-)) collapses the bundles (Fig. 4.3a, middle profile, Fig. 4.3d, $D_{w-w} \approx 4$-5 nm), with a tight microtubule wall-to-wall spacing comparable to the radius of gyration of 3RΔ(N-) ($R_G = 4.79$ nm)[21]. This result indicates that the anionic block of the PD (a charged polymer containing overall anionic and cationic blocks) presents the dominant component of the repulsive barrier preventing neighboring microtubules from getting closer.
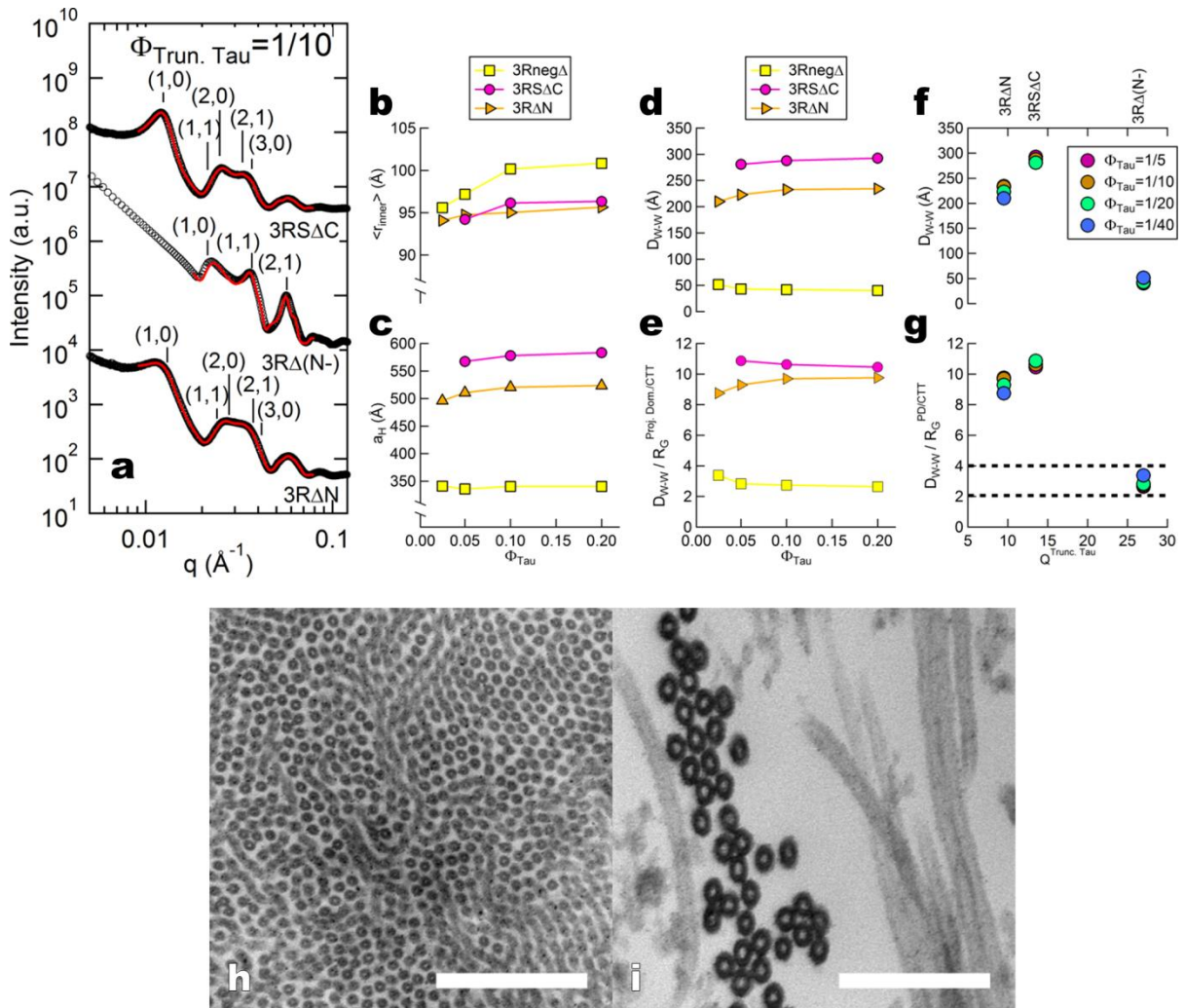
Fig. 4.3| SAXS and TEM of microtubules assembled with truncated Tau show widely- and tightly-spaced microtubule bundles. a, Azimuthally-averaged SAXS data of truncated Tau exhibits scattering consistent with widely-spaced [3RSΔC (missing CTT, top line-shape, q_{10} = 0.0126 Å⁻¹) and 3RΔN (missing NTT, bottom line-shape, q_{10} = 0.0139 Å⁻¹)] and tightly-spaced [3RΔ(N-), (missing anionic section of PD, middle line-shape, q_{10} = 0.0213 Å⁻¹)] hexagonally packed microtubules. b-e, Line-shape analysis of SAXS data [resultant fits in red on (a)] yields $<r_{in}>$ (b), a_H (c), $D_{w\text{-}w}$ (d), and $D_{w\text{-}w}$ normalized by R_G of the PD (3RSΔC), remaining PD (3RΔ(N-)), or CTT (3RΔN) (e). f, g, $D_{w\text{-}w}$ and $D_{w\text{-}w}/R_G^{PD}$ as a function of Truncated Tau net charge ($Q^{Trun.\ Tau}$) reveals a disparity in the data for 3RΔ(N-), when compared to WT Tau (Fig. 4.2f,g), indicative of a different interaction regime between microtubules, likely induced by correlated density fluctuations. h, TEM of widely-spaced microtubule bundles ($\Phi_{3R\Delta N}$=1/20) despite a lack of an entire NTT (and thus, lacking the projection domain). i, Closely-packed microtubules ($\Phi_{3R\Delta(N-)}$=1/20) upon elimination of the anionic component of the projection domain suggesting an interaction mediated by correlated density

fluctuations of the overall cationic 3RΔ(N-) on the microtubule surface. Scale bars, 600 nm (**f**) and 150 nm (**g**).

Removal of the entire NTT of Tau (3RΔN) results in a highly unexpected finding where SAXS data (Fig. 4.3a, bottom profile) gives $D_{\text{w-w}} \approx 22\text{-}24$ nm (Fig. 4.3d) compatible with widely-spaced bundles, despite the nominal size ($R_G = 4.0$ nm) of 3RΔN. The relatively wide spacing seen upon elimination of the NTT (3RΔN) indicates that the NTT is unnecessary for widely-spaced bundling (under these conditions) and that, in its absence, the CTT (Fig. 4.1a) plays an equivalent role in determining the inter-microtubule interactions. TEM of microtubules assembled with 3RΔN and 3RΔ(N-) (Fig. 4.3h,i) clearly show microtubule bundles with relatively wide inter-microtubule spacing and in close contact, respectively, consistent with SAXS data. For 3RΔN and 3RSΔC, $D_{\text{w-w}}/R_G$ ($\approx$8-11, Fig. 4.3e,g) is consistent with the WT ratio (Fig. 4.2e,g), suggesting a similar mechanism of inter-microtubule interactions. However, 3RΔ(N-) presented dramatically smaller $D_{\text{w-w}}$ ($\approx$5 nm) and $D_{\text{w-w}}/R_G$ ($\approx$2-4, Fig. 4.3e,g), suggesting a different inter-microtubule interaction regime.

4.3.4 Secondary energy minimum of bundles accessed via osmotic stress

To understand the molecular mechanism of the Tau-mediated interactions between microtubules in active bundles, the force response behavior of bundles was measured via SAXS of reaction mixtures under osmotic stress. We used high

molecular-weight PEO-100k (size $\approx$ 40 nm, see Methods) to ensure that polymer depletant did not penetrate the inter-microtubule region in the widely-spaced bundles, creating a polymer concentration exterior to microtubule bundles and thus exerting an osmotic pressure (P) on the bundle itself. By this method (Fig. 4.4a), we measured the microtubule wall-to-wall spacing $D_{w\text{-}w}$ of bundles induced by 3RS and 3RL WT isoforms as a function of increasing P (Fig. 4.4b). The P-$D_{w\text{-}w}$ curves for both WT isoforms exhibit an initial soft repulsion with $D_{w\text{-}w}$ decreasing $\approx$ 3-4 nm up to $P \approx$ 40 Pa followed by a steep increase in slope (with $D_{w\text{-}w}$ decreasing $\approx$ 2-3 nm for 40 Pa $< P < \approx$ 300-400 Pa) consistent with a highly repulsive barrier due to the PD with anionic blocks, resisting osmotic compression. Remarkably, above a critical pressure P_c ($\approx$ 300 and 400 Pa for 3RS and 3RL, respectively) there is an abrupt $\approx$ 5 nm decrease in $D_{w\text{-}w}$ from $\approx$ 21.5 nm to $\approx$ 16.5 nm for 3RS and $\approx$ 27.5 nm to $\approx$ 22.5 nm for 3RL. This sudden jump is reflected in the SAXS data as a sudden large shift in peak position as P is increased to just above P_c (lines in Fig. 4.4a are a guide to the first peak below and above P_c).
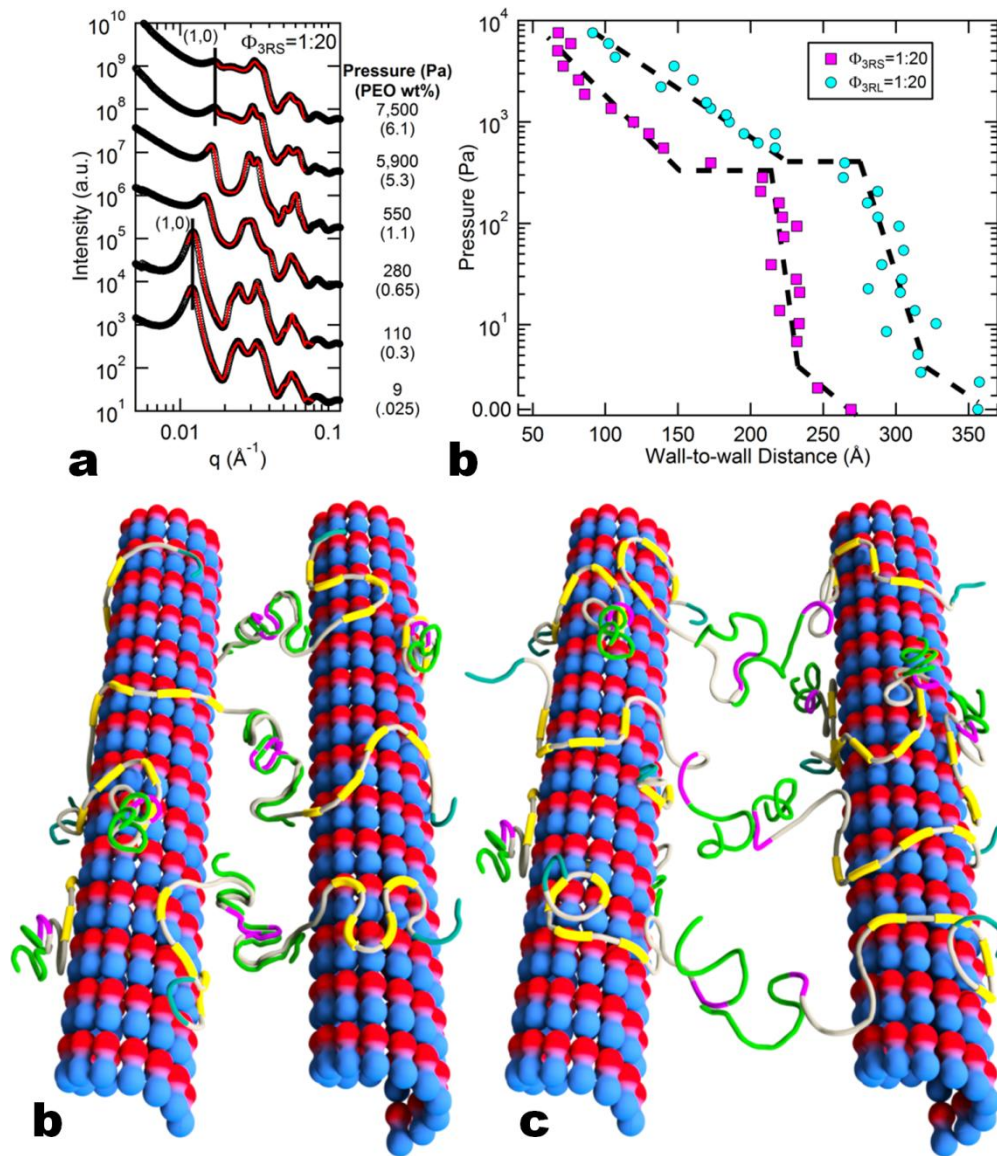
Fig. 4.4 | Direct force measurements of Tau-mediated active microtubule bundles at 37° C in 2 mM GTP reveal distinct energy minima. **a,** Representative azimuthally-averaged SAXS data for $\Phi_{3RS}=1/20$ at selected increasing pressures resulting in increasing peak position of q_{10}, reflecting the decrease in the hexagonal lattice parameter a_H. **b,** The measured wall-to-wall distances (D_{w-w}) for 3RS and 3RL mediated microtubule bundles show a sudden transition (≈ 5 nm decrease) at applied osmotic pressure $P \approx 300\text{-}400$ Pa, indicative of a secondary energy minimum for microtubule bundles. **c,** A cartoon of the osmotic-pressure induced secondary minimum at intermediate D_{w-w}, with anti-parallel dimerization occurring between the anionic section of the NTT (green) and the cationic part of the PD (purple) plus cationic proline-rich region (gray). **d,** A cartoon of the widely-spaced energy minimum, with Tau mediating microtubule bundles by transient charge-charge attractions between the cationic residues (purple/gray) and the anionic residues (green) in the amino-terminal tail.

4.4   Discussion and Conclusions

The osmotic pressure data and, more specifically, the abrupt transition above P_c are consistent with the onset of anti-parallel dimerization between fully-interpenetrating dipolar Tau PDs on opposing microtubule surfaces (Fig. 4.4c). Microtubule bundles at this intermediate spacing are in a second local energy minimum distinct from widely-spaced bundles in the absence of PEO. Several findings support this model. First, reversibility measurements show this local minimum is stable, as bundles for $P > P_c$ do not relax to their previous spacings upon removal of PEO-100k but instead relax to the $D_{w\text{-}w}$ associated with P_c. This implies the barrier between the second and widely-spaced minima is greater than thermal energy $k_B T$. Second, the wall-to-wall spacing observed for this local minimum for intermediate spacing bundles ($D_{w\text{-}w} \approx 22.5$ nm for 3RL) is consistent with recent work showing that PDs for microtubule-bound Tau are in an extended conformation (size ≈ 20 nm for the –L isoforms), twice that of the Tau PD physical diameter in solution[18].

Considering the minimum associated with widely-spaced bundles, several findings with WT Tau isoforms point to the repulsive component emanating from the projection domain containing the anionic block: the steep repulsive barrier when PD chains are pushed together under osmotic pressure and the increase in $D_{w\text{-}w}$ with increasing projection domain length (and increasing anionic block size, Fig. 4.2d). The observation of microtubule phase separation into widely-spaced bundles (Fig. 4.2h), upon addition of small amounts of WT Tau (as low as $\square_{Tau}$ =

1/40), demonstrates a Tau-mediated attractive component of the energy minimum, which overcomes the repulsive component, stabilizing microtubule bundles against dilution. The large D_{w-w} ($\approx$ 38 nm for 3RL), when put in the context of the effective size of PDs ($\approx$ 20 nm for −L isoforms[18]), strongly supports a model where only PD end regions interact with each other to create an attractive potential; although the Tau PD is anionic, locally it is a polyampholyte containing positive and negative residues. Additionally, the short Debye screening length ($\approx$ 9.8 Å) of the reaction mixture solution strongly suggests a mechanism mediated via short-ranged attractions.

Accordingly, we propose that the attraction is provided by transient short-range charge-charge attractions between cationic/anionic residues of weakly penetrating Tau PDs near the midplane-layer between opposing microtubule surfaces (Fig. 4.4d). The proposed short-range attraction would still require transient extensions beyond the average length. Indeed, the SAXS measurements are ensemble-averaged over a finite time, in which transient, extended conformations are possible, as seen in Monte-Carlo simulations of the projection domain of 3RS Tau on microtubule surfaces[25]. While individually these attractions are weak[26], the sum of these interactions over the entire microtubule length should be sufficient to stabilize the inter-microtubule spacing. For 20 µm length[11] hexagonally-packed microtubule bundles, an energy depth of 10-20 $k_B T$ between microtubules would require $\approx$0.05-0.1 $k_B T$ per Tau-

Tau interaction at $\Phi_{Tau} = 1/40$. This mechanism is consistent with shorter, paclitaxel-stabilized microtubules[27] (length ≈ 2 μm) not bundling[14].

A model of polyampholyte-mediated attraction near the midplane-layer dovetails with truncated Tau data: upon deletion of the NTT, the CTT plays an analogous role (which also contains an anionic, but shorter, block, see Fig. 4.1b). However, elimination of the PD anionic block ($3R\Delta(N\text{-})$) results in a large enough attraction between microtubules (which the small CTT anionic block cannot sufficiently counterbalance) such that bundles collapse due to correlated density fluctuations of the highly cationic truncated Tau on the microtubule surface (Fig. 4.3e,g)[28,29]. Similar behavior was observed in tightly-spaced microtubule bundles induced by smaller polyamines like spermine (4+)[23]. Remarkably, this ion correlation mechanism predicts[30] that $D_{w\text{-}w} \approx$ physical size of the macromolecular-counterion ($=2(5/3)^{1/2}R_G$), consistent with $D_{w\text{-}w}/R_G \approx 2\text{-}4$ (Fig. 4.3e,g).

The proposed mode by which Tau bundles microtubules may have major implications for post-translation modifications of Tau associated with neurodegeneration, especially phosphorylation. In tauopathies, both cytosolic Tau and aggregated Tau in neurofibrillary tangles are hyperphosphorylated[31,32]. Our mechanism predicts that increasing Tau phosphorylation would suppress Tau-mediated attractions, disrupt fascicles in the AIS, and impair neuronal polarity crucial to healthy neurons.

A noteworthy conclusion of our study, which goes against normal biological dogma, is that Tau function is tied to its lack of structure. As a charged polymer with both anionic and cationic residues (i.e. a polyampholyte), Tau is able to both specifically bind to microtubules and act as a dynamic chain in bundling microtubules through non-specific electrostatic interactions instead of the more common static cross-linkages mediated through the specific interactions of folded proteins (e.g. α-actinin cross-linking f-actin into parallel bundles[33]). This novel and highly-unusual interaction between widely-spaced surfaces is made possible by the non-uniform charge distribution of the projection domain of Tau, where segments of the NTT (which shift the active zone to the mid-layer) are followed by shorter, attractive domains. This mechanism could also serve as an inspiration for polymer-directed assembling materials.
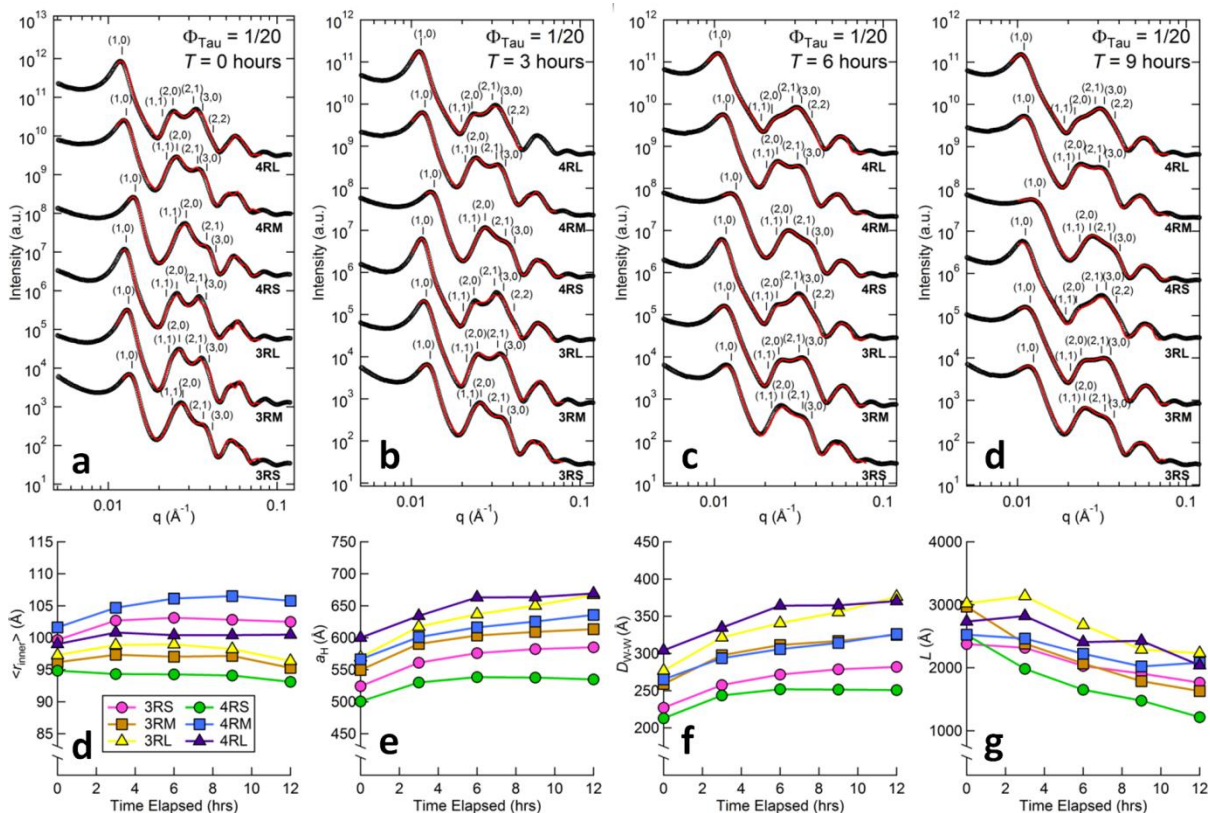
Fig 4.5| Small-angle X-ray scattering (SAXS) and subsequent line-shape analysis of reaction mixtures with tubulin and wild type Tau show hexagonally-ordered microtubule bundles that are stable over 12 hours. Azimuthally-averaged X-ray scattering data of reaction mixtures of tubulin mixed with Tau (from top to bottom: 4RL, 4RM, 4RS, 3RL, 3RM, and 3RS, all at Φ_{Tau} = 1/20) is consistent with long, hollow tubes (microtubules) arranged in a hexagonal arrays, with scattering not significantly changing at T = 0 hours (a), 3 hours (b), 6 hours (c), and 9 hours (d). Extracted parameters via line shape analysis of SAXS data [subsequent fits in red on data in (a-d)] show that although the ensemble-averaged inner radius $<r_{in}>$ (e), hexagonal lattice parameter a_{H} (f), and wall-to-wall distance $D_{w\text{-}w}$ (g) stabilize over time for all wild type Tau-induced bundles, there is a clear monotonic decrease in bundle domain width $L \approx 2(\pi\ln 4)^{1/2}/\kappa_{10}$ (h), where κ_{10} is the first peak width. The decreasing bundle domain width is most likely due to microtubule depolymerization as a result of microtubule dynamic instability.
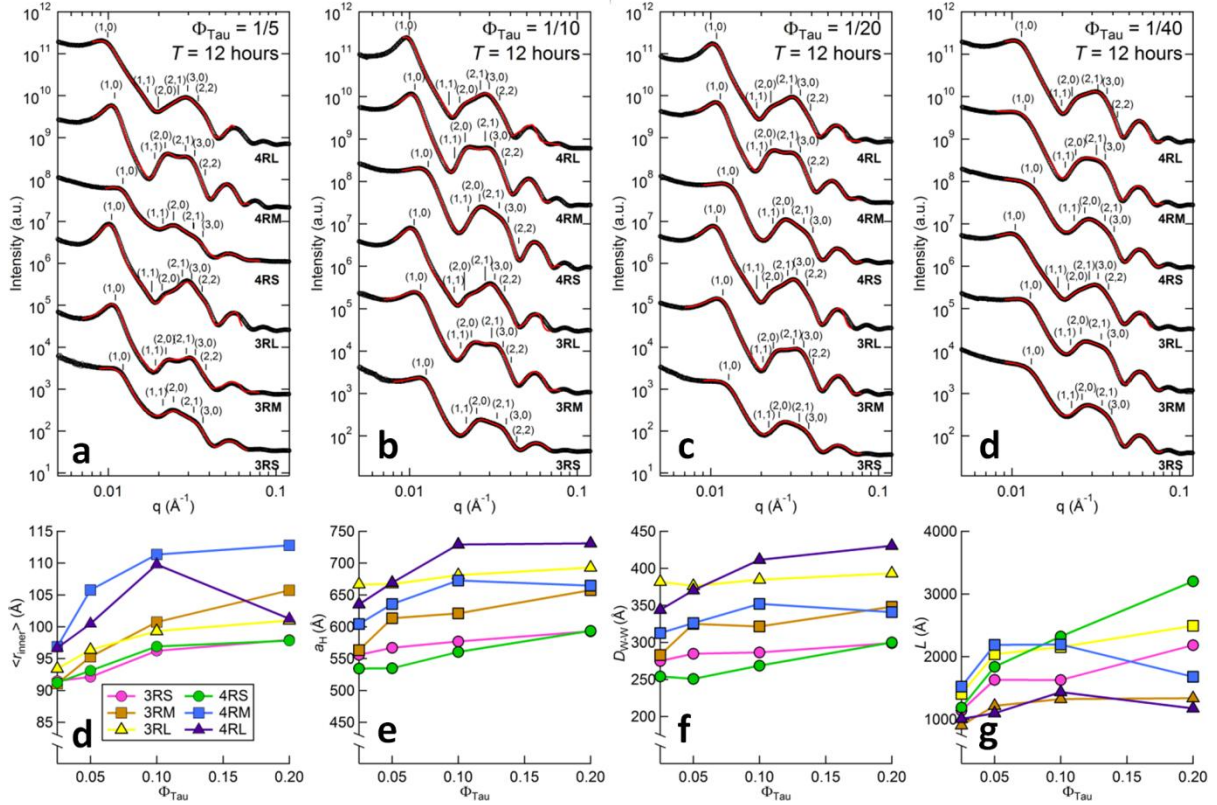
Fig 4.6| Over a physiological range of Φ_{Tau} (1/40 ≥ Φ_{Tau} ≥ 1/5), SAXS and subsequent analysis show the Tau-induced show that microtubule wall-to-wall distance is relatively consistent and is primarily a function of the Tau projection domain length. As before, azimuthally-averaged SAXS data of tubulin mixed with Tau [Φ_{Tau} = 1/5 (**a**), Φ_{Tau} = 1/10 (**b**), Φ_{Tau} = 1/20 (**c**), and Φ_{Tau} = 1/40 (**d**)] at T = 12 hours with subsequent line-shape analysis [fits in red on data in (**a-d**)] revealing the ensemble-averaged inner radius $<r_{in}>$ (**e**), hexagonal lattice parameter a_H (**f**), wall-to-wall distance D_{w-w} (**g**), and bundle domain width L (**h**). Although D_{w-w} changes slight as a function of Φ_{Tau}, D_{w-w} is more directly a function of the Tau projection domain length. Generally, increasing Tau concentration also increases the bundle domain width L, in agreement with suppressed microtubule dynamic instability with increasing Tau.

123
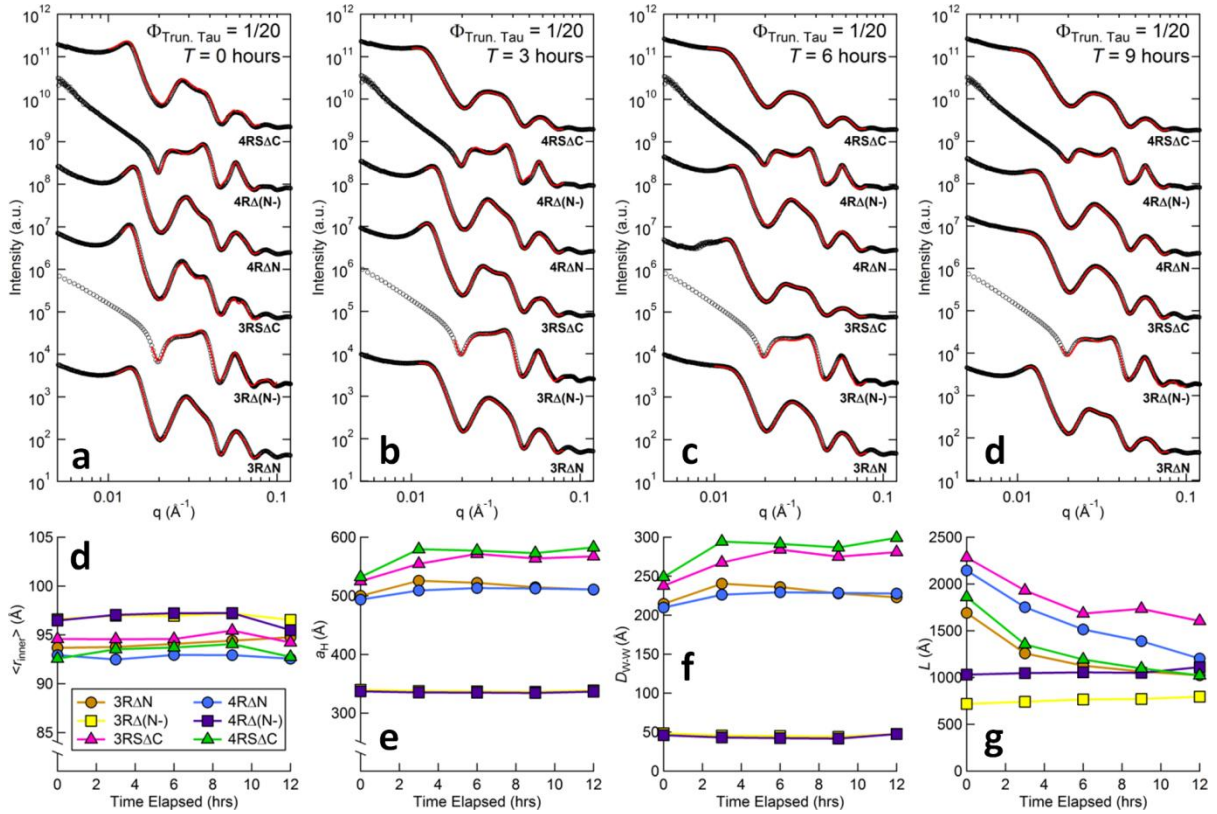
Fig 4.7| Truncated Tau also induces microtubule bundle formation that is remarkably consistent over 12 hours. Azimuthally-averaged SAXS data of tubulin mixed with truncated Tau isoforms [C-terminal tail deletion (4RSΔC, 3RSΔC), anionic domain deletion (4RΔ(N-), 3RΔ(N-)), and N-terminal tail deletion (4RΔN, 3RΔN)] presents scattering consistent with hexagonally-ordered bundles in reaction mixtures ($\Phi_{Trunc. Tau}$ = 1/20) at T = 0 hours (**a**), 3 hours (**b**), 6 hours (**c**), and 9 hours (**d**) with the parameters ensemble-averaged inner radius $<r_{in}>$ (**e**), hexagonal lattice parameter a_H (**f**), wall-to-wall distance D_{w-w} (**g**), and bundle domain width L (**h**) extracted via line-shape analysis. While truncation of the C-terminal tail did not majorly affect D_{w-w} compared to non-truncated variants (see Fig. 4.7**f,g**), truncation of the anionic domain of Tau collapses the microtubules into tightly-packed bundles. Remarkably, truncation of the entire N-terminal tail results in the restoration of relatively widely-spaced microtubules with hexagonal lattice symmetry.

124
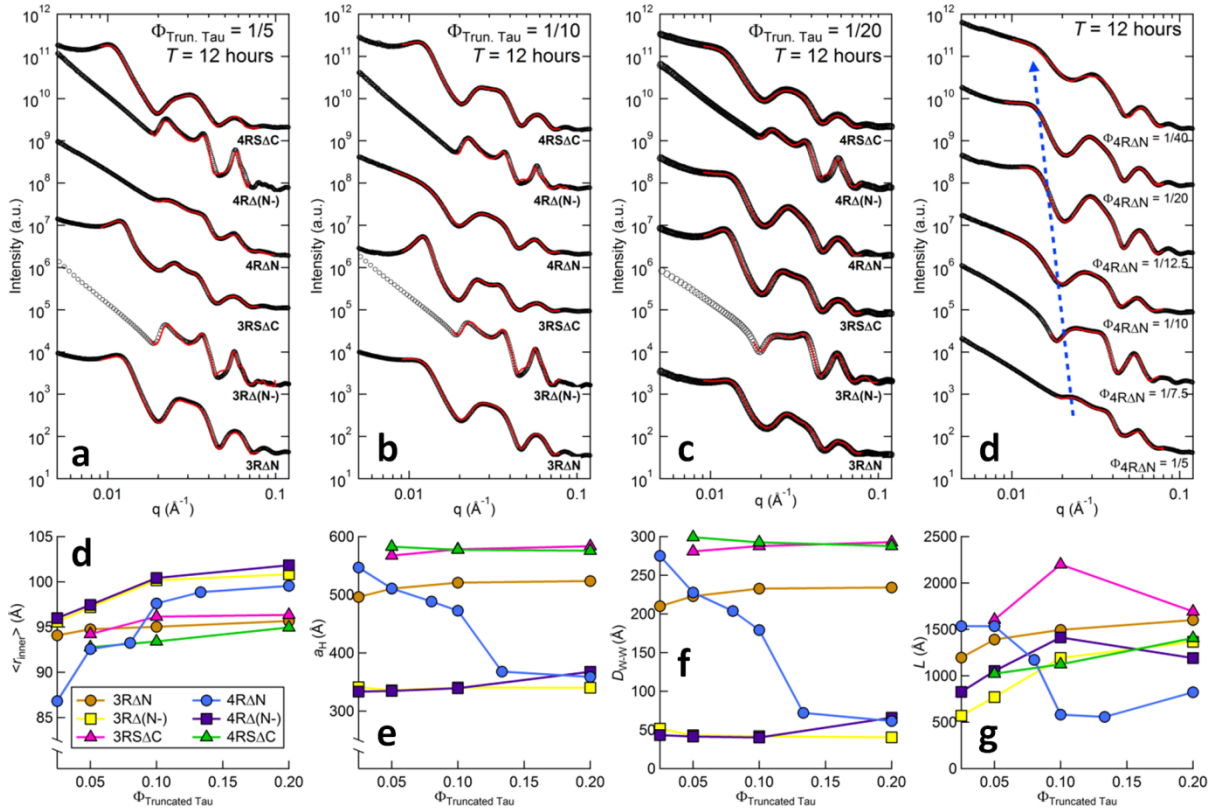
Fig 4.8| Surprisingly, reaction mixtures with 4RΔN Tau (but not 3RΔN) undergo a phase transition from widely-spaced to tightly-packed microtubule bundles with increasing truncated Tau concentration. As before, azimuthally-averaged SAXS data of tubulin mixed with truncated Tau [$\Phi_{\text{Trun. Tau}}$ = 1/5 (a), $\Phi_{\text{Trun. Tau}}$ = 1/10 (b), and $\Phi_{\text{Trun. Tau}}$ (c)] reveal hexagonally-ordered bundles, albeit with varying morphologies. Dramatically changing line profiles for reaction mixtures with 4RΔN prompted higher resolution investigation a function of Tau concentration [$\Phi_{\text{Trun. Tau}}$ = 1/5, 1/7.5, 1/10, 1/12.5, 1/20, and 1/40 (d)] with phase transition observed from widely-spaced to tightly-packed bundles for increasing 4RΔN concentration. Line-shape analysis [subsequent fits in red on data in (a-d)] reveals the ensemble-averaged inner radius $<r_{\text{in}}>$ (e), hexagonal lattice parameter a_{H} (f), wall-to-wall distance $D_{\text{w-w}}$ (g), and bundle domain width L (h), with clear transition observed in (f) and (g).

4.6 References

1. Desai, A. & Mitchison, T. J. Microtubule polymerization dynamics. *Annu. Rev. Cell Dev. Biol.* **13,** 83–117 (1997).

2. Kosik, K. S., Joachim, C. L. & Selkoe, D. J. Microtubule-associated protein tau (tau) is a major antigenic component of paired helical filaments in Alzheimer disease. *Proc. Natl. Acad. Sci. U. S. A.* **83,** 4044–4048 (1986).

3. Hutton, M. *et al.* Association of missense and 5'-splice-site mutations in tau with the inherited dementia FTDP-17. *Nature* **393,** 702–705 (1998).

4. McKee, A. C. *et al.* Chronic traumatic encephalopathy in athletes: progressive tauopathy after repetitive head injury. *J. Neuropathol. Exp. Neurol.* **68,** 709–735 (2009).

5. Peters, A., Palay, S. L. & Webster, H. deF. *The Fine Structure of the Nervous System: Neurons and Their Supporting Cells.* (Oxford University Press, 1991).

6. Chen, J., Kanai, Y., Cowan, N. J. & Hirokawa, N. Projection domains of MAP2 and tau determine spacings between microtubules in dendrites and axons. *Nature* **360,** 674–677 (1992).

7. Palay, S. L., Sotelo, C., Peters, A. & Orkand, P. M. The axon hillock and the initial segment. *J. Cell Biol.* **38,** 193–201 (1968).

8. Rasband, M. N. The axon initial segment and the maintenance of neuronal polarity. *Nat. Rev. Neurosci.* **11,** 552–562 (2010).

9. Baas, P. W., Pienkowski, T. P. & Kosik, K. S. Processes induced by tau expression in Sf9 cells have an axon-like microtubule organization. *J. Cell Biol.* **115,** 1333–1344 (1991).

10. Gustke, N., Trinczek, B., Biernat, J., Mandelkow, E. M. & Mandelkow, E. Domains of tau protein and interactions with microtubules. *Biochemistry* **33,** 9511–9522 (1994).

11. Brandt, R. & Lee, G. Orientation, assembly, and stability of microtubule bundles induced by a fragment of tau protein. *Cell Motil. Cytoskeleton* **28,** 143–154 (1994).

12. Derry, W. B., Wilson, L. & Jordan, M. A. Substoichiometric binding of taxol suppresses microtubule dynamics. *Biochemistry* **34,** 2203–2211 (1995).

13. Ojeda-Lopez, M. A. *et al.* Transformation of taxol-stabilized microtubules into inverted tubulin tubules triggered by a tubulin conformation switch.

Nat. Mater. **13,** 195–203 (2014).

14. Choi, M. C. *et al.* Human microtubule-associated-protein tau regulates the number of protofilaments in microtubules: A synchrotron X-ray scattering study. *Biophys. J.* **97,** 519–527 (2009).

15. Black, M. M., Slaughter, T., Moshiach, S., Obrocka, M. & Fischer, I. Tau is enriched on dynamic microtubules in the distal region of growing axons. *J. Neurosci.* **16,** 3601–3619 (1996).

16. Nagahama, K., Inomata, H. & Saito, S. Measurement of osmotic pressure in aqueous solutions of poly(ethylene glycol) and poly(N-isopropylacrylamide). *Fluid Phase Equilib.* **96,** 203–214 (1994).

17. Devanand, K. & Selser, J. C. Asymptotic Behavior and Long-Range Interactions in Aqueous Solutions of Poly (ethylene oxide). *Macromolecules* **24,** 5943–5947 (1991).

18. Chung, P. J. *et al.* Direct force measurements reveal protein Tau confers short-range attractions and isoform-dependent steric stabilization to microtubules. *Proc. Natl. Acad. Sci.* **112,** E6416–E6425 (2015).

19. Andreu, J. M. *et al.* Low resolution structure of microtubules in solution. *J. Mol. Biol.* **226,** 169–184 (1992).

20. Brandt, R. & Lee, G. Functional organization of microtubule-associated protein tau. Identification of regions which affect microtubule growth, nucleation, and bundle formation in vitro. *J. Biol. Chem.* **268,** 3414–3419 (1993).

21. Mylonas, E. *et al.* Domain conformation of tau protein studied by solution small-angle X-ray scattering. *Biochemistry* **47,** 10345–10353 (2008).

22. Kohn, J. E. *et al.* Random-coil behavior and the dimensions of chemically unfolded proteins. *Proc. Natl. Acad. Sci. U. S. A.* **101,** 12491–12496 (2004).

23. Needleman, D. J. *et al.* Higher-order assembly of microtubules by counterions: from hexagonal bundles to living necklaces. *Proc. Natl. Acad. Sci. U. S. A.* **101,** 16099–16103 (2004).

24. Trinczek, B., Biernat, J., Baumann, K., Mandelkow, E. M. & Mandelkow, E. Domains of tau protein, differential phosphorylation, and dynamic instability of microtubules. *Mol. Biol. Cell* **6,** 1887–1902 (1995).

25. Leermakers, F. A. M., Jho, Y.-S. & Zhulina, E. B. Modeling of the 3RS tau protein with self-consistent field method and Monte Carlo simulation. *Soft Matter* **6,** 5533 (2010).

26.   Makrides, V. *et al.* Microtubule-dependent oligomerization of tau. Implications for physiological tau function and tauopathies. *J. Biol. Chem.* **278,** 33298–304 (2003).

27.   Carlier, M. F. & Pantaloni, D. Taxol effect on tubulin polymerization and associated guanosine 5'-triphosphate hydrolysis. *Biochemistry* **22,** 4814–4822 (1983).

28.   Oosawa, F. Interaction between parallel rodlike macroions. *Biopolymers* **6,** 1633–1647 (1968).

29.   Netz, R. R. Electrostatistics of counter-ions at and between planar charged walls: From Poisson-Boltzmann to the strong-coupling theory. *Eur. Phys. J. E - Soft Matter* **5,** 557–574 (2001).

30.   *Small-Angle X-Ray Scattering.* (Academic Press, 1982).

31.   Grundke-Iqbal, I. *et al.* Abnormal phosphorylation of the microtubule-associated protein tau (tau) in Alzheimer cytoskeletal pathology. *Proc. Natl. Acad. Sci. U. S. A.* **83,** 4913–4917 (1986).

32.   Alonso, A. C., Zaidi, T., Grundke-Iqbal, I. & Iqbal, K. Role of abnormally phosphorylated tau in the breakdown of microtubules in Alzheimer disease. *Proc. Natl. Acad. Sci. U. S. A.* **91,** 5562–5566 (1994).

33.   Biology, C. *Cell Biology.* (Saunders/Elsevier, 2008).

5. Conclusions

While much of the initial research pertaining to Alzheimer's dealt with the protein amyloid beta[1–5] (due, in part, to amyloid beta being the main constituent of extracellular plaques, a characteristic feature of Alzheimer's), the discovery that many of the neurodegenerative symptoms associated with Alzheimer's could be found in victims of chronic traumatic encephalopathy[6] *without* amyloid beta plaques but *with* neurofibrillary tangles (made up primarily of hyperphosphorylated Tau) has, to a certain extent, caused a re-examination of the physiological and pathophsyiological roles Tau may play in brain function and neurodegeneration, respectively. Indeed, it was recently discovered that Tau pathology may actually spread trans-synaptically[7], much like prions in bovine spongiform encephalopathy[8]. These new moieties through which Tau can exhibit dysfunction have underscored the need to characterize the biophysical and biochemical properties of Tau.

This work represents an attempt to assess the action of Tau on the microtubule surface, such that we may not only understand the putative interactions between Tau and microtubules, but correlate phenomenon observed in our cell-free studies to *in vivo* and *in vitro* experiments. Additionally, as an intrinsically disordered protein (IDP) it is quite possible that motifs that occur in Tau may recur in other IDPs. This is particularly imperative, as other IDPs, such as α-synuclein, are implicated in neurodegenerative diseases as well.

5.1. Implications for Physiological Function

It has been well established that increasingly phosphorylation of Tau, especially to the carboxyl-terminal half, reduces the binding affinity for microtubules[9,10], but much less is understood of the role of phosphorylation of the amino-terminal half, particularly the Tau projection domain. In observing a mushroom-to-brush transition of Tau, it is clear that increasing phosphorylation of the Tau projection domain would likely alter the Tau coverage at which the transition occurs (owing to an expanded mushroom state as a result of increased intra-Tau repulsion) and increase the steric repulsion of microtubules against other microtubules or macromolecules that exist within the axoplasm. While I have shown that Tau is able to mediate attractions over longer microtubules with higher-order architectures mimicking axonal initial segment microtubules fascicles, it should be noted that axonal microtubules exhibit the nematic phase over most of the axon[11,12]. As Tau phosphorylation increases, it is quite possible that the non-specific, sub-$k_{\mathrm{B}}T$ attractions mediated by Tau are suppressed or overwhelmed by the increasingly anionic characteristic of the projection domain, resulting in sterically-stabilized microtubules in the nematic phase. Indeed, this is consistent with the spatial map of Tau phosphorylation in axons, with phosphorylation increasing as Tau is further removed from the axon initial segment[13,14].

If higher-order microtubule architectures are not observed over the majority of the axon, what, then, would be the function of Tau-mediated microtubule

fascicles in the axonal initial segment (AIS)? The answer may lie in the AIS steering axon-specific cargo, contributing to neuronal polarity (i.e. ensuring distinct cellular environments for axons and dendrites)[15]. While this steering mechanism remains unknown[16], it has been thought the differences in microtubule polarity (mixed in dendrites, polarized towards the distal end in axons) may be a factor. The molecular motors kinesin and dynein travel towards the positive and negative end of microtubules, respectively. Additionally, cargo is thought to be moved by multiple motors[17,18]. Fascicles of microtubules may increase the polarized-microtubule area for an axonal-specific combination of motors to travel on. However, I would like to propose another alternative, in light of the discovery of sub-$k_B T$ attractions between microtubules in Tau-mediated bundles. While previous efforts have focused on groups of motors traveling on a single microtubule, it may be entirely possible Tau-mediated microtubule fascicles provide a platform for transport to occur via multiple microtubules "docking" sites with locally weak Tau-Tau interactions producing only a small impediment towards axonal transport.

5.2. Implications for Pathophysiological Function

Tau is known to be constitutively phosphorylated in mature neurons with Tau binding-affinity to MTs thought to be regulated by phosphorylation[19]. However, in tauopathies, both cytosolic Tau and aggregated Tau in neurofibrillary tangles are often found to be hyperphosphorylated[20,21].

Additionally, lysine acetylation of Tau is suggested to be another potential pathological pathway in Alzheimer's and other neurodegenerative disorders[22]. While it is clear that the binding affinity of the mostly-cationic Tau to the anionic-microtubules would decrease upon increasing Tau phosphorylation (through increasing anionic charge) and acetylation (through decreasing cationic charge), a mechanism of sub-$k_B T$ interactions predicts that the bundling activity should also decrease upon increasing phosphorylation and acetylation, particularly at the many post-translation sites in the projection domain[23]. Indeed, there is direct cell-culture evidence that increasing Tau phosphorylation by GSK-3β leads to a decrease in higher-order MT bundles[24] and cell-free reconstitution of acetylated-Tau mimetic mutants with MTs dramatically decreases bundling activity relative to WT Tau isoforms[22]. While the loss of function paradigm for Tau has often focused on the inability for hyperphosphorylated Tau to bind to microtubules (thus increasing microtubule depolymerization and subsequently decreasing axonal transport), the loss of fasciculated microtubules may also be a feature of Tau-induced pathogenesis.

Furthermore, the loss of function paradigm for Tau may be more nuanced than increasing microtubule depolymerization in the absence of stabilizing Tau. The ability for Tau to sterically stabilize microtubules is contingent on the coverage of Tau on the microtubule surface. Even slight changes to the binding affinity of Tau to the microtubule surface could cause a drop in coverage below

which a conformational transition in which microtubules are not sterically stabilized occurs.

5.3.   Implications for other Intrinsically Disordered Proteins

Although Tau and its subdomains are intrinsically disordered[25], this work has shown that although Tau bound to microtubules may assume a structure[26], said structures and concomitant interactions induced may require examining the aggregate properties of Tau on the microtubule surface. We see that Tau undergoes a mushroom-to-brush transition as a function of Tau coverage and that Tau mediates microtubule bundling through an aggregate of sub-$k_{\mathrm{B}}T$ interactions, both of which would have been impossible to observe if Tau was under dilute conditions.

Furthermore, the observation of Tau-mediated microtubule bundling under paclitaxel-free conditions underscores the importance of attempting to mimic cellular conditions when attempting cell free experiments. Indeed, microtubule dynamic instability would have made many experiments intractable were it not for the discovery that paclitaxel (known popularly as its chemotherapeutic formulation Taxol) promoted and stabilized microtubules against cold- and calcium ion-induced microtubule depolymerization[27]. Although the use of paclitaxel did alter microtubule structure by decreasing the microtubule radius[28], minor changes to the microtubule structure were outweighed by the robustness of microtubules for experiments, especially at room temperature.

This, unfortunately, may have lead to results that were specific to paclitaxel-stabilized microtubules only (e.g. the conclusion that Tau was purely repulsive[29]) as opposed reflecting a true biological reality.

5.4.   Future Directions

One of the more critical post-translational modifications of Tau, phosphorylation, has escaped a systematic characterization due to the difficulty in producing Tau isoforms with site-specific phosphorylations. While *in vivo* and *in vitro* experiments have been able to identify the general effects of phosphorylation (and, to a certain extent, hyperphosphorylation) on cell function[30,31], understanding the specific role of Tau being phosphorylated at a specific site would require greater control of phosphorylation and the conditions under which it occurs. As some sites have been reported to be more correlated to the abnormal hyperphosphorylation of Tau in Alzheimer's disease[31] than others, it would be interesting if said phosphorylation gave way to any structural changes to Tau structure and/or function.

Finally, the role of the axon initial segment (AIS), while seen as critical in the development of neuronal polarity, is not entirely clear. If one were able to recreate the conditions in which the AIS exists (with the appropriate confined geometries) in cell free reconstitutions, one might be able to identify the properties that make the axon initial segment so unique in acting both as

cytoskeletal-based diffusion barrier[32] while accepting axonal and rejecting dendritic cargo. As fascicles of microtubules are a cardinal feature of the AIS, it would be easy to imagine that the higher-order molecular architecture may affect properties specific to the AIS.

5.5. References

1. Tanzi, R. E. *et al.* Amyloid beta protein gene: cDNA, mRNA distribution, and genetic linkage near the Alzheimer locus. *Science* **235,** 880–884 (1987).

2. Haass, C. *et al.* Amyloid Beta-Peptide Is Produced by Cultured-Cells during Normal Metabolism. *Nature* **359,** 322–325 (1992).

3. Huang, Y. & Mucke, L. Alzheimer mechanisms and therapeutic strategies. *Cell* **148,** 1204–1222 (2012).

4. Soto, C. *et al.* Beta-sheet breaker peptides inhibit fibrillogenesis in a rat brain model of amyloidosis: implications for Alzheimer's therapy. *Nat. Med.* **4,** 822–826 (1998).

5. Iwai, a *et al.* The precursor protein of non-A beta component of Alzheimer's disease amyloid is a presynaptic protein of the central nervous system. *Neuron* **14,** 467–475 (1995).

6. McKee, A. C. *et al.* Chronic traumatic encephalopathy in athletes: progressive tauopathy after repetitive head injury. *J. Neuropathol. Exp. Neurol.* **68,** 709–735 (2009).

7. Liu, L. *et al.* Trans-synaptic spread of tau pathology in vivo. *PLoS One* **7,** (2012).

8. Hyman, B. T. Tau propagation, different tau phenotypes, and prion-like properties of tau. *Neuron* **82,** 1189–1190 (2014).

9. Bramblett, G. T. *et al.* Abnormal tau phosphorylation at Ser396 in alzheimer's disease recapitulates development and contributes to reduced microtubule binding. *Neuron* **10,** 1089–1099 (1993).

10. Biernat, J., Gustke, N., Drewes, G., Mandelkow, E. & Mandelkow, E. Phosphorylation of Ser262 strongly reduces binding of tau to microtubules: Distinction between PHF-like immunoreactivity and microtubule binding. *Neuron* **11,** 153–163 (1993).

11. Peters, A., Palay, S. L. & Webster, H. deF. *The Fine Structure of the Nervous System: Neurons and Their Supporting Cells.* (Oxford University Press, 1991).

12. Palay, S. L., Sotelo, C., Peters, A. & Orkand, P. M. The axon hillock and the initial segment. *J. Cell Biol.* **38,** 193–201 (1968).

13. Black, M. M., Slaughter, T., Moshiach, S., Obrocka, M. & Fischer, I. Tau is enriched on dynamic microtubules in the distal region of growing axons. *J.*

Neurosci. **16,** 3601–3619 (1996).

14. Mandell, J. W. & Banker, G. a. A spatial gradient of tau protein phosphorylation in nascent axons. *J. Neurosci.* **16,** 5727–5740 (1996).

15. Rasband, M. N. The axon initial segment and the maintenance of neuronal polarity. *Nat. Rev. Neurosci.* **11,** 552–562 (2010).

16. Maday, S., Twelvetrees, A. E., Moughamian, A. J. & Holzbaur, E. L. F. Axonal Transport: Cargo-Specific Mechanisms of Motility and Regulation. *Neuron* **84,** 292–309 (2014).

17. Hendricks, A. G., Holzbaur, E. L. F. & Goldman, Y. E. Force measurements on cargoes in living cells reveal collective dynamics of microtubule motors. *Proc. Natl. Acad. Sci. U. S. A.* **109,** 18447–52 (2012).

18. Welte, M. A., Gross, S. P., Postner, M., Block, S. M. & Wieschaus, E. F. Developmental regulation of vesicle transport in Drosophila embryos: Forces and kinetics. *Cell* **92,** 547–557 (1998).

19. Lindwall, G. & Cole, R. D. Phosphorylation affects the ability of tau protein to promote microtubule assembly. *J. Biol. Chem.* **259,** 5301–5305 (1984).

20. Grundke-Iqbal, I. *et al.* Abnormal phosphorylation of the microtubule-associated protein tau (tau) in Alzheimer cytoskeletal pathology. *Proc. Natl. Acad. Sci. U. S. A.* **83,** 4913–4917 (1986).

21. Alonso, A. C., Zaidi, T., Grundke-Iqbal, I. & Iqbal, K. Role of abnormally phosphorylated tau in the breakdown of microtubules in Alzheimer disease. *Proc. Natl. Acad. Sci. U. S. A.* **91,** 5562–5566 (1994).

22. Cohen, T. J. *et al.* The acetylation of tau inhibits its function and promotes pathological tau aggregation. *Nat. Commun.* **2,** 252 (2011).

23. Lee, G. *et al.* Phosphorylation of tau by fyn: implications for Alzheimer's disease. *J. Neurosci.* **24,** 2304–2312 (2004).

24. Wagner, U., Utton, M., Gallo, J. M. & Miller, C. C. Cellular phosphorylation of tau by GSK-3 beta influences tau binding to microtubules and microtubule organisation. *J. Cell Sci.* **109 (Pt 6,** 1537–1543 (1996).

25. Mylonas, E. *et al.* Domain conformation of tau protein studied by solution small-angle X-ray scattering. *Biochemistry* **47,** 10345–10353 (2008).

26. Kadavath, H. *et al.* Folding of the Tau Protein on Microtubules. *Angew. Chemie Int. Ed.* n/a–n/a (2015). doi:10.1002/anie.201501714

27. Schiff, P. B., Fant, J. & Horwitz, S. B. Promotion of microtubule assembly

in vitro by taxol. *Nature* **277,** 665–667 (1979).

28. Andreu, J. M. *et al.* Low resolution structure of microtubules in solution. *J. Mol. Biol.* **226,** 169–184 (1992).

29. Trinczek, B., Biernat, J., Baumann, K., Mandelkow, E. M. & Mandelkow, E. Domains of tau protein, differential phosphorylation, and dynamic instability of microtubules. *Mol. Biol. Cell* **6,** 1887–1902 (1995).

30. Stoothoff, W. H. & Johnson, G. V. W. Tau phosphorylation: Physiological and pathological consequences. *Biochim. Biophys. Acta - Mol. Basis Dis.* **1739,** 280–297 (2005).

31. Yu, Y. *et al.* Developmental regulation of tau phosphorylation, tau kinases, and tau phosphatases. *J. Neurochem.* **108,** 1480–1494 (2009).

32. Li, X. *et al.* Novel diffusion barrier for axonal retention of Tau in neurons and its failure in neurodegeneration. *EMBO J.* **30,** 4825–4837 (2011).

Appendix

Tau Purification Protocol

Purpose: To grow, harvest, and purify MAP Tau and other constructs from glycerol cell stocks.

Day One: Media

1. Using large graduated cylinder (red bottom), make 6.0 L of AIM

    a. Fill graduated cylinder with approximately 5.5 L of nanopure water

    b. Add sterile stir bar, begin mixing before adding ingredients

    c. Add ingredients:

        i. 60g of Peptone (Tryptone)

        ii. 30g of Yeast Extract

        iii. 21.36g of Na_2HPO_4 (CAS#: 7558-79-4)

        iv. 20.g of KH_2PO_4 (CAS#: 7778-77-0)

        v. 16.08g of NH_4Cl (CAS#: 12125-02-9)

        vi. 4.32g of Na_2SO_4 (CAS#: 7757-82-6)

        vii. 2.94g of $MgSO_4$ (CAS#: 10034-99-8)

        viii. 30mL of Glycerol (Wash out glycerol from graduate cylinder using DI water, getting AIM to 6.0 L) (CAS#: 56-81-5)

        ix. 3g of Dextrose (CAS#: 50-99-7)

        x. 12g of Lactose (CAS#: 5989-81-1)

d. Spin to homogeneity (Should be yellow-brown, no floating particulates)

2. Using 500mL beaker or 250mL flask, make 250 mL of LB

   a. Fill container with approximately 200 mL of DI water

   b. Add sterile stir bar, begin mixing before adding ingredients

   c. Add ingredients

      1. 2.50g of Peptone (Tryptone)

      2. 1.25g of Yeast Extract

      3. 2.50g of NaCl (CAS#: 7647-14-5)

   d. Spin to homogeneity (Should be yellow, no floating particulates)

3. Divide AIM into 6 2.0L flasks (1L in each)

4. Pour LB into 1 500mL flasks

5. Autoclave AIM and LB, 35 minute wet cycle, 0 minutes dry

6. When cool, add 1% (V/V) of ampicillin solution (see Note 1) to LB, which should be approximately 2.5 mL.

7. Add bugs to LB

8. Shake overnight at 37deg C, 250RPM. Keep in mind that this cycle should last approximately 18 hours

Note 1: Ampicillin (CAS#: 7177-48-2) should be set to 5 mg/mL in DI Water. A pellet of NaOH may be added to make it easier for Ampicillin to dissolve.

Solution should be stored in cold environment. Ampicillin salt does not require addition pellet of NaOH.

Day Two: Induction

1. Add 1% (V/V) of ampicillin solution to each 2.0L flask with 1L of LB, which should be 10 mL.

2. Divides contents of LB flask into the six AIM flask

3. Shake for 24 hours at 37 deg C, 250 RPM

4. Wash empty LB flasks with dilute solution bleach in water

Day Three: Harvesting and Lysing

1. The French Press apparatus should be placed in the refrigerator in order to minimize time bacteria spends near or at room temperatures.

2. Form pellets of bacteria

    a. Add contents of 2 2.0L AIM flasks into 6 800mL centrifuge bottles

    b. Balance centrifuge bottles with DI water

    c. Centrifuge bottles at 5000 RPM for 10 minutes

    d. Discard supernatant into empty AIM flasks

    e. Repeat steps A-D with remaining sets of AIM flasks. Take particular note that pellets should be facing same direction when in centrifuge rotor as previous centrifugations.

3. Using 10mL pipette tip, carefully move pellets from 5 centrifuge bottles into one bottle.

4. Using 40mL of BRB80+.1%BME (See Note 2), sequentially wash out five remaining centrifuge bottles, with extra concern in resuspending remaining pellet (scrape with 10mL pipette tip, shake vigorously)

5. Add BRB80+.1%BME+remaining pellet into centrifuge bottle with pellets

6. Resuspend pellet in last bottle by scraping with 10mL pipette tip and shaking vigorously. Pour solution into 3-4 50mL falcon tubes

7. Clean out remaining 6 centrifuge bottles ~30 mL of 50% BRB80+.1% BME solution/Isopropanol solution

8. Add equal amounts of 50% BRB80+.1% BME solution/Isopropanol solution in 50mL falcon tubes, vortexing resulting solution. There should be approximately 40 mL in each falcon tube.

9. Flash freeze 50mL falcon tubes in isopropanol/dry ice slurry for a period of at least 15 minutes (This is a period of time where it might be good to take a break, or eat lunch, provided there is enough dry ice)

10. Thaw pellet in running water

11. Run resuspended pellet through French Press

12. Set up French Press apparatus. Plunger should inserted to the appropriate level, appropriate tubing hooked up, and cap securely fastened by bolt.

13. Insert apparatus into machine and activate.

14. Ensure that the pressure within the apparatus does not fall below 1000 PSI and exceed 1200 PSI to maximize cell shearing.

15. Repeat twice for each 50 mL falcon tube of resuspended pellet.

16. Wash apparatus and return to Foltz laboratory.

17. In a 500mL beaker, boil ~200mL of water (NOT DI water). Once boiling, boil falcon tubes until solution in falcon tubes begins to foam (~5 min)

18. Pour suspended pellets into four centrifuge tubes. Wash out falcon tubes w/ BRB80+.1%BME, using wash to balance centrifuge tubes

19. Spin suspension at 10K RPM, 4deg C for 10 minutes.

20. Freeze supernatant in -80deg Freezer. Trash pellet in sink.

Note 2: BRB80 is 80mM PIPES (CAS#: 1000037-69-2), 1 mM EGTA (CAS#: 67-42-5), and 1 mM MgCl2 (CAS#: 7791-18-6). .1% (V/V) of BME (CAS#: 60-24-2) should be added after solution has been maded.

Day Four: Phosphocellulose Column

1. Prepared column bed buffers: 1.0L of .5M NaOH, 2.0L of NaPO4 buffer, and 1.0L of .5 M HCl (under fume hood) (see Note 3).

2. While cycling pH through columns, melt lysate (supernatant) from Day 3 in running cold water and clean column/tubing necessary for phosphocellulose chromotography

3. Cycle pH through column:

a. Weigh ~1g phosphocellulose per liter of AIM used (6g for 6.0L of AIM)

b. Pour ~250mL of NaOH solution on phosphocellulose, mix thoroughly

c. Allow phosphocellulose to settle until clear boundary forms (~5 minutes)

d. Pour off fines into sink

e. Repeat steps b-d but with phosphate buffer, HCl solution, and finally phosphate buffer

f. Buffer exchange using steps b-d with BRB80+.1%BME twice. Pour as much off as possible without losing phosphocellulose

4. Mix lysate with phosphocellulose

5. In 50 mL falcon tubes, rotate phosphocellulose+lysate mixtures in cold room for ~60 minutes.

6. Pour into clean column, allowing for phosphocellulose to settle within column. If everything cannot fit into column, wait until phospocellulose has settled, pipette solution into reservoir, and pour remaining phosophocellulose+lysate into column

7. Connect column to peristaltic pump (downstream) and column to reservoir cup (upstream)

8. Run column

a. Gradually increasing collect speed from 0 to 3 mL/min, run flow-through phosphocellulose column and collect.

b. Wash with 2 column volumes (for ~6g of phosphocellulose, 50 mL) of BRB80+.1% BME.

c. Collect fractions 1-8 of 2 column volumes of 50 mM $(NH_4)_2SO_4$. 150 mM $(NH_4)_2SO_4$, 250 mM $(NH_4)_2SO_4$, and 1 M $(NH_4)_2SO_4$, all in BRB80+.1% BME.

9. Run column results of flow through, wash, and fractions acquired from phosphocellulose columns with SDS-PAGE (See SDS-PAGE Protocol)

Note 3: Sodium phosphate buffer is 87.2 g of sodium phosphate dibasic (CAS#: 7558-79-4) and 47.8 g of sodium phosphate monobasic (CAS#: 10049-21-5).

Day Five: Hydrophobic Interaction Chromotography (HIC) Column

1. Having identified the fractions in which pure target protein appears, collect the appropriate fractions and add $(NH_4)_2SO_4$ to get the salt concentration to 1M.

2. Once HIC Column has been completely washed with Buffer A, load sample:

a. Place 50mL falcon tube at the end of waste line to collect

b. Bring column off-line by disconnecting feed tubing from intermix chamber

  c. Connect feed line to clean column

  d. Anchor syringe to scaffolding

  e. Add all fractions + proteins to syringe

  f. Run at 1.00 mL/min

3. Reconnect tubing to mixing chamber, and flow 10 column volumes of buffer A to wash through at 1 mL/min (it is possible that air has been trapped in the line between syringe/mixing chamber and the column; in that case, it is best to unhook the line before the column and allow air to escape until only buffer is coming through, then reconnecting)

4. Run HIC Column program:

  a. Fill rack with culture tubes in appropriate fraction collector

  b. Run HIC program

    1. 0-60% Buffer B for 100 min

    2. 60-100% Buffer B for 10 min

    3. Collect in 1.5 mL fractions

  c. Clean column with cleaning program

5. Take 10uL aliquots from approximately every 3rd fraction and run using SDS-PAGE gels to identify fractions containing the target protein

Day Six: Concentration and Characterization

1. Identify from SDS-PAGE results and concentrate relevant fractions with Amicon Centrifugal units and run Tau characterization.

SDS-PAGE Protocol

Purpose: SDS-Page can be used to identify and quantify proteins of interest.

SDS-PAGE Gel:

Necessary Materials: 4x Resolving Buffer, 4x Stacking Buffer, 1x Electrode Buffer, 40% Bis/Acrylamide, DI Water, 10% APS, TEMED (CAS#: 110-18-9), Isopropanol, 2x Sample Buffer

4x Resolving Buffer: 1.5M Tris (Acid or Base), pH 8.8, .4% (%W/V) of sodium dodecyl sulfate (CAS #151-21-3) OR sodium lauryl sulfate

4x Stacking Buffer: .5M Tris (Acid or Base), pH 6.8, .4% (%W/V) of sodium dodecyl sulfate (CAS #151-21-3) OR sodium lauryl sulfate

10x Running Buffer (1 L): 144g of Glycine (CAS#: 56-40-6), 30g of Tris Acid (CAS#: 1185-53-1), 10g of sodium dodecyl sulfate (SDS), filling up to 1L with DI water. For 1x running buffer, dilute 10x running with 9:1 ratio of DI Water:10x running buffer

10% APS: 1g of ammonium persulfate (CAS#: 7727-54-0), filling up to 1mL with DI water

2x Sample Buffer (40 mL):10 mL of 4x stacking buffer, 10 mL of glycerol, .8 g of sodium dodecyl sulfate (SDS), .1g of bromophenol blue (CAS#: 115-39-9), fill up to 40 mL with DI water

Table 1: Formula Chart for 1 Resolving Gel

	7%	8%	10%	12%	14%
40% Bis/Acrylamide	.875 mL	1.0 mL	1.25 mL	1.5 mL	1.75 mL
4x Resolving Buffer	1.25 mL	1.25 mL	1.25 mL	1.25 mL	1.25 mL
DI Water	2.875 mL	2.75 mL	2.5 mL	2.25 mL	2.0 mL
10% APS	40 uL	40 uL	40 uL	40 uL	40 uL
Temed	8 uL	8 uL	8 uL	8 uL	8 uL

Table 2: Formula Chart for 2 Resolving Gels

	7%	8%	10%	12%	14%
40% Bis/Acrylamide	1.75 mL	2.0 mL	2.5 mL	3.0 mL	3.5 mL
4x Resolving Buffer	2.5 mL	2.5 mL	2.5 mL	2.5 mL	2.5 mL
DI Water	2.875 mL	5.5 mL	5 mL	4.5 mL	4.0 mL
10% APS	80 uL	80 uL	80 uL	80 uL	80 uL
Temed	16 uL	16 uL	16 uL	16 uL	16 uL

Table 3: Formula Chart for 2 Stacking Gels

40% Bis/Acrylamide	.625 mL
4x Stacking Buffer	1.25 mL
DI Water	3.125 mL
10% APS	40 uL
Temed	10 uL

1. Take appropriate number of gel plates and place in gel plate holder. Once secure in gel plate holder, put gel plate holder + gel plates in gel holder dock. Fill with water to ensure bottom of the gel plates are appropriately sealed.

2. Make resolving gel solutions without adding APS or TEMED.

3. Once the gel plates have been sealed from the bottom, evacuate water and wick with kimwipes to dry out gap between gel plates.

4. Add APS and TEMED to resolving gel solution, adding 4.4 mL of the complete solution to each gap between gel plates. Quickly pipette isopropanol on top of polymerizing resolving gel solution to get rid of bubbles and define clear boundary.

5. Prepare stacking gel solution while resolving gel is polymerizing. Again, do not add APS or TEMED until resolving gel has been completely polymerized.

6. Once resolving gel has been polymerized, wash out with DI water and wick with kimwipes/paper towels to dry out remaining gap between gel plates.

7. Add APS and TEMED to stacking gel solution, adding to the very top of the gel plates. Quickly insert gel comb to create loading wells for samples.

8. Store in 1x running buffer for future use (within 1 week of creation)